Title
Synthesis and Utilization of Titanium (IV) Dioxide Nanomaterials and its Derivatives

Permalink
https://escholarship.org/uc/item/0wp8q05p

Author
Dahl, Michael James

Publication Date
2015

Peer reviewed|Thesis/dissertation

UNIVERSITY OF CALIFORNIA
RIVERSIDE

Synthesis and Utilization of Titanium (IV) Dioxide Nanomaterials and its Derivatives

A Dissertation submitted in partial satisfaction
of the requirements for the degree of

Doctor of Philosophy

in

Chemistry

by

Michael James Dahl

June 2015

Dissertation Committee:
Dr. Yadong Yin, Chairperson
Dr. Francisco Zaera
Dr. Pingyun Feng

The Dissertation of Michael James Dahl is approved:

Committee Chairperson

University of California, Riverside

Acknowledgements

It would not be possible to write this dissertation without considerable input and assistance from many of those with whom I have worked. First, I must thank my advisor, Professor Yadong Yin. Under his tutelage and instruction I have learned and grown a considerable amount during my PhD study. I am ever grateful to him and I am lucky to have had the opportunity to work under his guidance.

I must also thank my coauthors who I have frequently collaborated with and also learned much from. Additionally, I greatly appreciate the opportunity I have had to work with Dr. Ji Bong Joo, Dr. Chuanbo Gao, Dr. Xiaogang Han, Dr. Yongxing Hu, Dr. Qiao Zhang, Dr. Zhenda Lu, Dr. Le He, Dr. James Goebl, Dr. Geon Dae Moon, Dr. Yoon Jae Lee, Dr. Wenshou Wang, Dr. Na Li, Dr. Guoqing Wang, Dr. Anirban Das, Mingsheng Wang, Yiding Liu, Wenjing Xu, Yaocai Bai, Hongxia Yu, Qipeng Lu, Hongyan Liu, Xiaojing Wang, Ji Feng, Pritam Shankhari and all the other members, past and present, of the Yin Lab.

I would also like to thank a number of high school and undergraduate researchers who I have worked with considerably. I would like to thank Suzanne Dang, Kevin Nguyen, Fernando Castaneda, Victor Reyes, Noemi Garcia, Kelly Chau, Sarah Samaradivakara, Kyle Madrid and Andrea Noronha.

I would like to thank Professor Claire Xiong and her group at Boise State University for the opportunity to work alongside them and learn about battery cell fabrication as well as electrochemical synthesis and characterization of materials for energy production and storage.

Last but not least I must thank my family who have stood alongside me and supported me through this entire PhD study. I am grateful to my parents, Mike and Ramona, for encouraging my education and to my wife Cristina who has been with me though all the good times and the difficult times and has remained by my side. Without the support and understanding of my family, completion of this work would have been impossible.

ABSTRACT OF THE DISSERTATION

Synthesis and Utilization of Titanium (IV) Dioxide Nanomaterials and its Derivatives

by

Michael James Dahl

Doctor of Philosophy, Graduate Program in Chemistry
University of California, Riverside, June 2015
Dr. Yadong Yin, Chairperson

The controllable synthesis of colloidal titanium dioxide nanomaterials can yield materials with tunable properties and morphologies. The crystal grain size in nanoscale TiO_2 has been determined to be of importance to the photocatalytic activity and in my work the synthesis of anatase titania microspheres with controllable grain sizes was obtained by impregnating the porous networks of amorphous titania microspheres with silicate oligomers and calcining the composite. Controlling the degree of silicate impregnation enables the tuning of the grain size and surface area which yields an optimal sample for photocatalysis.

The optimization of coating TiO_2 onto nanoparticles and microspheres was next explored to create a simplified system which can easily coat a wide range of particles. The system consists of a mixed solution of titanium n-butoxide and ethylene glycol to create a titanium-glycolate precursor which can directly coat spherical and anisotropic metal nanoparticles as well as larger particles such as SiO_2 and polymer microspheres through an extension of this method. Further, the thickness of these coatings can be tuned and this coating can be crystallized into TiO_2 through refluxing in water for low crystallinity or calcination to obtain highly crystalline shells.

The titanium glycolate coating method can also incorporate additional metals into the precursor mixture to obtain a doped TiO_2 shell which can extend the light absorption into the visible range. Additionally, a study of the effect of the metal dopant on the crystalline grain size of the obtained product has been done as well. An increase or decrease in grain size relative to pure TiO_2 can be predicted by if the metal typically promotes or inhibits the anatase to rutile phase transition.

Hollow, metal incorporated TiO_2 can be produced by utilizing a sodium titanate intermediate which readily ion exchanges with target metals. This incorporation of metals can yield doped TiO_2 products with improved photocatalytic capabilities. Additionally, Fe^{3+} incorporated materials can be reduced to form a porous and magnetic iron oxide-TiO_2 composite structure. This combination of properties allows for the composite to be applied to the separation of phosphorylated proteins from a protein mixture.

Table of Contents

List of Figures

Chapter 1

Introduction to Titanium (IV) Dioxide Nanomaterials

1.1 Background of TiO_2

Titanium dioxide (titania, TiO_2) has been fervently researched over the past few decades due to its potential applications across many different areas. Thanks to its bulk properties, including high refractive index and ultraviolet (UV) light absorption, TiO_2 has seen considerable use as a white pigment in paint, food coloring, and personal care products such as a UV absorber in sunscreens.[1] These applications utilize TiO_2 across a wide range of sizes from hundreds of nanometers to several microns. Although these applications account for the majority of global TiO_2 consumption, its utilization in nanoscale research has primarily focused on its near semiconductor electronic properties.

Beginning with the initial discovery of the production of hydrogen from a TiO_2 anode under UV irradiation,[2] much work has been done, which has expanded the use of TiO_2 to numerous new applications. These applications range from photovoltaic cells[3] to photocatalysts for hydrogen production and environmental remediation,[4] as well as photoelectrochemical sensors.[5] Many other niche uses have also been studied, particularly in the medical and biological fields, where TiO_2 based nanomaterials have been investigated for *in vivo* imaging,[6,7] cancer therapy,[4,8] protein separation/purification,[9-11] and as bactericides.[12,13] Although applications as a pigment/UV absorber are typically possible using pure TiO_2, it has become clear that this is less feasible for applications utilizing photoelectrochemical properties, as well as a number of biological applications. Thus, much research has been dedicated to the construction of nanoscale TiO_2 composite materials.

1.1.1 Photocatalysis on TiO_2

The photoactivity of TiO_2 has been shown to be dependent on several key properties: crystal phase, surface area, exposed crystal facets, uncoordinated surface sites, defects in the lattice, and the degree of crystallinity. The two main polymorphs of TiO_2 which show the highest photoactivity are the anatase and rutile phases, which have typical reported bandgap values of 3.2 eV and 3.0 eV, respectively. The rutile phase is the thermodynamically stable phase while anatase is metastable, however the transformation of anatase to rutile typically does not begin to occur until reaching temperatures of at least 600 °C, though this can vary depending on the synthesis and processing conditions. Figure 1.1 displays the unit cells of both anatase and rutile in a ball-and-stick model. Although both polymorphs have a tetragonal crystal structure, the metastable anatase phase consists of a distorted octahedra of oxygen atoms surrounding the titanium atom which results in an expanded unit cell. Upon transformation to rutile, the unit cell volume decreases and the density increases as the octahedra become more ideally oriented and form a condensed unit cell.

Although the bandgap of rutile is narrower, the anatase phase is considered a more favorable photocatalyst. Typical studies of the capabilities of TiO_2 as a photocatalyst are done using a model dye degradation system, such as Rhodamine B, Methyl Orange, Methylene blue, et al. Figure 1.2 shows a general model for photocatalysis on anatase TiO_2 which takes place according to the following steps: (i)

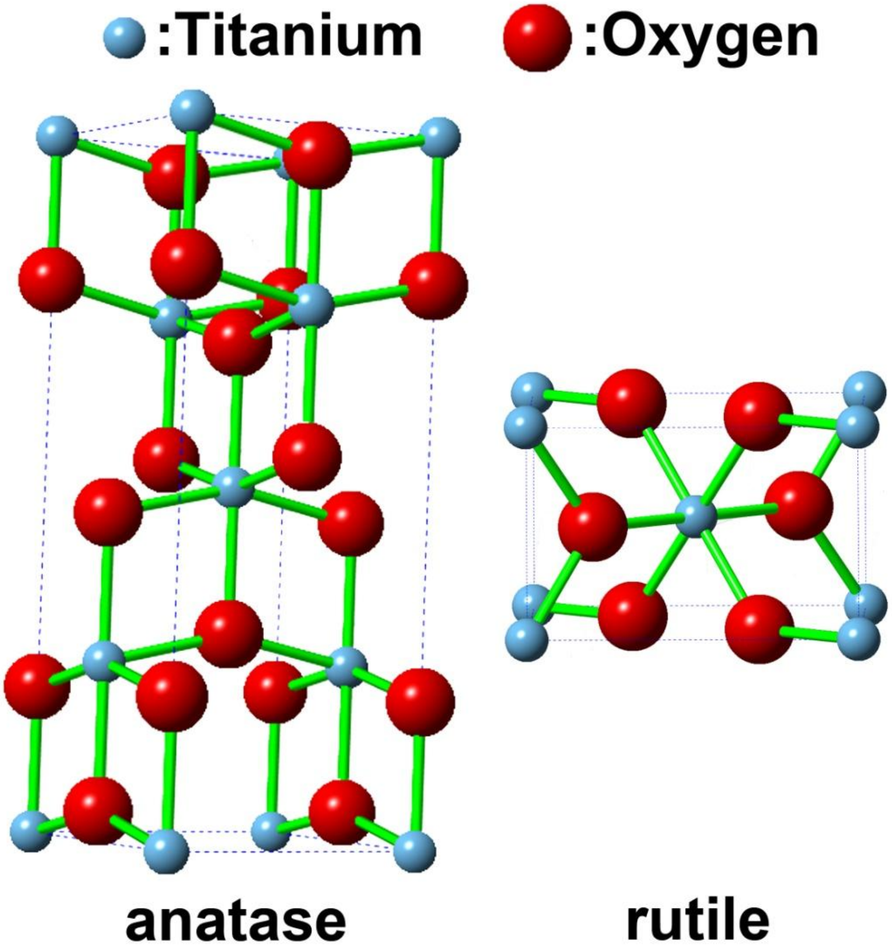

Figure 1.1 Unit cells for the two primary polymorphs of crystalline TiO_2: anatase and rutile.

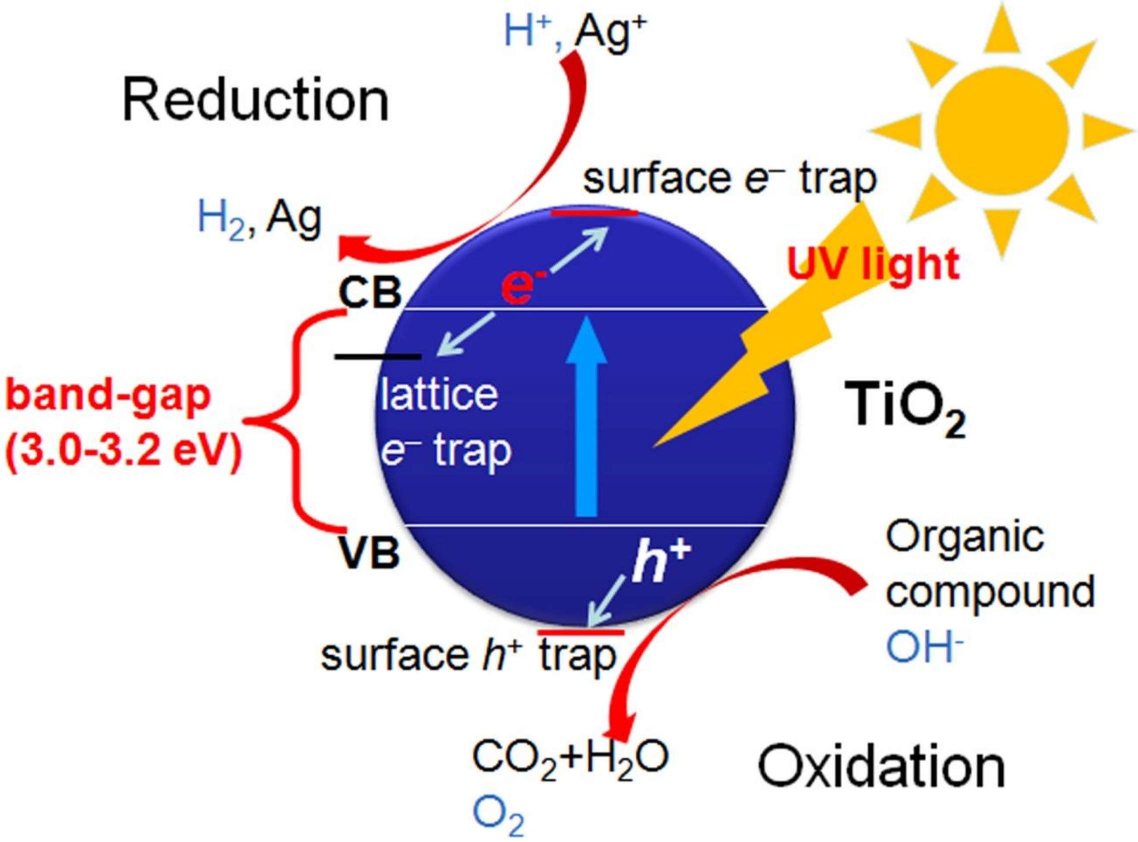

Figure 1.2 (a) General model of photocatalysis on TiO_2. Reactions occur in three steps: (i) absorption of photons greater than the band gap energy to produce an electron−hole pair; (ii) separation of charges and migration to the surface; (iii) redox reactions with adsorbed reactants.

light is absorbed by TiO_2 to produce an electron-hole pair; (ii) the charges migrate to the surface or boundary; (iii) the charge carriers (electrons and holes) react with adsorbed molecules and redox reactions occur. This ideal case assumes low charge recombination and easy charge migration to the surfaces. Further the rates of reaction can be affected by factors such as the surface area, which correlates to the number of active sites and the availability of surface coordination sites for reactant molecules to bind to. Anatase TiO_2 has been shown as preferable to rutile TiO_2 because it has a higher reduction potential and a slower rate of recombination of electron-hole pairs.[14,15] The higher relative rate of charge carrier recombination for rutile results from the generally larger crystal domains in rutile. In anatase TiO_2, charge separation can be enhanced by creation of features such as surface defects where electrons and holes can be trapped to prevent recombination. Additionally, EPR experiments have shown that there exists an electron trap site in the anatase lattice which exists at 0.8 eV below the conduction band.[16,17] It was later determined that the photogenerated holes are preferentially trapped on the surfaces whereas electrons become trapped within the lattice. A decrease in electron-hole recombination is achieved since the photogenerated holes can migrate to the surface and participate in oxidation reactions and the electrons will either be quenched or participate in redox reactions themselves. Anatase TiO_2 also has benefits which originate from the fact that it is easy to make at room temperature and it is metastable. Anatase TiO_2 can be made with more controllable crystal grain sizes, surface areas, and surface properties. The effect of the grain sizes is mentioned above, however it is also of note that the increase in grain sizes will generally decrease the active surface area and yield fewer binding sites for reactant molecules. These factors, which are frequently intertwined, are much easier to optimize in anatase TiO_2, yielding a superior photocatalyst.

1.1.2 Synthesis of Colloidal TiO_2

The colloidal synthesis of TiO_2 nanomaterials is most commonly done with either a titanium halide or titanium alkoxide. The advantage of colloidal synthesis is that it can be done in solution with simple equipment common to a chemistry lab and it can typically produce particles, gels, or coating materials. Figure 1.3a shows the typical sol-gel procedure where the following steps occur: (i) preparation of a solution containing titanium alkoxide precursors and solvent (generally alcohol); (ii) hydrolysis of the precursor combined with polycondensation of the monomers produced. Although the synthesis procedure can be modified to aim for a certain product, the final step can also play an important role in the product. Varying the processing can produce microspheres, aerogels and xerogels, or thin film coatings onto various substrates. The production of TiO_2 microspheres is well controlled and follows the standard LaMer diagram shown in Figure 1.3b. In the LaMer mechanism, the concentration of the monomer increases until C_{min} is reached, at which point self-nucleation of the monomer occurs and particles are formed. Once the monomer concentration decreases below C_{min}, the as formed particles consume the remaining monomers in order to grow larger. With titanium alkoxide precursors, there are a number of factors which can contribute to the nucleation and growth of TiO2 microspheres. One key component is the addition of surfactants such as hydroxypropyl cellulose (HPC) or polyvinylpyrrolidone (PVP) which can coordinate to the alkoxide precursor or the monomer and slow the nucleation. A similar method to

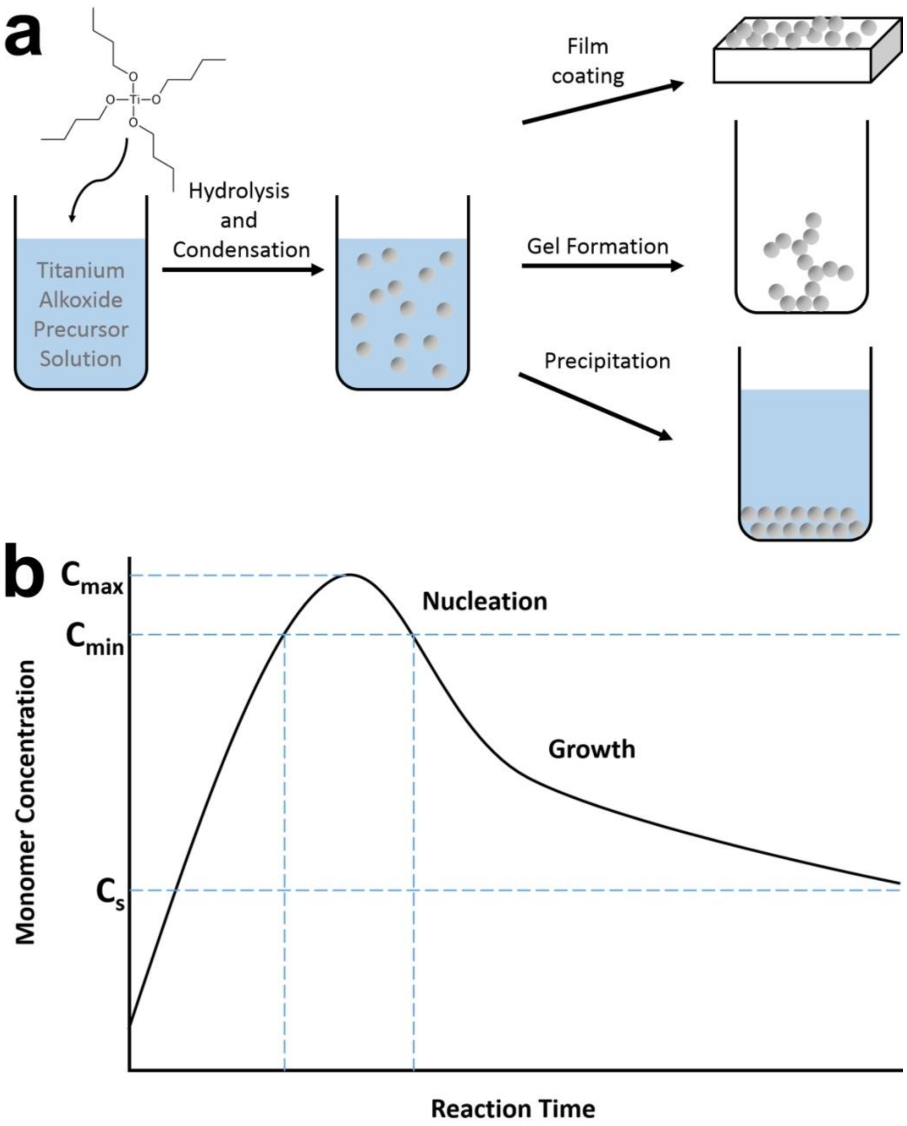

Figure 1.3 (a) General mechanism of the sol-gel process for titanium alkoxide precursors for products such as film coatings, gels, or particles. (b) Typical LaMer diagram depicting the nucleation and growth process for the formation of nanoparticles.

control the nucleation and growth is to stabilize the precursor through the addition of a chelating agent. Adding molecules such as urea or ethylene glycol to the precursor can also help control the nucleation of the particles to be produced.

1.2 Templated Colloidal TiO_2 Materials

1.2.1 Anodized Aluminum Oxide

Since the discovery of porous alumina templates made by the anodization of aluminum films, composites with these templates have been widely researched. The ease of deposition of precursors into the alumina pores allows for controlled height and composition of the deposited nanowires. The general method for synthesis of these nanowires follows a generally simple series of procedures. First an aluminum film is anodized to form a network of porous Al_2O_3 (alumina) nanotubes. This anodization can be repeated to control the pore width and height to better enhance the tuning of the later deposited material. The pores are then filled by deposition of the precursor material, e.g. titanium alkoxides, and the alumina/aluminum can be selectively dissolved to yield free nanorods/nanowires. Alternatively, commercial alumina templates with larger pore widths (200-250 nm in diameter) are available as filters. These templates can then be utilized in the same fashion for deposition and subsequent template removal. These templating methods have made the controllable synthesis of highly crystalline TiO_2 nanowires simple and reproducible.[18-22] Additionally, single crystal TiO_2 nanowires have been reported utilizing electrochemical oxidative hydrolysis and sol-gel deposition of TiO_2 precursors.[19,20]. This templating method has shown great utility for the creation of uniform nanowire arrays which can be utilized in applications such as dye-sensitized solar cells or photocatalysis.

1.2.2 Ordered Mesoporous Silica and Zeolites

Ordered templates based on silica such as MCM-41 and SBA-15, and zeolites have seen some usage as ‘hard’ templates for the synthesis of mesoporous TiO_2 materials. These templates allow for the synthesis of highly porous TiO_2 networks which can be used for applications in photocatalytic degradation of organic molecules, H_2 production, and Li^+ ion insertion for battery applications [23-28] Further, easy removal of the template can be done by chemical etching with NaOH or HF. Composites with zeolites were initially utilized more frequently due to their abundance and ease of purchase.[29-31] These composite structures were shown to enhance photocatalytic activity of reactions such as photooxidation of alcohols and water splitting. Later, with the synthesis and proliferation of ordered mesoporous silica structures like MCM-41 and SBA-15, the use of zeolites decreased. Utilizing typical titanium alkoxide deposition processes, there are four main types of guest assembling interactions inside ordered mesoporous silica (OMS) nanotubular mesopores: (i) ensemble of nanoparticles with diameter less than that of OMS mesopores; (ii) isolated nanoparticles of dimension comparable with OMS mesopore diameter; (iii) guest phase layer where the alkoxide uniformly coats the inside of the pores; (iv) combination of guest nanoparticles inside the OMS mesopores with large guest particles at the outer surface of OMS crystals.

1.2.3 Core@Shell Colloidal TiO_2 Materials

Template mediated syntheses have been utilized quite regularly in recent years to create layered composite TiO_2 structures with well controlled properties. The synthesis of these materials typically involves the sequential process of preparation of the core material template followed by deposition of the shell materials on the surface of the templates, usually via a sol-gel process. A number of core@TiO_2 shell composites have been synthesized using core materials ranging from metals, to metal oxides to carbons such as nanotubes. The uniformity of these samples is not always optimal but the array of materials which have been coated yields composites with a number or properties and potential applications such as in sensors, catalysis, and battery fabrication.

One template material that has been utilized readily over the past decade is polystyrene (PS) beads due to its availability in a wide range of sizes either through synthesis or from commercial sources.[32-36] Polystyrene templates have been of use because of the relative ease of removal either through chemical dissolution or by calcination. Polystyrene beads can be assembled into a crystalline array, followed by infiltration with a titanium alkoxide precursor or they can be coated directly in a colloidal dispersion. Both types of templates can be removed by calcination or dissolution in a solvent such as toluene in order to obtain hollow TiO_2 spheres. The difficulty with removal by calcination however is that although it results in crystalline TiO_2, the product material tends to be structurally degraded, especially in the case of hollow shells. In addition to PS beads, TiO_2 has also been deposited on other carbonaceous templates

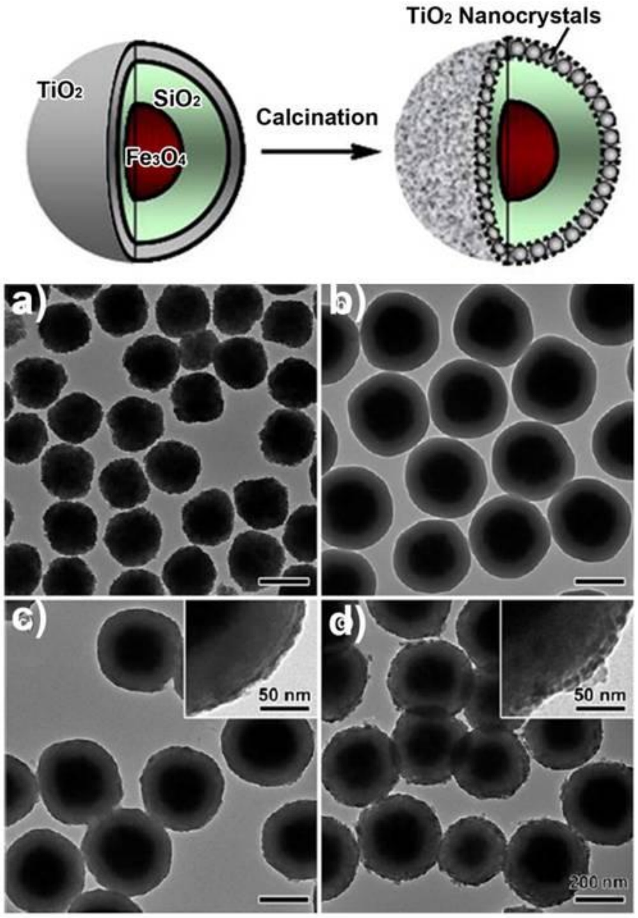

Figure 1.4 (Top) Scheme of as-synthesized composite structure. (Bottom) TEM images of (a) Fe_3O_4, (b) Fe_3O_4/SiO_2, (c) $Fe_3O_4/ SiO_2/TiO_2$, and (d) calcined $Fe_3O_4/SiO_2/TiO_2$ particles. Insets in c and d are magnified images of portions of the composite particles showing the morphological change in the TiO_2 shell due to calcination.

which can easily be burned away to reveal a hollow TiO_2 structure. Most prominently, glucose can be hydrothermally treated to form colloidal carbon spheres.[37] Much like polystyrene beads, these carbon spheres can then be coated with TiO_2 via a sol-gel process, followed by calcination to remove the carbon core.[38] Although good control of the coating of TiO_2 onto PS beads and glucose has been demonstrated, it has fallen out of favor as compared to other templates such as silica.

The coating of TiO_2 onto silica templates has been widely demonstrated over the past two decades with varying degrees of control.[39-42] More recently, our group has shown an ability to extend this to include other materials with the core@shell structure. One such example, as shown in Figure 1.4, is the addition of a superparamagnetic iron oxide colloidal nanocrystal cluster in order to facilitate the magnetic recoverability of the composite from reaction media. This hierarchical structure was synthesized by using superparamagnetic Fe_3O_4 cores (Figure 1.4a) which were first coated by a layer of SiO_2 by a modified Stöber process (Figure 1.4b). This was followed by a coating with TiO_2 using titanium (IV) *n*-butoxide in an ethanolic solution to obtain an $Fe_3O_4@SiO_2@TiO_2$ composite as shown in Figure 1.4c.[43] Finally, the composite was calcined at 500 °C to crystallize the TiO_2 shell. As shown in Figure 1.4d, the as calcined structures are uniform and have well defined morphologies with anatase crystalline TiO_2 on the surface. The composites also showed good photocatalytic activity for the degradation of RhB under UV irradiation which exceeded that of P25. Further, the magnetic recoverability and good cyclability allowed for a catalyst which showed little drop in efficiency over 18 cycles.

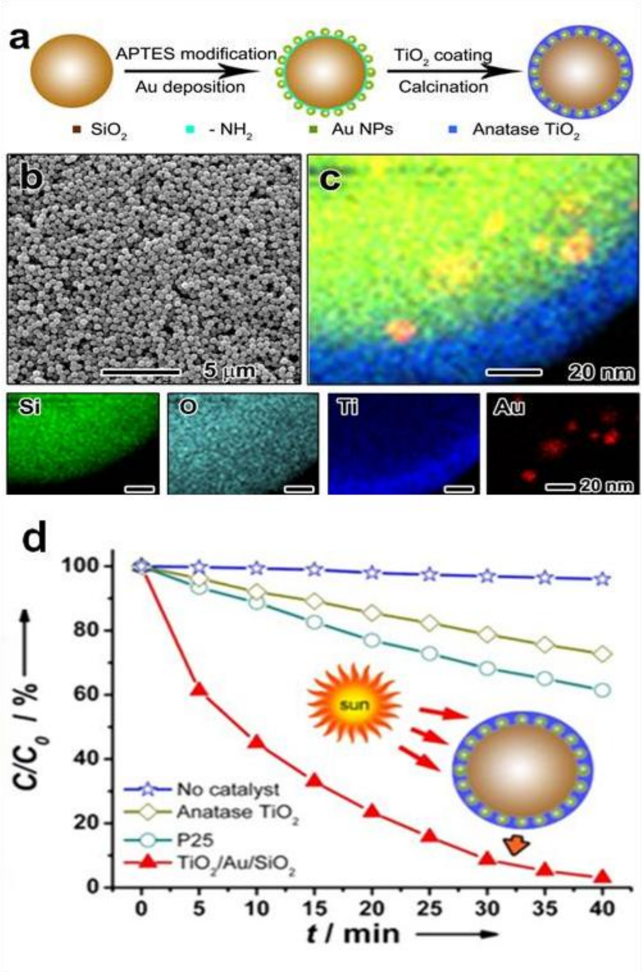

Figure 1.5 (a) Schematic illustration of the fabrication process of the sandwich-structured SiO_2/Au/TiO_2 photocatalyst. (b) Typical SEM image of the composite photocatalyst. (c) Elemental mapping of a single particle with the distribution of individual elements shown in the bottom row. (d) Photodegradation of RhB under direct sunlight illumination.

The addition of noble metal nanoparticles to a SiO_2@TiO_2 core@shell composite has also been recently demonstrated by our group. This composite structure, a core-shell hierarchical SiO_2@Au@TiO_2 composite, was developed to increase the photocatalytic activity for the degradation of Rhodamine B (RhB) dye under visible light.[44] The composite was synthesized starting with a SiO_2 core, to which Au nanoparticles were chemically attached via interactions with an amine-modified SiO_2 surface. The composite was then coated with TiO_2 and calcined at 500 °C as shown in the scheme in Figure 1.5a. Figure 1.5c shows the energy dispersive X-ray (EDX) elemental mapping confirming the "sandwich" structure where the Au nanoparticles are located in between the SiO_2 core and TiO_2 layer. This composite showed impressive photocatalytic activity for the degradation of RhB dye under direct solar irradiation as shown in Figure 1.5d. The composite completely degraded the dye in 40 minutes whereas, in the same time, commercial P25 had only degraded ~38% of the dye. Further, the optimal catalyst showed a significant decrease in the amount of gold necessary compared to many other catalysts as the optimal loading amount was only 0.10 wt. %. The catalyst also showed improvement by nitrogen-doping of the TiO_2 shell which was supposedly doped by the decomposition of the amine layer when the composite was calcined.

1.3 Silica Protected Calcination

One significant drawback for many of these early TiO_2 coated composites is that after crystallization at high temperature and removal of the template (generally SiO_2 or PS), the TiO_2 shell would collapse. This is likely due to the large degree of structural reorganization that occurs upon high temperature crystallization of the amorphous shell.

Once the core is removed, the support for these crystals is gone and the shell falls apart. Interestingly, if a spacer of different composition, such as PS or SnO_2, is placed between the core and the TiO_2 layer the shell morphology can be retained after calcination and removal of either the spacer or the SiO_2 core.[45,46] Unfortunately this will result in materials which are no longer pure phase TiO_2.

1.3.1 Silica Protection of Metal Nanoparticles

The utilization of silica as a protective oxide layer against corrosion has been shown as effective on materials such as aluminum since it prevents oxidation and acid corrosion. An interesting use of silica on the nanoscale is to act as a protection layer on the surface of a material to prevent significant growth of nanomaterials upon calcination. One such example illustrates how a silica overlayer, produced from sol-gel processes, can prevent the sintering of metal nanoparticles.[47] Figure 1.6 shows TEM images of Pt nanoparticles deposited onto a silica sphere which is either then coated again (covered) or not (naked). Upon calcination, the naked composite particles show a significant amount of sintering of the Pt nanoparticles on the silica surface. This behavior is quite common of bare metal nanoparticles and leads to loss of optimal size for catalysis. Conversely, the Pt particles which were coated with an additional silica layer showed little to no growth in size upon calcination. The Pt particles could then be exposed through a mild base etching to remove the protective silica layer. A similar phenomenon has also been applied to gold@silver core shell nanoparticles in order to facilitate alloy particles.[48] The silica simultaneously protects against sintering while also providing a confined space for the two metals to alloy together.

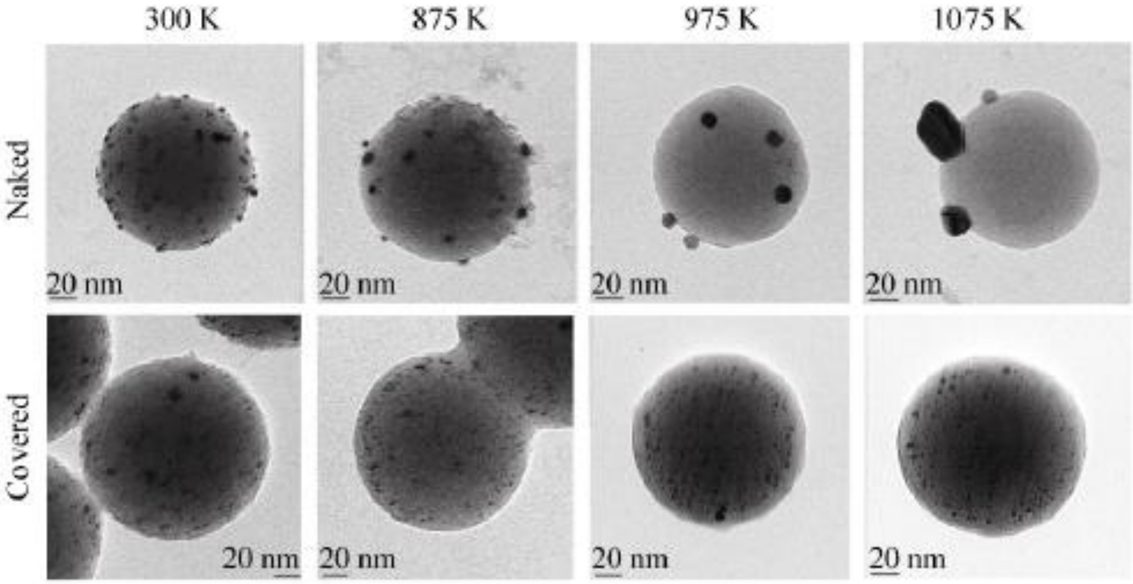

Figure 1.6 TEM images of Pt nanoparticle/SiO_2 bead catalysts, “naked”)i.e., uncovered, top row) and covered with a layer of mesoporous silica (bottom row) after calcination at, from left to right, 300, 875, 975, and 1075 K. Sintering is already significant by 875 K in the naked samples, whereas no appreciable sintering is observed in the encapsulated samples even after calcination at 1075 K.

1.3.2 Silica Protection of TiO_2

The principles which are behind the silica protection of metal nanoparticles in order to prevent sintering can also be applied to TiO_2 as well. The crystallization of amorphous TiO_2 is highly reconstructive and leads to a ripening of crystallites to form large crystal grains. Unfortunately in order to best utilize TiO_2, it must be as crystalline as possible which typically implies calcination temperatures of greater than 600 °C. Under these conditions, if the TiO_2 is present as the top layer in a core@shell composite, this reconstruction results in structural degradation of the shell layer and if the core is removed, the material breaks apart entirely. Although this degradation can be avoided with lower calcination temperatures, the resulting product will have sub-par catalytic performance. Additionally, if a SiO_2 core is removed through sodium hydroxide etching prior to calcination, the resulting sodiated titania undergoes a rapid crystallization and leads to morphology loss as well as formation of sodium titanate. Figure 1.7 shows TEM images and XRD diffractograms illustrating these different potential products. In Figure 1.7a we see hollow amorphous shells prepared by etching without calcination (TiO_2-E) whereas Figures 1.7b and 1.7c show samples (TiO_2-E-C-500 and TiO_2-E-C-800) after calcination at 500 and 800 °C, respectively. The sample in Figure 1.7b retains its hollow morphology however it is still amorphous whereas in 1.7c the morphology has been completely degraded and the product is sodium titanate. Figure 1.7d (TiO_2-C-E-500) shows a SiO_2@TiO_2 sample calcined to 500 °C followed by etching. Although the XRD diffractogram indicates a well crystallized anatase phase, it is apparent that the hollow morphology is already becoming degraded. Here is where the addition of a silica

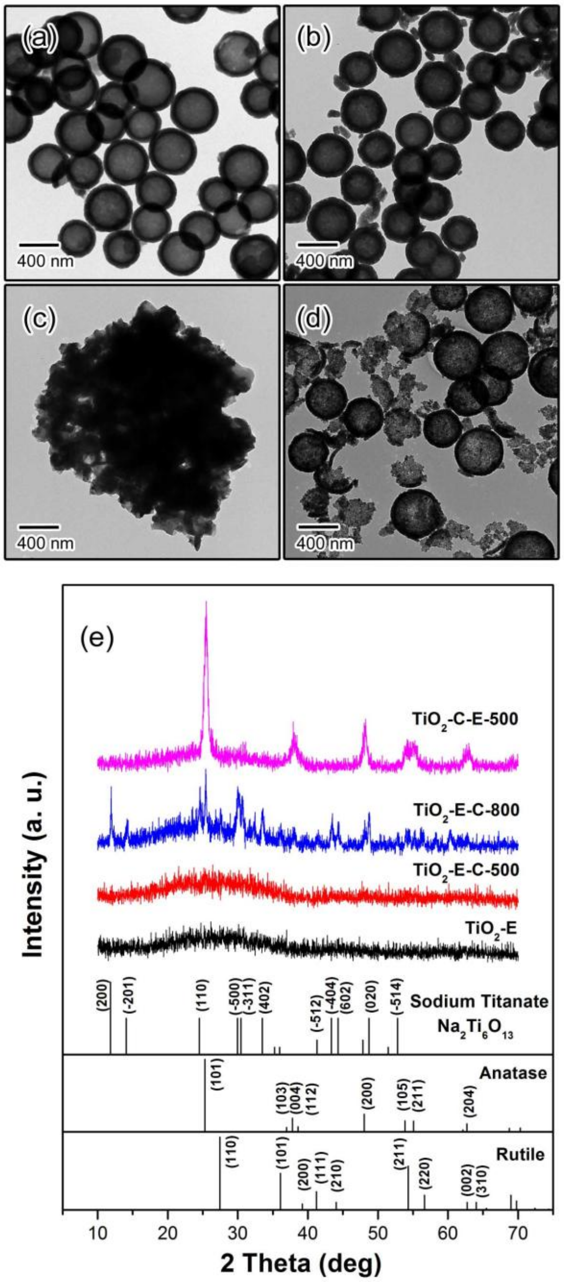

Figure 1.7 TEM images (a) ~ (d) and XRD patterns (e) of the prepared TiO_2 samples: (a) TiO_2-E, (b) TiO_2-E-C-500, (c) TiO_2-E-C-800 and (d) TiO_2-C-E-500.

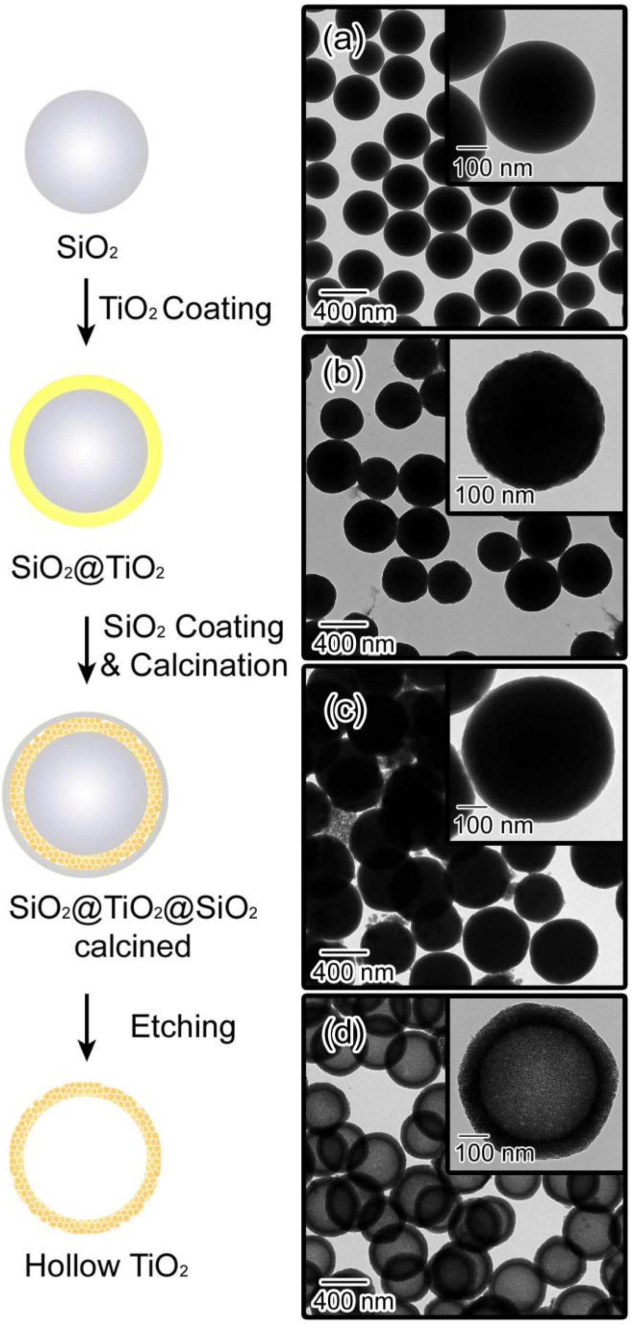

Figure 1.8 Schematic illustration of procedures of silica-protected calcination for fabrication of mesoporous hollow TiO_2 (left) and corresponding TEM images of each of the synthetic steps: (a) SiO_2, (b) $SiO_2@TiO_2$, (c) $SiO_2@TiO_2@SiO_2$ after calcination and (d) final hollow TiO_2 after template removal by base etching.

overlayer for protection of the TiO_2 shell becomes of importance. Our group has demonstrated the function of this silica overlayer by utilizing it to form TiO_2 materials which, after calcination and etching, have a well maintained hollow shell morphology and anatase crystalline phase.[49] Figure 1.8 shows the scheme of the synthetic procedures in addition to TEM images corresponding to each step. One consequence of the silica overlayer protection however is that although the diffractogram shows anatase crystalline phase, it is a relatively low crystallinity with grain sizes of ~ 5nm, as measured by the Scherrer Equation. Although a significant improvement in morphology was shown, the photocatalytic activity was still minimal due to the small grains yielding more sites for recombination of photogenerated charge carriers.

1.4 Use of Colloidal TiO_2 in This Work

My PhD research has focused on studying the properties of TiO_2 composites finding simple and robust synthetic methods for production of TiO_2 materials and its derivatives. Although the synthesis of colloidal TiO_2 is well developed, many of the more recent advances in nanoscale materials have occurred in systems that are either not easily scaled up or cannot extend beyond the system it was designed for. Additionally my research has focused on various applications of TiO_2 based materials including catalysis, bioseparation, and lithium ion batteries. This includes exploring different synthetic methods for preparing TiO_2, modifying TiO_2, and transforming TiO_2 into titanate derivatives.

The ability of SiO_2 to act as a protection layer for TiO_2 layers in order to facilitate controllable properties after calcination had been studied but not fully investigated.

Notably, the prevention of crystalline phase transition as well as the effect on the physicochemical properties required further attention. Therefore, a systematic study utilizing colloidal TiO_2 microspheres was designed. Although the hollow particles are not utilized, the synthetic procedures were similar and the components were the same. It was determined that to better control the ratios of SiO_2 to TiO_2, starting with colloidal TiO_2 and adding SiO_2 precursor was a more reliable system. Additionally, using TiO_2 microspheres would allow for the determination of the extent of the SiO_2 impregnation into the amorphous TiO_2 network. TiO_2 shells only give thicknesses of tens of nanometers whereas TiO_2 microspheres of ~300 nm were used instead. The results of this process indicate that the SiO_2 can affect the entirety of the TiO_2 matrix rather than only near the surface. Further, the colloidal TiO_2 microspheres were impregnated with varying concentrations of SiO_2 precursor in order to track the changes which occur after calcination of the composite. By varying the concentrations, we can alter to what extent the SiO_2 can protect the TiO_2. As a result, we can see the grain size and surface area, which are intertwined, changing with respect to amount of SiO_2 precursor added. The details of this research are shown in Chapter 2.

Next, I developed a procedure for coating TiO_2 onto materials of various sizes, from microspheres to nanoparticles. The coating of TiO_2 shells onto sub-micron sized particles has been widely studied in recent years with much success occurring in the coating of templates with sizes above 50 nm. Direct coating onto particles below this size has been difficult to attain especially with good control over properties such as thickness and TiO_2 crystallinity. To facilitate coating a wider array of materials, stabilization of the

TiO_2 precursor was desired. To do this, a system consisting of a mixed solution of titanium n-butoxide and ethylene glycol was made in order to create a titanium glycolate precursor for coating TiO_2 on aqueous nanoparticles. The titanium glycolate precursor coating is particularly useful due to its ability to coat materials lacking strong polymer or ligand surfactants which are frequently necessary to facilitate typical titania coatings. Metal nanoparticles ranging from citrate-stabilized gold and silver particles to gold nanorods and silver nanoplates, can all be directly coated and exhibit a corresponding shift in the surface plasmon resonance. Additionally, coatings on larger particles, such as SiO_2 microspheres and polymer spheres, can be done through a simple extension of this method. Further the thickness of these coatings can be tuned from a few nanometers to ~30 nm through subsequent coatings. This coating can be crystallized to TiO_2 through refluxing in water for low crystallinity or calcination to obtain highly crystalline shells. This procedure can be very useful for the production of TiO_2 coatings with tunable thickness and crystallinity as well as for further study on the effect of TiO_2 coatings on nanoparticles.

Additionally, the titanium glycolate precursor facilitates the doping of metal ions into the TiO_2 shell layer through dissolution of a metal salt into the ethylene glycol-titanium n-butoxide mixture. This was demonstrated with the case of a TiO_2 shell layer onto SiO_2 so that removal of the template could be done and the products obtained were metal doped TiO_2 hollow shells, which made characterization of and comparison to pure TiO_2 easier. This study was done not only to bring the bandgap of the resulting TiO_2 into the visible region, but also to look at how the change in grain size after calcination can be changed based on the identity of the metal ion added. This was compared to how metal ions can inhibit or promote the anatase to rutile phase transition. The detailed results of this research can be found in Chapter 3.

One advantage of the colloidal processing of TiO_2 which has only been mildly explored is the conversion of amorphous TiO_2 to titanates. Although it was noticed in some of our early experiments that SiO_2@TiO_2 core@shell composites which had been treated with sodium hydroxide could form crystalline sodium titanate after calcination, the utilization of such material was not immediate. These alkali metal titanate materials are known for their capacities as cation exchange materials. Synthesis of colloidal SiO_2@TiO_2 core@shell composites followed by refluxing in an aqueous sodium hydroxide solution resulted in amorphous sodium titanate. This sodium titanate intermediate could then be refluxed with a desired metal ion source in order to remove the sodium ions and replace them with the target metal ion. In addition, the process of removal of the sodium titanate and the resulting water refluxing yielded a crystalline TiO_2 product, which was now infiltrated, or doped, with the metal ion. The results showed a significant amount of metal ion retention when utilizing typical transition metal ions such as Cu^{2+}, Ni^{2+}, and Fe^{3+}. These metal doped TiO_2 materials could then be used for applications common to TiO_2. The Cu^{2+} incorporated TiO_2 were investigated for their capabilities towards the visible light degradation of Rhodamine B dye. The Fe^{3+} exchanged materials in particular could be calcined under a flowing hydrogen atmosphere in order to partially reduce the Fe^{3+} and yield a magnetic iron oxide-TiO_2 composite. This magnetically responsive composite could then be used for the separation of phosphorylated proteins from non-phosphorylated proteins. Further, the scalability of this procedure could yield gram scale quantities of the target material, which has been uncommon when making composites of this nature. The details of research on these titanate based materials are found in Chapter 4.

1.5 References

(1) Robichaud, C. O.; Uyar, A. E.; Darby, M. R.; Zucker, L. G.; Wiesner, M. R. *Environ. Sci. Technol.* **2009**, *43*, 4227.

(2) Fujishima, A.; Honda, K. *Nature* **1972**, *238*, 37.

(3) O'Regan, B.; Gratzel, M. *Nature* **1991**, *353*, 737.

(4) Fujishima, A.; Rao, T. N.; Tryk, D. A. *J. Photochem. Photobiol., C* **2000**, *1*, 1.

(5) Yang, L.; Luo, S.; Cai, Q.; Yao, S. *Chin. Sci. Bull.* **2010**, *55*, 331.

(6) Endres, P. J.; Paunesku, T.; Vogt, S.; Meade, T. J.; Woloschak, G. E. *J. Am. Chem. Soc.* **2007**, *129*, 15760.

(7) Smith, L.; Kuncic, Z.; Ostrikov, K.; Kumar, S. *J. Nanomaterials* **2012**, *2012*, 1.

(8) Yamaguchi, S.; Kobayashi, H.; Narita, T.; Kanehira, K.; Sonezaki, S.; Kubota, Y.; Terasaka, S.; Iwasaki, Y. *Photochem. Photobiol.* **2010**, *86*, 964.

(9) Chen, C.-T.; Chen, Y.-C. *Anal. Chem.* **2005**, *77*, 5912.

(10) Lu, Z.; Ye, M.; Li, N.; Zhong, W.; Yin, Y. *Angew. Chem.* **2010**, *122*, 1906.

(11) Lu, J.; Wang, M.; Deng, C.; Zhang, X. *Talanta* **2013**, *105*, 20.

(12) Sunada, K.; Kikuchi, Y.; Hashimoto, K.; Fujishima, A. *Environ. Sci. Technol.* **1998**, *32*, 726.

(13) McCullagh, C.; Robertson, J. C.; Bahnemann, D.; Robertson, P. J. *Res. Chem. Intermed.* **2007**, *33*, 359.

(14) Fox, M. A.; Dulay, M. T. *Chem. Rev.* **1993**, *93*, 341.

(15) Sclafani, A.; Herrmann, J. M. *J. Phys. Chem.* **1996**, *100*, 13655.

(16) Leytner, S.; Hupp, J. T. *Chem. Phys. Lett.* **2000**, *330*, 231.

(17) Hurum, D. C.; Agrios, A. G.; Gray, K. A.; Rajh, T.; Thurnauer, M. C. *J. Phys. Chem. B* **2003**, *107*, 4545.

(18) Hoyer, P. *Langmuir* **1996**, *12*, 1411.

(19) Zhang, X. Y.; Zhang, L. D.; Chen, W.; Meng, G. W.; Zheng, M. J.; Zhao, L. X.; Phillipp, F. *Chem. Mater.* **2001**, *13*, 2511.

(20) Miao, Z.; Xu, D.; Ouyang, J.; Guo, G.; Zhao, X.; Tang, Y. *Nano Lett.* **2002**, *2*, 717.

(21) Lee, J.; Jho, J. Y. *Sol. Energy Mater. Sol. Cells* **2011**, *95*, 3152.

(22) Liang, Y.-C.; Wang, C.-C.; Kei, C.-C.; Hsueh, Y.-C.; Cho, W.-H.; Perng, T.-P. *J. Phys. Chem. C* **2011**, *115*, 9498.

(23) Aronson, B. J.; Blanford, C. F.; Stein, A. *Chem. Mater.* **1997**, *9*, 2842.

(24) Bhattacharyya, A.; Kawi, S.; Ray, M. B. *Catal. Today* **2004**, *98*, 431.

(25) López-Muñoz, M.-J.; Grieken, R. v.; Aguado, J.; Marugán, J. *Catal. Today* **2005**, *101*, 307.

(26) Zhang, Z.; Zuo, F.; Feng, P. *J. Mater. Chem.* **2010**, *20*, 2206.

(27) Peng, R.; Zhao, D.; Dimitrijevic, N. M.; Rajh, T.; Koodali, R. T. *J. Phys. Chem. C* **2011**, *116*, 1605.

(28) Yue, W.; Randorn, C.; Attidekou, P. S.; Su, Z.; Irvine, J. T. S.; Zhou, W. *Adv. Funct. Mater.* **2009**, *19*, 2826.

(29) Green, K. J.; Rudham, R. *J. Chem. Soc., Faraday Trans.* **1993**, *89*, 1867.

(30) Liu, X.; Iu, K.-K.; Thomas, J. K. *J. Chem. Soc., Faraday Trans.* **1993**, *89*, 1861.

(31) Xu, Y.; Langford, C. H. *J. Phys. Chem.* **1995**, *99*, 11501.

(32) Shiho, H.; Kawahashi, N. *Colloid. Polym. Sci.* **2000**, *278*, 270.

(33) Zhong, Z.; Yin, Y.; Gates, B.; Xia, Y. *Adv. Mater.* **2000**, *12*, 206.

(34) Caruso, R. A.; Susha, A.; Caruso, F. *Chem. Mater.* **2001**, *13*, 400.

(35) Imhof, A. *Langmuir* **2001**, *17*, 3579.

(36) Agrawal, M.; Pich, A.; Zafeiropoulos, N.; Stamm, M. *Colloid. Polym. Sci.* **2008**, *286*, 593.

(37) Sun, X.; Li, Y. *Angew. Chem. Int. Ed.* **2004**, *43*, 597.

(38) Ao, Y.; Xu, J.; Fu, D.; Yuan, C. *Catal. Commun.* **2008**, *9*, 2574.

(39) Srinivasan, S.; Datye, A. K.; Hampden-Smith, M.; Wachs, I. E.; Deo, G.; Jehng, J. M.; Turek, A. M.; Peden, C. H. F. *J. Catal.* **1991**, *131*, 260.

(40) Hsu, W. P.; Yu, R.; Matijević, E. *J. Colloid Interf. Sci.* **1993**, *156*, 56.

(41) Hanprasopwattana, A.; Srinivasan, S.; Sault, A. G.; Datye, A. K. *Langmuir* **1996**, *12*, 3173.

(42) Guo, X.-C.; Dong, P. *Langmuir* **1999**, *15*, 5535.

(43) Ye, M.; Zhang, Q.; Hu, Y.; Ge, J.; Lu, Z.; He, L.; Chen, Z.; Yin, Y. *Chem. Eur. J.* **2010**, *16*, 6243.

(44) Zhang, Q.; Lima, D. Q.; Lee, I.; Zaera, F.; Chi, M.; Yin, Y. *Angew. Chem.* **2011**, *123*, 7226.

(45) Chen, J. S.; Luan, D.; Li, C. M.; Boey, F. Y. C.; Qiao, S.; Lou, X. W. *Chem. Commun.* **2010**, *46*, 8252.

(46) Zhang, K.; Zhang, X.; Chen, H.; Chen, X.; Zheng, L.; Zhang, J.; Yang, B. *Langmuir* **2004**, *20*, 11312.

(47) Lee, I.; Zhang, Q.; Ge, J.; Yin, Y.; Zaera, F. *Nano Res.* **2011**, *4*, 115.

(48) Gao, C.; Hu, Y.; Wang, M.; Chi, M.; Yin, Y. *J. Am. Chem. Soc.* **2014**, *136*, 7474.

(49) Joo, J. B.; Zhang, Q.; Lee, I.; Dahl, M.; Zaera, F.; Yin, Y. *Adv. Funct. Mater.* **2012**, *22*, 166.

Chapter 2

Control of the Crystallinity in TiO_2 Microspheres Through Silica Impregnation

2.1 Introduction

The utilization of solar radiation as a renewable source of energy has been under constant study in order to decrease fossil fuel consumption. Titania (TiO_2) has been one of the most frequently studied semiconductor materials for energy harvesting and photocatalysis because of its stability, low toxicity, and abundance[1,2]. Since the initial demonstrations of TiO_2 as a hydrogen producing catalyst under UV irradiation by Honda and Fujishima,[3] various developments have been made to both increase the efficiency of these materials and to extend the photocatalytic activity into the visible spectrum. In addition to the study of its potential for hydrogen production and water splitting,[4,5] the photocatalytic activity of TiO_2 has been widely studied for its use as a promising catalyst for environmental remediation.[6-9]

The activity of TiO_2 has been shown to be dependent on different properties of the material including crystal phase, surface area, grain size, and the degree of crystallinity.[10] Compared with rutile phase,[11] the anatase phase has been shown to be superior because of a slower charge carrier recombination rate, which improves performance.[12,13] One factor which decreases the recombination rate is a higher surface area, which increases the number of localized states where an electron is between the conduction and valence band. The charge carrier can then be localized near the surface where terminal bonds provide a means for charge separation and can trap the charge carrier.[14,15] These trapped charge carriers can finally react with adsorbed species rather than recombine. However in semiconductor materials with too large of a surface area, the crystal grain size is too small to prevent a quick charge carrier recombination. In photoelectrochemical cells when an n-type semiconductor is in contact with an electrolyte solution, electron transfer will occur at the surface until the Fermi level is equal to the chemical potential of the solution. This causes a potential drop between the surface and the bulk, which is known as band bending. In n-type TiO_2 the Fermi level is normally higher than the chemical potential of the solution and the bands are bent upwards with respect to the bulk. As a result excess charge carriers cannot exist at the surface and will instead recombine. As a result, a large surface area may increase localized states, however once equilibrium has been reached the recombination process cannot be avoided.[14] It is therefore critically important to control the crystallinity while maintaining a high surface area of the photocatalysts.

Various methods have been used in order to increase the grain size of colloidal TiO_2 and determine the resulting optimal properties including the addition of dopants, high temperature calcination, or the addition of surfactants.[16-18] High surface area crystalline TiO_2 has also been obtained through the synthesis of clusters of individual TiO_2 nanocrystals.[19] The addition of metal oxides from alkoxide precursors has provided a simple way to change the surface area and grain size upon synthesis. Precursors ranging from zirconium isopropoxide, aluminium sec-butoxide, and tetraethyl orthosilicate (TEOS) have been hydrolyzed in the presence of TiO_2 gels in order to affect the crystallization.[20] SiO_2, from the hydrolysis of TEOS, has been commonly used due to its ability to inhibit anatase grain growth as well as its easy removal from the resultant composite material. The inhibition of grain growth is believed to occur by the following mechanism: upon heating the silica-titania composite, the silicate species within the amorphous TiO_2 structure is slowly expelled to the surface of the grain. As the silica is expelled out of the TiO_2 matrix it forms a layer of SiO_2 around the grain, preventing further growth.[21] It then can be assumed that varying the amount of silicate present will change the point at which the grain is fully covered with SiO_2, thus allowing different grain sizes to grow. Different methods have incorporated SiO_2 to produce crystalline TiO_2 ranging from a co-hydrolysis method, mixing already prepared powders, or hydrothermal growth of TiO_2 in a SiO_2 template.[22-25] Few of these however have provided a systematic study of the system and additionally many of the products form gels which retain no control of size and will precipitate upon standing when in aqueous solutions.

Recently Joo et al. synthesized mesoporous hollow TiO_2 shells with small crystal grain sizes of ~4 nm with surface areas >300 m^2/g through the synthesis of core-shell structure $SiO_2@TiO_2@SiO_2$, calcination, then removal of the template SiO_2.[26] Although the shell structures had high surface areas, the grain size still exhibited somewhat lower activity for the degradation of organic molecules because of the small grain size. The inhibition of grain growth is believed to result from the silicate species from the hydrolyzed precursor penetrating into the TiO_2 matrix and preventing grain growth upon calcination. A partial etching followed by recalcination process was then developed in order to increase the grain size while still yielding a dispersible shell structure with a high surface area.[27] This method showed an increase in photocatalytic activity due to the resultant grain sizes which were as large as 14 nm. Grain sizes larger than this were grown however it was not possible to maintain the shell structure.

In this work we report the use of TiO_2 microspheres as the model system due to its microporous nature,[28] which allows the impregnation of silicate species. The as-prepared TiO_2-SiO_2 composites were subsequently calcined to obtain structures with varying grain sizes, which can be fully controlled by the amount of silicate impregnation. The removal of silica by etching with a NaOH solution will then yield non-aggregated crystalline microspheres with roughly spherical morphology and good water dispersibility. As expected, with an increase in crystallinity the surface area of the microspheres decreases as well as the overall porosity of the structure. A systematic study allows us to find optimized parameters between surface area and crystallinity, yielding a peak photocatalytic performance.

2.2 Experimental

2.2.1 Synthesis of Colloidal TiO_2

Colloidal titania particles were made using established procedures.[28,29] Briefly, hydroxypropyl cellulose (HPC, 0.2 g) was dissolved in an ethanol (50 mL) and deionized water (0.3 mL) solution. To this solution tetrabutyl orthotitanate (TBOT, 97%, 0.85 mL) was added and mixed vigorously until the solution became cloudy at which point stirring was ceased and the solution was left to age for 3 h. The resulting microspheres were isolated through centrifugation and washed three times with ethanol, once with water and finally dispersed in 20 mL of deionized water. To form a complete silica coating on the TiO_2 microsphere, the solution was stirred overnight with polyvinylpyrrolidone (PVP, Mw ~ 40,000, 0.2 g) to allow adsorption onto the TiO_2 surface. The solution was then washed and re-dispersed in 10 mL ethanol.

2.2.2 Silica Impregnation into Colloidal TiO_2

The PVP coated TiO_2 colloid was added to a solution with tetraethyl orthosilicate (TEOS, 99%, 0.86 mL), deionized water (4.3 mL) and ethanol (13 mL). The solution was stirred for three minutes and an aqueous ammonia solution (26%, 0.62 mL) was added and the solution was stirred for three hours. The samples were then collected by centrifugation and washed with ethanol three times. For impregnation without coating, the as-obtained TiO_2 microspheres were dispersed in 10mL ethanol and added to a solution of deionized water (4.3 mL) and ethanol (13 mL). To obtain different degrees of crystallization, different volumes of TEOS are added to this solution. The concentration of TEOS added was calculated based on the final volume of the solution. Upon stirring for three minutes an aqueous solution of ammonia (26%, 0.62 mL) was added and the solution was stirred for 4 h after which it was centrifuged and washed with ethanol three times.

2.2.3 Crystallization of TiO_2 and Removal of SiO_2

To crystallize the amorphous TiO_2 microspheres, the samples were dried under vacuum and calcined in air to 800 °C at a rate of 2.5 °C/min then held for 4 h and cooled to room temperature over 3 h. The calcined composite (170 mg) was then dispersed into 20 mL of deionized water and the SiO_2 was removed by etching with a

NaOH solution (1.5 mL, 2.5 M) at 70°C for 12 h. The etched microspheres were centrifuged and washed several times with deionized water and dried under vacuum to obtain the final powder.

2.2.4 Characterization

The sample morphology was characterized using transmission electron microscopy (TEM, Tecnai T12, 120 kV). The crystal phase and grain size was determined by X-ray diffraction (XRD) analysis using a Bruker D8 Advance Diffractometer with Cu Kα radiation ($\lambda = 1.5406$ Å). The nitrogen adsorption isotherm was obtained at 77 K using a Quantachrome NOVA 4200e Surface Area and Pore Size Analyzer. The surface area was calculated from the adsorption isotherm using the multi-point BET method in the pressure range of $P/P_0 = 0.05\text{-}0.25$. The average pore sizes were determined by the BJH method from the adsorption isotherm. FTIR measurements were done on a Bruker Equinox 55 FTIR.

2.2.5 Photocatalytic Activity Tests

The photocatalytic activity was tested by the degradation of Rhodamine B (RhB). Before the reaction was initiated, the catalyst was first irradiated under UV light for 30 min to remove any residual organic contaminants. Catalyst (5 mg) was added to an aqueous RhB solution (25 mL, 2.0×10^{-5} M) in a 50 mL quartz cell and the solution was stirred in the dark for 30 min to ensure adsorption of dye. The UV lamp (300 W Hg) was used with a 365 nm filter in a commercial reactor system (Xujiang XPA-7). The concentration of RhB was measured by UV-Vis spectrophotometry (HR2000CG-UV-NIR, Ocean Optics) during the reaction.

Table 1. Summary of physicochemical characterization of TiO_2 samples.

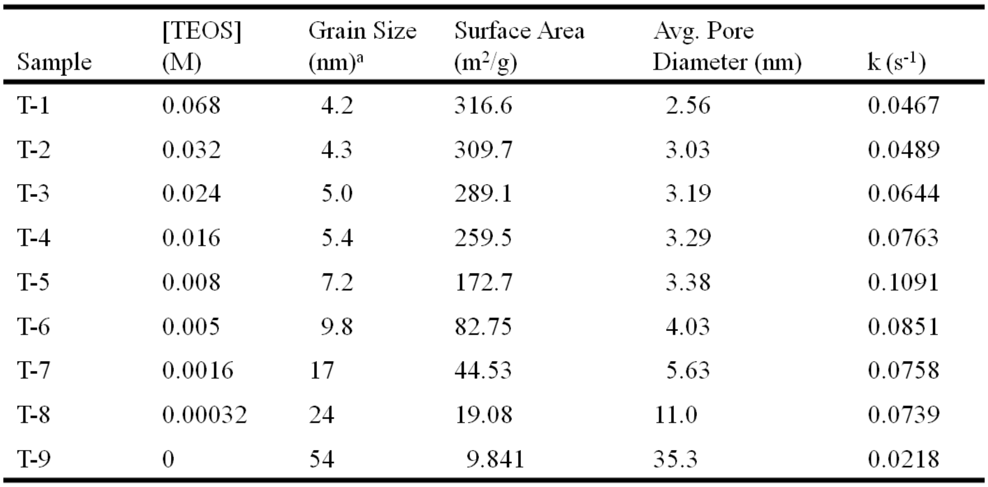

Sample	[TEOS] (M)	Grain Size (nm)[a]	Surface Area (m^2/g)	Avg. Pore Diameter (nm)	k (s^{-1})
T-1	0.068	4.2	316.6	2.56	0.0467
T-2	0.032	4.3	309.7	3.03	0.0489
T-3	0.024	5.0	289.1	3.19	0.0644
T-4	0.016	5.4	259.5	3.29	0.0763
T-5	0.008	7.2	172.7	3.38	0.1091
T-6	0.005	9.8	82.75	4.03	0.0851
T-7	0.0016	17	44.53	5.63	0.0758
T-8	0.00032	24	19.08	11.0	0.0739
T-9	0	54	9.841	35.3	0.0218

a – Determined from Scherrer Equation $D = \frac{K\lambda}{B\cos\theta}$

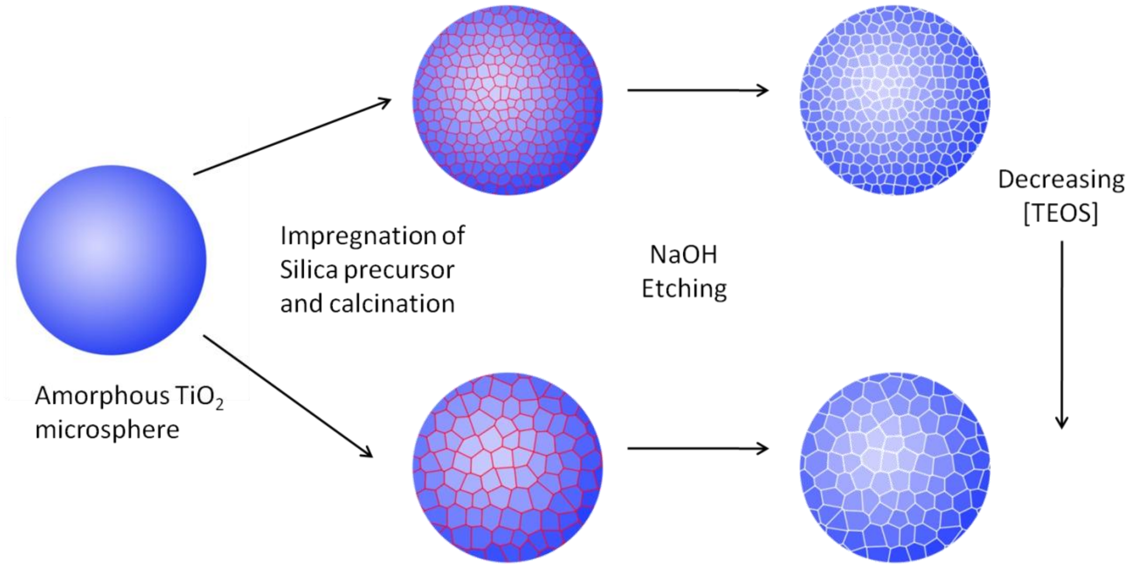

Figure 2.1 Schematic illustration of the impregnation of silica precursor into amorphous TiO$_2$ and its effect on the crystallinity of the product microspheres

2.3 Results and Discussion

The general scheme for the synthesis of SiO_2 impregnated TiO_2 microspheres is shown in Figure 2.1. The synthesis involves preparation of TiO_2 microspheres from the hydrolysis and condensation of tetrabutyl orthotitanate (TBOT), followed by impregnation with TEOS by hydrolysis in a colloidal suspension of TiO_2 microspheres. The as obtained composites are then dried and calcined to crystallize the amorphous TiO_2 network, and finally the SiO_2 within the TiO_2 microsphere is removed through chemical etching using a NaOH solution. The grain sizes within the microspheres can be tuned by simply changing the concentration of TEOS precursor added to the reaction mixture containing colloidal TiO_2 microspheres. Table 1 summarizes the sample notations as well as the pertinent data measured for each sample from which one can summarize that the grain size is inversely proportional and the surface area is directly proportional to the amount of silica impregnation. The change in crystallite size of the final products can be followed through imaging with TEM. Figure 2.2a shows sample T-1 where the microsphere produced has the smallest attainable grain size. This sample is synthesized using the highest concentration of TEOS and a procedure whereby not only is the structure impregnated with silica, but an entire shell of SiO_2 is formed around the sample. Sample T-2, where the concentration of TEOS is less than one half of that in T-1, does not form a shell however the degree of silica impregnation is great enough to nearly match the grain size and surface area of sample T-1. Further decreasing the concentration of TEOS added can then yield increased grain sizes in the as evidenced in Figure 2.2b-d.

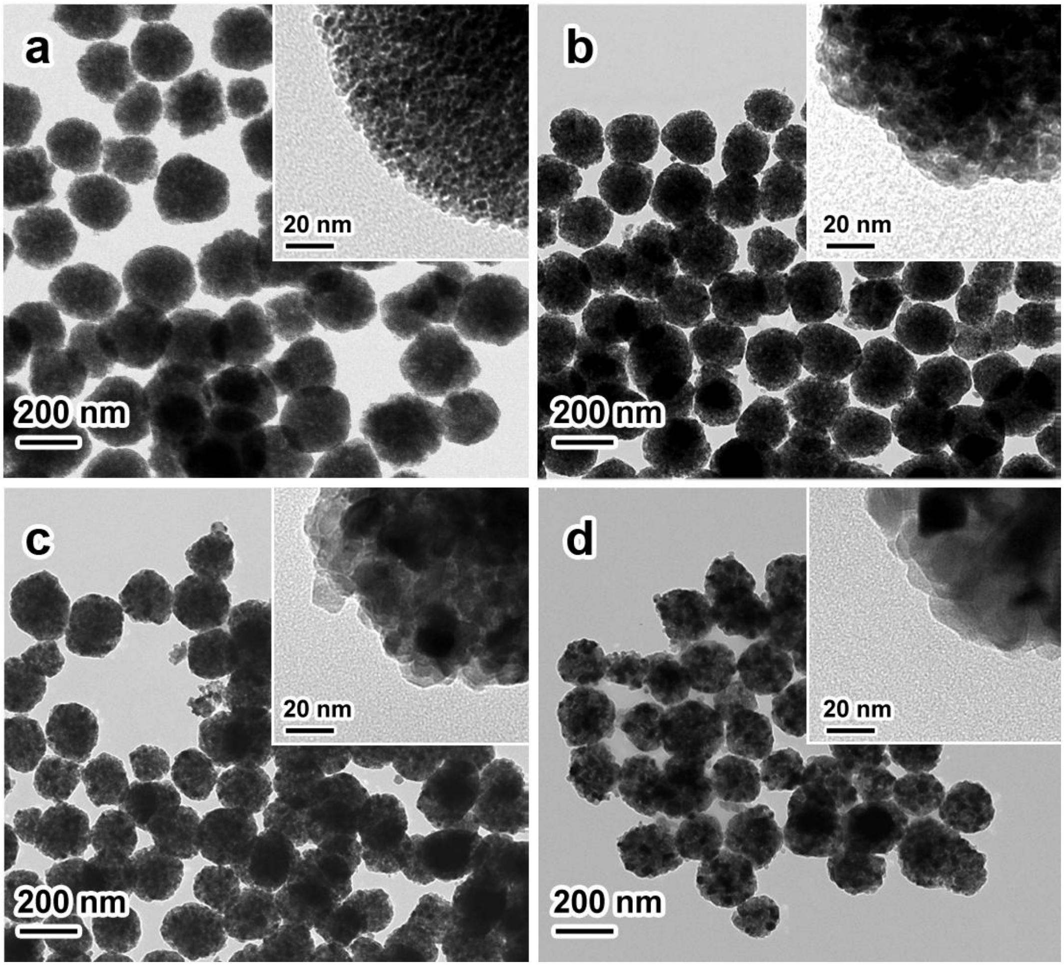

Figure 2.2 TEM images of TiO_2 microspheres with individual grains in a) T-1 and larger grains in b) T-6 c) T-7 and d) T-8

The growth of the crystal grains as well as the crystal phase of the as-prepared microspheres could be further confirmed by studying their XRD patterns. Figure 2.3a shows the XRD pattern from samples T-1 through T-9 where each peak can be indexed to pure anatase crystal structure. As the crystallinity of the samples increases, the relative intensities and sharpness of the peaks increases and the characteristic anatase (101) peak at $2\theta \approx 25°$ becomes increasingly distinct. In order to better quantify the increase in crystallinity, the Scherrer formula was used to estimate the grain sizes using the anatase (101) peak.[30] Figure 2.3b summarizes the trend of the increase in grain size as determined by XRD as a function of the TEOS concentration. We see that the highest concentrations of TEOS correspond to the smallest crystal grain sizes of approximately 4.2 nm, which corroborates the TEM images. The grain size could then be tuned within the range of 4.2 nm to 25 nm based simply on the concentration of TEOS added. The increase in grain size is attributed to the fact that since less silica precursor is present, there is not enough to form a complete coating around each grain which allows the grain to grow larger while crystallizing from the amorphous network.[21] This in turn must then yield a larger grain size in comparison to samples which have more silica present. The sample with the largest crystal grain size, T-9, refers to a sample of as-synthesized colloidal TiO_2 microspheres, without any TEOS addition. A crystal grain size of approximately 54 nm is estimated by the Scherrer equation, which gives a good representation of how large the grain sizes have grown even though this is presumed inexact because of limitations of the Scherrer formula.[31] The shape factor used is based on an estimate of roughly spherical

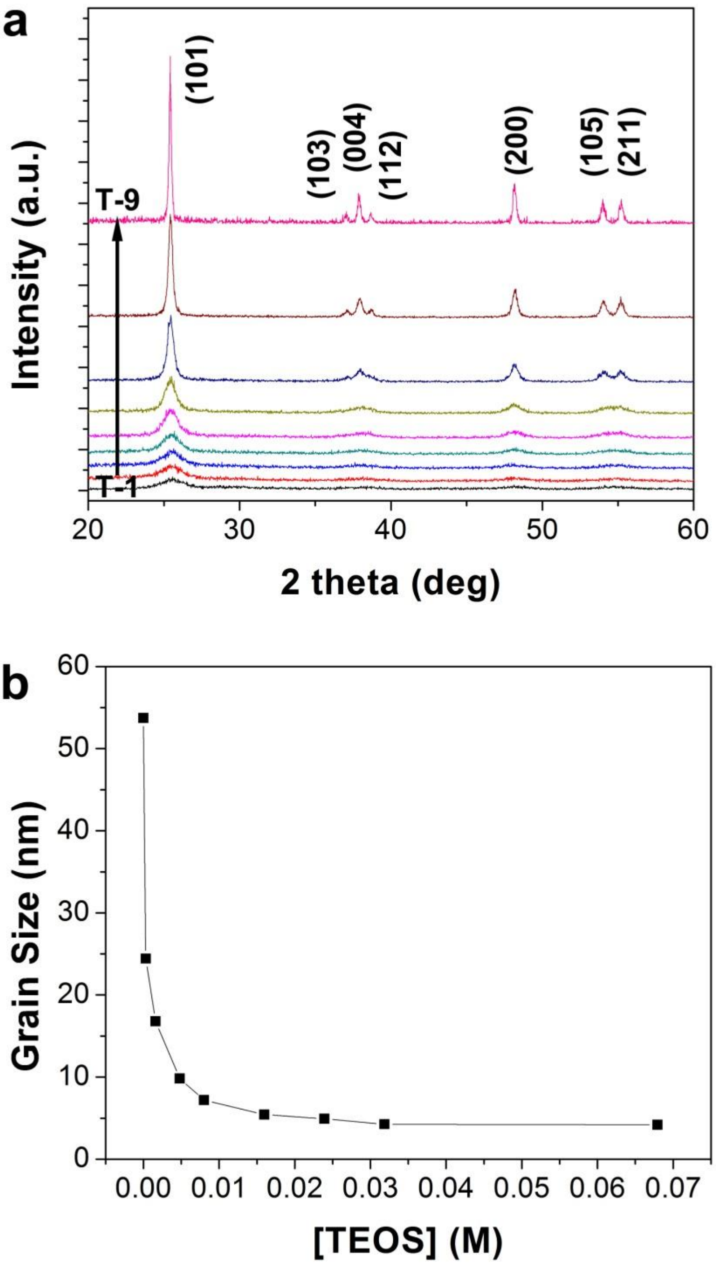

Figure 2.3 a) X-ray diffraction patterns of TiO_2 microspheres after calcination at 800°C and removal of SiO_2. The diffraction patterns become increasingly sharper as the concentration of TEOS decreases. b) Plot summarizing the effects of TEOS on the in grain size as determined by the Scherrer equation.

morphology of the crystal grains which can be used with confidence for smaller grain sizes; however the larger grain sizes within the microspheres became noticeably non-spherical.

As the crystallinity of the grains in the microspheres increases, the porosity and surface area of the samples must correspondingly be altered as well. This can be measured using nitrogen adsorption-desorption isotherms. Figure 2.4 details the changes in surface area and corresponding average pore diameter as measured against TEOS concentration. Each sample yielded a type IV isotherm although those with a higher surface area resulted in a higher total pore volume and larger total volume adsorbed. Additionally as the samples became more crystalline, the hysteresis loop closes at higher relative pressures indicating the growth of larger pores within the structure.[32] The surface area is measured by the multi-point Brunauer-Emmett-Teller (BET) method from the adsorption branch in the relative pressure range of 0.05 – 0.25. Surface areas as high as ~316 m^2 / g can be achieved with the highest concentrations of TEOS and this can be controlled to give surface areas as low as 10 m^2 / g by systematically decreasing the concentration of TEOS. Upon calcination, amorphous TiO_2 is converted to small crystallites, which stack together and produce mesoscale pores. The size of the pores can be determined using the Barrett-Joyner-Halenda (BJH) method on the adsorption branch of the isotherm. Average pore diameters as small as ~2.5 nm can be created yielding a high surface area mesoporous microsphere. The average pore diameter increases as the grain size increases because of the larger voids created between crystallites.

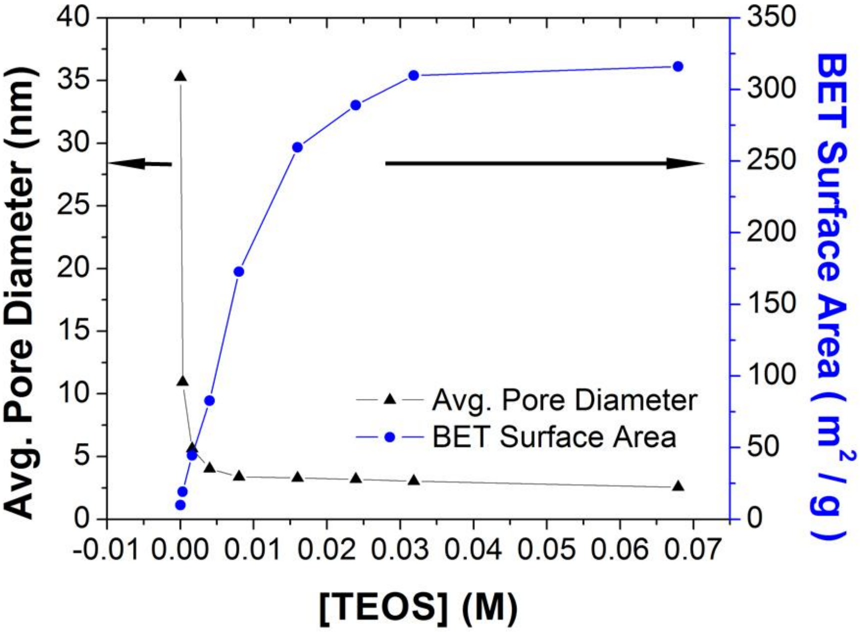

Figure 2.4 Plot summarizing the effects of TEOS on the surface area and average pore diameter as determined from multi-point BET method and BJH adsorption respectively.

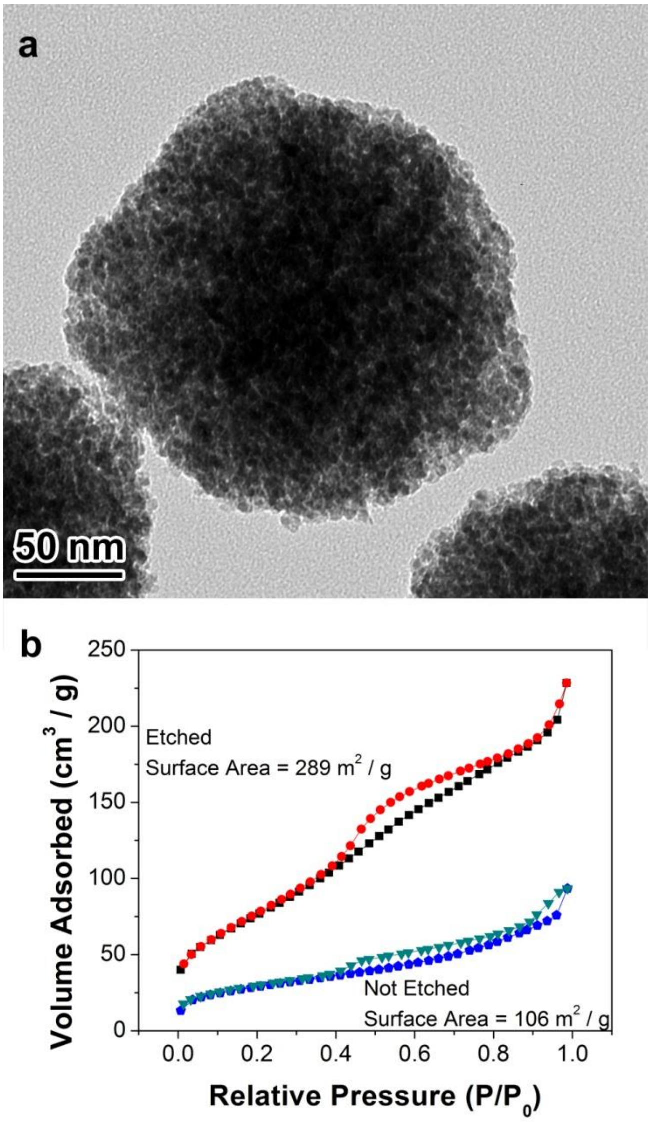

Figure 2.5 a) TEM image of TiO_2 sample T-3 after SiO_2 impregnation and calcination. Image is representative of impregnation without a full coating. b) N_2 adsorption-desorption isotherms for T-3 before and after SiO_2 removal.

The porosity of the samples also is one method to establish the penetration of SiO_2 into the TiO_2 microspheres. Sample T-3 was used to show the difference in surface area and by extension the penetration of silica before and after etching. The sample was synthesized with a TEOS concentration of 0.024 M which would not form a coating over the entire surface of the microsphere, but rather only penetrate into the microsphere as shown in Figure 2.5a. The BET surface area of the sample prior to etching was determined to be 106 m^2 / g while the surface area after etching was 289 m^2 / g (Figure 2.5b). The surface area before etching corresponds to the penetration of silica within the structure which will decrease the total surface area because of the loss of porosity. Upon removal of the silica on the TiO_2 grains, there is an increase in surface area as the structure becomes more porous. The presence and removal of silica can also be determined by FTIR which is shown in Figure 2.6. The etched sample shows only the characteristic Ti-O-Ti stretching vibration at 400-850 cm^{-1} whereas the sample which was not etched shows the Si-O-Si bending mode at ~460 cm^{-1}, the Si-O-Si asymmetric stretch at ~1080 cm^{-1} and ~1220 cm^{-1} (shoulder) and the Si-O-Ti band at ~970 cm^{-1}.[33,34]

The photocatalytic activity of the TiO_2 microspheres was tested in order to determine the optimal parameters of size of the crystallites and the surface area. The photocatalysis was tested using the model system of the degradation of the organic dye Rhodamine B (RhB) under UV irradiation. Figure 2.7a shows the rate of degradation as monitored by the decrease in absorption of the characteristic RhB peak at 553 nm versus time of selected photocatalysts. Prior to the degradation of RhB the

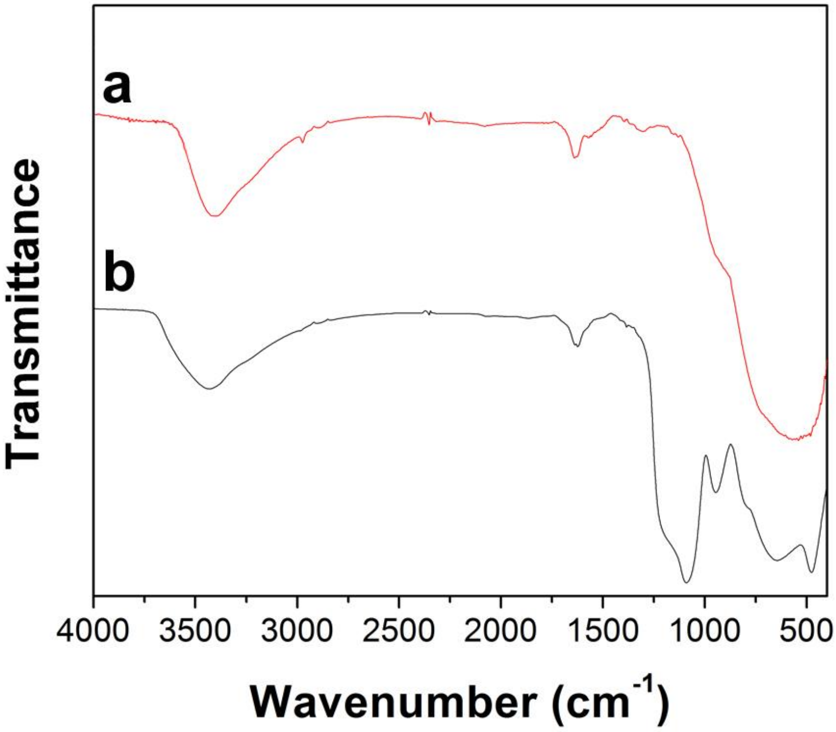

Figure 2.6 FTIR spectra of a) T-3 after etching and b) T-3 before etching showing the disappearance of characteristic Si-O-Si IR bands after etching.

photocatalysts were irradiated with UV light for 30 min to remove any organic contaminants. The dye solution containing the catalyst was first stirred under dark conditions for 30 min to ensure adsorption of the dye onto the catalyst. The samples were then irradiated under UV light with a 366 nm filter. The degradation of the dye alone under irradiation was ~6% after irradiation for 60 min whereas all the catalysts removed between 93-100% of the dye in the same period of time. The adsorption capacity of the catalysts ranges between nearly 15% for the most porous catalyst to 8% for the least porous catalyst. As shown in Figure 2.7a, sample T-1 shows a markedly lower activity due to its smaller grain size. Sample T-5 displayed the greatest activity and sample T-6 began to show a slower rate of degradation. Sample T-9 was not tested because the sample was not readily dispersible in water and upon standing for 10 min would settle out of solution.

In order to compare the reaction kinetics, we assume the reaction followed first order kinetics. Figure 2.7b shows the linear relationships when plotting ln (C/C_0) versus reaction time while under irradiation. All of the plots match first order reaction kinetics well with R^2 values all greater than 0.995. This relation allows us to determine the apparent rate constant (k) from the equation $\ln(C/C_0) = -kt$. As expected from the data in Figure 2.7b, the rate constant for degradation increases from T-1 to T-5, reaches a maximum and begins to decrease after this point. This indicates that the highest photocatalytic activity was reached by sample T-5 where $k = 0.109\ s^{-1}$. This activity should be attributed to the increase in crystal grain size while still maintaining a high surface area. Figure 2.8 summarizes the effects of the concentration of TEOS,

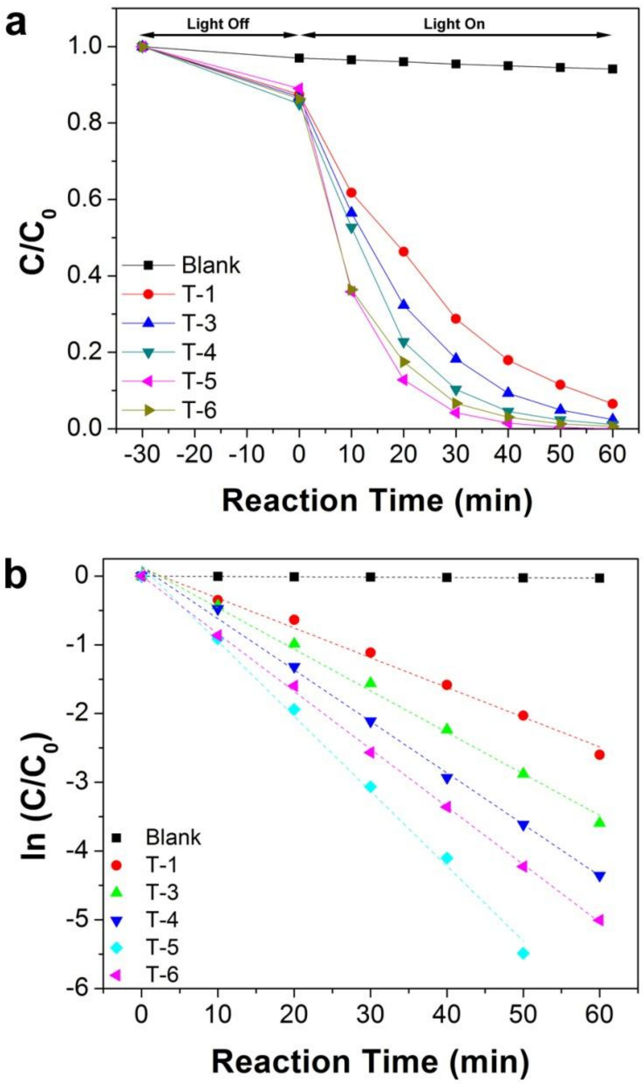

Figure 2.7 a) Degradation of RhB under UV-irradiation with a 366 nm filter b) Apparent reaction rate constant vs UV irradiation time. Some samples are omitted for clarity.

the grain size and the surface area against the apparent rate constant. Each plot displays a noticeable peak where the activity reaches a maximum which corresponds to sample T-5. The decrease in activity after sample T-5 is assumed to occur because of the large decrease in surface area. The general trend regarding the crystallinity should be that as the grain size increases, the activity increases; however after the peak corresponding to T-5 the surface area drops precipitously causing a decrease in activity due to the decrease in the number of redox sites available. When k is plotted as a function of grain size, as in Figure 2.8b, the drop in activity is noticeable though not as much so as when k is plotted against surface area as in Figure 2.8c. This data yields an optimal photocatalyst with a grain size of approximately 7.2 nm and a surface area of 173 m^2 / g. The cause for the increase in photocatalytic activity is further supported by the UV-Vis diffuse reflectance spectra shown in Figure 2.9. The spectra of the samples appear very similar regardless of the change in TEOS concentration, indicating that a bandgap shift is not responsible for the difference in photocatalytic activities.

2.4 Conclusion

In summary, we have demonstrated the preparation of a mesoporous TiO_2 microsphere structure with controllable grain size and surface area. The method involves the hydrolysis of a specific concentration of a silica precursor in a solution of colloidal TiO_2, followed by calcination of the composite to crystallize the amorphous TiO_2 structure and removal of the silica through chemical etching. Tuning the concentration of the silica added controls the size of the crystal grains which grow in each TiO_2 microsphere. As the grain sizes grow, the surface area correspondingly decreases. This study determined an optimum balance between grain size and surface area which yielded the highest photocatalytic activity as determined by the degradation of Rhodamine B under UV irradiation. Such a systematic investigation may pave the way for rational design in the future for more efficient TiO_2-based photocatalysts, for example, by combining the crystallinity control with non-metal doping and plasmonic metal nanoparticle decoration.

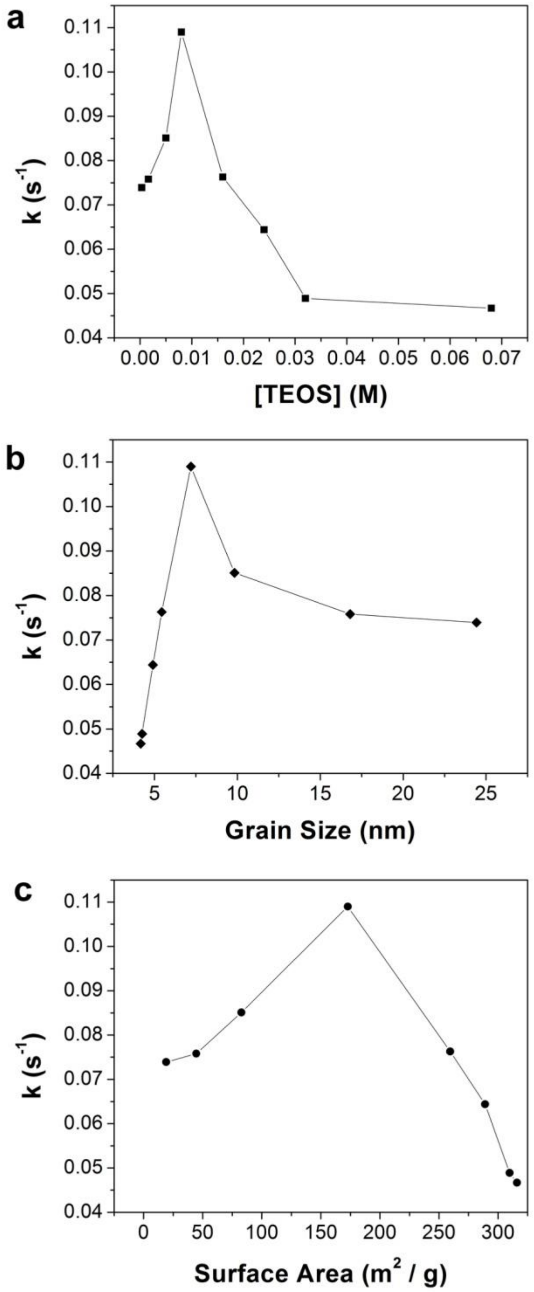

Figure 2.8 Plots summarizing the effect of a) TEOS concentration b) grain size and c) surface area on the apparent rate constant

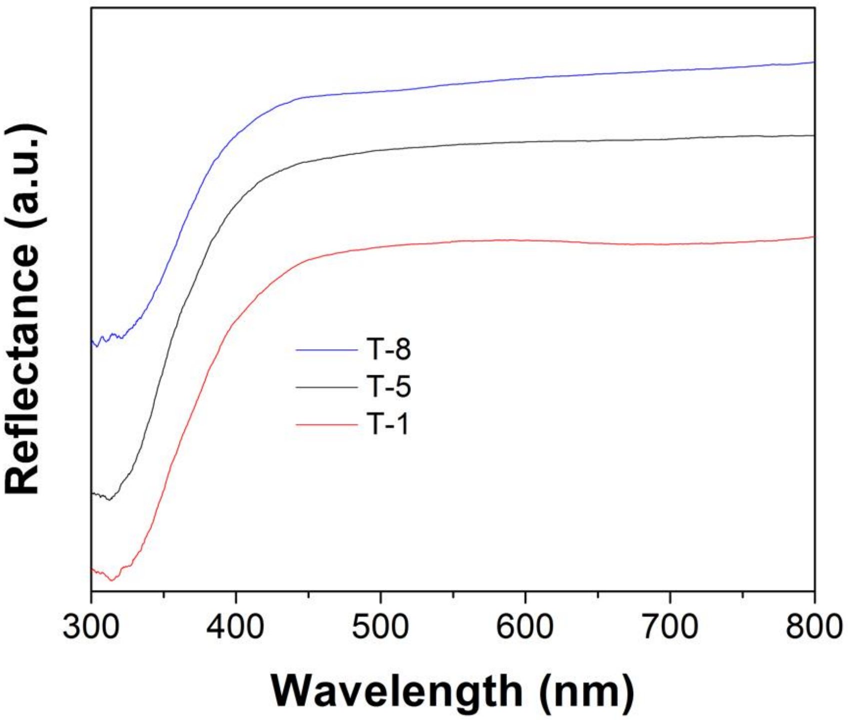

Figure 2.9 UV-Vis diffuse reflectance spectra of samples T-1, T-5 and T-8 indicating no change in absorption of light to account for change in photocatalytic activity.

2.5 References

(1) O'Regan, B.; Gratzel, M. *Nature* **1991**, *353*, 737.

(2) Chen, X.; Mao, S. S. *Chem. Rev.* **2007**, *107*, 2891.

(3) Fujishima, A.; Honda, K. *Nature* **1972**, *238*, 37.

(4) Bowker, M. *Green Chem.* **2011**, *13*, 2235.

(5) Zuo, F.; Wang, L.; Wu, T.; Zhang, Z.; Borchardt, D.; Feng, P. *J. Am. Chem. Soc.* **2010**, *132*, 11856.

(6) Ye, M.; Zhang, Q.; Hu, Y.; Ge, J.; Lu, Z.; He, L.; Chen, Z.; Yin, Y. *Chem. Eur. J.* **2010**, *16*, 6243.

(7) Lee, I.; Joo, J. B.; Yin, Y.; Zaera, F. *Angew. Chem. Int. Ed.* **2011**, *50*, 10208.

(8) Matsuda, S.; Kato, A. *Appl. Catal.* **1983**, *8*, 149.

(9) Zhang, Q.; Lima, D. Q.; Lee, I.; Zaera, F.; Chi, M.; Yin, Y. *Angew. Chem.* **2011**, *123*, 7226.

(10) Zhang, Q.; Joo, J.-B.; Lu, Z.; Dahl, M.; Oliveira, D.; Ye, M.; Yin, Y. *Nano Res.* **2011**, *4*, 103.

(11) Hanaor, D.; Sorrell, C. *J. Mater. Sci.* **2011**, *46*, 855.

(12) Fox, M. A.; Dulay, M. T. *Chem. Rev.* **1993**, *93*, 341.

(13) Sclafani, A.; Herrmann, J. M. *J. Phys. Chem.* **1996**, *100*, 13655.

(14) Mott, N. F.; Allgaier, R. S. *Phys. Status Solidi B* **1967**, *21*, 343.

(15) Barzykin, A. V.; Tachiya, M. *J. Phys. Chem. B* **2002**, *106*, 4356.

(16) Zhang, Z.; Wang, C.-C.; Zakaria, R.; Ying, J. Y. *J. Phys. Chem. B* **1998**, *102*, 10871.

(17) Zhang, H.; Finnegan, M.; Banfield, J. F. *Nano Lett.* **2000**, *1*, 81.

(18) Ermokhina, N. I.; Nevinskiy, V. A.; Manorik, P. A.; Ilyin, V. G.; Shcherbatyuk, N. N.; Klymchyuk, D. O.; Puziy, A. M. *Mater. Lett.* **2012**, *75*, 68.

(19) Lu, Z.; Ye, M.; Li, N.; Zhong, W.; Yin, Y. *Angew. Chem.* **2010**, *122*, 1906.

(20) Reidy, D. J.; Holmes, J. D.; Morris, M. A. *J. Eur. Ceram. Soc.* **2006**, *26*, 1527.

(21) Okada, K.; Yamamoto, N.; Kameshima, Y.; Yasumori, A.; MacKenzie, K. J. D. *J. Am. Ceram. Soc.* **2001**, *84*, 1591.

(22) Zhang, Z.; Zuo, F.; Feng, P. *J. Mater. Chem.* **2010**, *20*, 2206.

(23) Aguado, J.; van Grieken, R.; López-Muñoz, M.-J.; Marugán, J. *Appl. Catal., A* **2006**, *312*, 202.

(24) He, C.; Tian, B.; Zhang, J. *J. Colloid Interf. Sci.* **2010**, *344*, 382.

(25) Tobaldi, D. M.; Tucci, A.; Škapin, A. S.; Esposito, L. *J. Eur. Ceram. Soc.* **2010**, *30*, 2481.

(26) Joo, J. B.; Zhang, Q.; Lee, I.; Dahl, M.; Zaera, F.; Yin, Y. *Adv. Funct. Mater.* **2012**, *22*, 166.

(27) Joo, J. B.; Zhang, Q.; Dahl, M.; Lee, I.; Goebl, J.; Zaera, F.; Yin, Y. *Energy Environ. Sci.* **2012**, *5*, 6321.

(28) Hu, Y.; Ge, J.; Sun, Y.; Zhang, T.; Yin, Y. *Nano Lett.* **2007**, *7*, 1832.

(29) Jean, J. H.; Ring, T. A. *Colloids Surf.* **1988**, *29*, 273.

(30) Zhong, J.; Chen, F.; Zhang, J. *J. Phys. Chem. C* **2009**, *114*, 933.

(31) Patterson, A. L. *Phys. Rev.* **1939**, *56*, 978.

(32) Kumar, K.-N. P.; Kumar, J.; Keizer, K. *J. Am. Ceram. Soc.* **1994**, *77*, 1396.

(33) Bertoluzza, A.; Fagnano, C.; Antonietta Morelli, M.; Gottardi, V.; Guglielmi, M. *J. Non-Cryst. Solids* **1982**, *48*, 117.

(34) Kang, C.; Jing, L.; Guo, T.; Cui, H.; Zhou, J.; Fu, H. *J. Phys. Chem. C* **2008**, *113*, 1006.

Chapter 3

Titanium Alkoxide-Ethylene Glycol Mixed Precursors for Coating TiO_2 on Nanoparticles

3.1 Introduction

The utilization of titanium dioxide for applications in photocatalysis, solar cells, sensors, etc. has been widely studied in recent years.[1-4] However, due to the wide band gap of TiO_2, 3.2 eV for anatase and 3.0 eV for rutile,[5] much work has been done in order to expand the activity to the visible region. One method under current investigation is the addition of metal nanoparticles, such as Au and Ag, in order to utilize their inherent surface plasmon absorption and to improve the separation of photogenerated charge carriers from TiO_2.[6,7] Many methods for attachment have been studied, however the sintering of nanoparticles at higher temperatures and the loss of activity under reaction conditions has been of concern. One method for avoiding this activity loss is embedding the particles within the TiO_2 materials.[7,8] This method for utilization is promising, however the lack of porosity in the metal oxide shell can greatly decrease the accessibility of reactants to the metal nanoparticle within.[9] In order to better utilize the properties of such metal-metal oxide composites, core-shell systems have been proposed. Core@shell TiO_2 structures and composites have seen significant research in recent times. Templates such as polystyrene,[10,11] silica,[12-15] iron oxide,[16,17] and metal nanoparticles[18-24] have all been utilized. These templates have allowed for the placement of the metal nanoparticles within a porous TiO_2 layer for improved accessibility, stability under thermal treatment, and recyclability.[13,25]

Unfortunately a wide variety of parameters are needed in order to coat this range of materials. Some methods have been established for extending uniform coatings to larger colloids,[17,26] however, the uniform coating of TiO_2 onto small metal nanoparticles, i.e. <50 nm diameter, has been difficult to achieve without either significant free TiO_2 particle formation, [27,28] or with a well controllable TiO_2 shell thickness. [29] Recent progress has been made in the coating of TiO_2 onto both silver nanoplates[30] and gold nanorods,[31,32] however a comprehensive system is still desirable.

In order to establish a coating method for both small materials and large materials alike, an ethylene glycol-titanium n-butoxide mixed precursor solution was established. The mixture of titanium alkoxides with ethylene glycol to produce a chelated complex has been shown previously,[33,34] further this particular precursor has been studied for its ability to form highly spherical titania colloids in an acetone solution.[35-38] Complexation of Ti^{4+} with ethylene glycol yields a titanium glycolate species which is much more stable than the parent titanium alkoxide precursor. This precursor can then undergo a more controlled reaction, catalyzed by the acetone, to produce uniform titanium glycolate microspheres. The role of the acetone as catalyst has been recently uncovered, and it is of note that the purity of the acetone, with respect to water content, is critical to the synthesis of uniform microspheres.[37] Once the titanium glycolate products have been formed, crystallization to TiO_2 can be done simply through high temperature calcination.

This study will provide a simple route for depositing a titanium glycolate coating on several materials including gold and silver spherical nanoparticles (~15-20nm diameter), gold nanorods, silver nanoplates, silica microspheres, and resorcinol-formaldehyde polymer microspheres. The effect that this coating has on the plasmon absorption of each type of metal nanoparticle will be detailed. Further, the crystallization of the as-coated titanium glycolate will be studied through refluxing in water as well as by high temperature calcination. Additionally, the utilization of hollow TiO_2 shells made by coating a silica template with titanium glycolate, calcination, and etching will be demonstrated by the degradation of Rhodamine B dye under UV irradiation. Finally, in order to improve photocatalysis of the TiO_2 shells and to extend it to the visible light reagion, the hollow TiO_2 shells are doped with additional metal ions and processed under similar conditions to compare to the undoped samples.

3.2 Experimental

3.2.1 Titanium Glycolate Preparation

Varying volumes of titanium n-butoxide (TBOT, 97%) was added to a vial containing ethylene glycol (EG, 99+%) to a total volume of 20 mL. For example, to produce a 2.5 vol. % precursor solution, 0.500 mL TBOT was mixed with 19.5 mL ethylene glycol. The resulting solution was then capped and stirred for at least 12 h before use.

3.2.2 Mixed Metal Titanium Glycolate Preparation for Doped Coatings

To produce mixed metal glycolate, the selected metal was first dissolved in ethylene glycol, then diluted further with ethylene glycol, followed by addition of titanium n-butoxide. For example to produce a 1 mol % Ni^{2+} precursor, 42.7 mg of $Ni(NO_3)_2 \bullet 6H_2O$ was dissolved in 10 mL ethylene glycol. The Ni^{2+}-ethylene glycol solution was then diluted with additional ethylene glycol to 19.55 mL. To this solution, 0.495 mL TBOT was added and the resulting mixture was stirred for at least 12 h before use.

3.2.3 Nanoparticle and Microsphere Synthesis

Au nanoparticles were synthesized using the Turkevich method[39]. Briefly 19 μL of $HAuCl_4 \cdot 3H_2O$ (1 g mL^{-1}) was added to 95 mL of water and the solution was heated to reflux. Next trisodium citrate dihydrate (TSC, 99%, 0.034 M, 5 mL) was quickly added to the hot solution. The refluxing was continued for 20 min then the solution was cooled to room temperature and stored. Ag nanoparticles were prepared from reported methods[40]. In a typical synthesis TSC (13.6 mM, 5 mL) and tannic acid (1.8 μM, 5 mL) were mixed and heated to 60 °C. Separately a solution of $AgNO_3$ (0.74 mM, 40 mL) was also heated to 60 °C, and upon reaching temperature, the TSC/tannic acid solution was added to it. The mixture was stirred for 3 min, then refluxed for 20 min before cooling and storing in dark conditions at 4 °C. Au nanorods were prepared according to the method from Ye et al. with no modifications[41]. After synthesis, the Au nanorods were concentrated to one-tenth of their original volume and redispersed in water. Ag nanoplates were prepared via a standard citrate reduction without use of polymer surfactant[42]. In a typical synthesis TSC (0.075 M, 2 mL) was added to 100 mL of water. To this solution $AgNO_3$ (0.05 M, 0.200 mL) and H_2O_2 (30 wt. %, 0.120 mL) was added with vigorous stirring. Then fresh, iced $NaBH_4$ (99%, 0.10 M, 0.200 mL) was added and the reaction was continuously stirred for 30 min, then stored in the dark for future use. SiO_2 microspheres were synthesized using a modified Stöber process. Tetraethyl orthosilicate (TEOS, 99%, 5.16 mL) was mixed with de-ionized water (25.8 mL), ethanol (138 mL) and an aqueous solution of ammonia (26%, 3.72 mL). After stirring for 4 h at room temperature, the colloidal silica particles were separated by centrifugation and washed three times with ethanol, then re-dispersed in 30 mL of ethanol under sonication. Resorcinol-formaldehyde (RF) polymer spheres were made similar to reported procedures[43,44]. Water (38 mL), ethanol (16 mL) and aqueous ammonia (28%, 0.200 mL) were mixed for 20 min. To this solution resorcinol (99%, 0.91 M, 2 mL) was added followed by stirring for a few minutes, then a formaldehyde solution (37 wt. %, 0.280 mL) was added, followed by stirring for 12 h. This solution was then refluxed for 3 h, centrifuged, washed with water three times and stored in 10 mL of water.

3.2.4 Titanium Glycolate Coating on SiO_2

To coat SiO_2 microspheres, 3 mL of the above colloid was centrifuged, washed once with acetone, then dispersed in 25 mL of acetone. This dispersion was added to a solution of 50 mL acetone and 0.3 mL water with stirring. To this solution the titanium glycolate precursor (2.5 vol. % TBOT in EG, 3.75 mL) was slowly injected over the course of 35 min. The solution was then stirred for 30 min, collected by centrifugation, washed once with acetone and twice with ethanol, then stored in ethanol. To produce shells of a thicker coating, this process can be repeated after washing once with acetone. Doped titanium glycolate coatings were done utilizing the same procedure as the non-doped materials. Each of the samples was coated four times in order to obtain thicker hollow doped TiO_2 shells as the final product.

3.2.5 Titanium Glycolate Coating on RF Polymer Spheres

To coat RF polymer spheres, 2 mL of the above RF suspension were centrifuged, then washed once with acetone, and dispersed in 25 mL of acetone. To this solution water (0.100 mL) was added with stirring, and the titanium glycolate precursor (1.25 vol. % TBOT in EG, 1.25 mL) was slowly injected over the course of 35 min. The solution was then stirred for 30 min, collected by centrifugation, washed once with acetone and twice with ethanol, then stored in ethanol. To produce thicker coatings, this process can be repeated after washing once with acetone.

3.2.6 Titanium Glycolate Coating on Nanoparticles

Nanoparticles of gold and silver, as well as silver nanoplates were all coated using a similar method. First 10 mL of the aqueous nanoparticle colloid was concentrated to a volume of 0.100 mL in water. Next a solution of acetone (25 mL) and titanium glycolate precursor (0.25 vol. % TBOT in EG, 0.020 mL) was prepared. To this solution the nanoparticles were added followed by injection of more titanium glycolate precursor (0.25 vol. % TBOT in EG, 0.180 mL) over the course of 30 min. The solution was then stirred for 30 min, collected by centrifugation, washed once with acetone and twice with ethanol, then stored in ethanol. To coat gold nanorods, 1 mL of the products of the above synthesis was concentrated to a volume of 0.050 mL. Then the coating procedure follows that of the other nanoparticle systems.

3.2.7 Crystallization of the Titanium Glycolate Shell

To crystallize the shell via refluxing, the sample is first centrifuged and dispersed into an aqueous sodium fluoride solution (10 mM, 25 mL), then refluxed for 1h. To crystallize via calcination, the sample is heated to the desired temperature at a rate of 2.5 °C min^{-1} then held for 4h.

3.2.8 Characterization

The morphology of each sample was observed by transmission electron microscopy (TEM, Tecnai T12, 120 kV). Surface plasmon resonance absorption spectra were measured by UV-Vis spectrophotometry (HR2000CG-UV-NIR, Ocean Optics). The Raman spectra were measured on a Horiba LabRAM HR confocal imaging system (λ_{ex} = 532 nm). The crystalline structures were determined by X-ray diffraction (XRD) analyses using Bruker D8 Advance Diffractometer with Cu Kα radiation ($\lambda = 1.5406$ Å). The nitrogen adsorption isotherms were obtained at 77 K using a Quantachrome NOVA 4200e Surface Area and Pore Size Analyzer. The surface area was calculated from the adsorption isotherm using the multi-point BET method in the pressure range of $P/P_0 = 0.05–0.25$.

3.2.9 Photocatlytic Measurments

The catalyst to be tested (5 mg) was dispersed in an aqueous Rhodamine B solution (25 mL, 2.0×10^{-5} M) in a 50 mL quartz cell which was then stirred in the dark for 30 min to ensure adsorption of the dye. Irradiation was done using a UV lamp (300 W Hg) with a 365 nm filter in a commercial reactor system (Xujiang XPA-7). To test the visible light degradation of RhB, the catalyst to be tested (5 mg) was dispersed in 25 mL of an aqueous RhB solution (1.0×10^{-5} M) then placed in a similar setup to the previous setup. The light source was a 500 W tungsten lamp with a 420 nm cutoff filter in the same reactor setup. In both the UV and visible cases, the concentration of RhB was determined by measuring the absorbance on a UV-Vis spectrophotometer (HR2000CG-UV-NIR, Ocean Optics).

3.3 Results and Discussion

3.3.1 Titanium Glycolate Coating on Nanoparticles and Microspheres

A generalized procedure for the coating of titanium glycolate onto nanoparticles and microspheres has been developed by utilizing a precursor consisting of titanium n-butoxide in ethylene glycol. The procedure consists of injecting titanium-glycolate precursor solutions of different concentrations into a colloidal dispersion of the template particles in acetone, with a minor amount of water present. TEM images of gold nanoparticles made by a standard citrate reduction are shown in

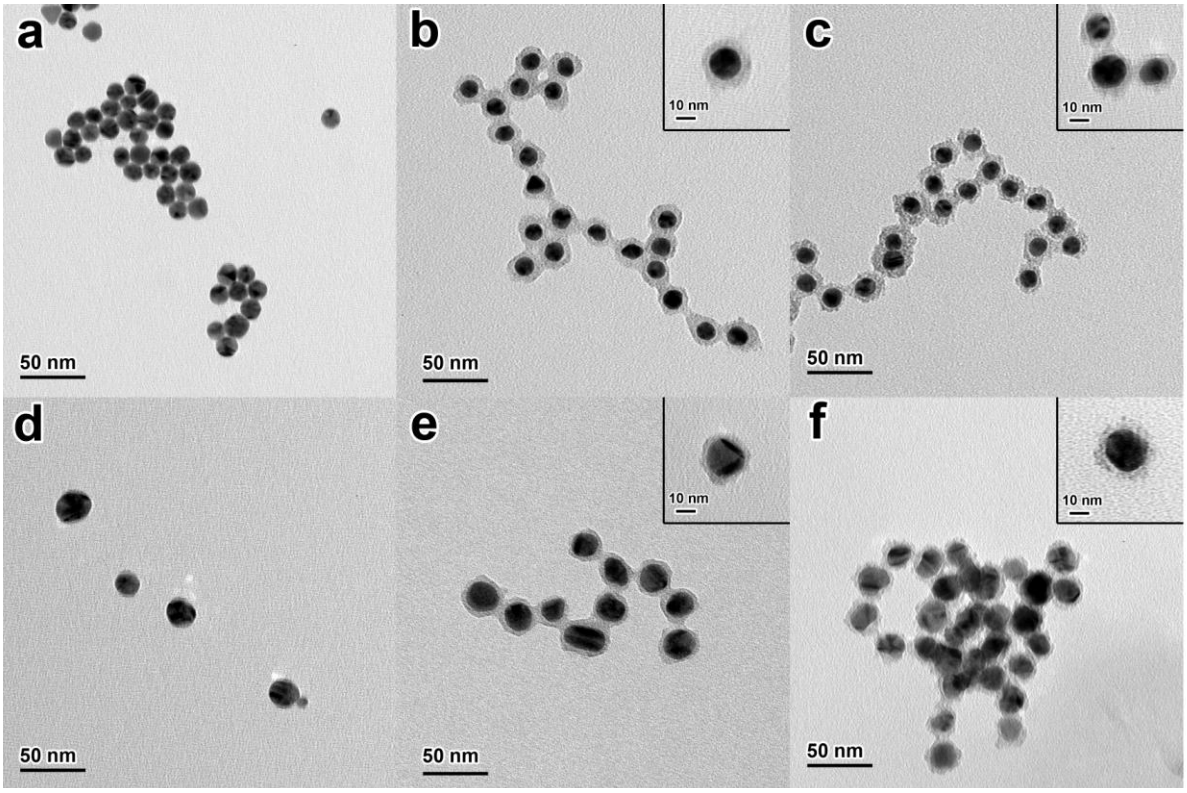

Figure 3.1 (a-c) TEM images of gold nanoparticles (a) before coating, (b) after coating with titanium glycolate, and (c) after refluxing. (d-f) TEM images of silver nanoparticles (d) before coating, (e) after coating with titanium glycolate, and (f) after refluxing.

Figure 3.1a and silver nanoparticles made by reduction using a mixture of trisodium citrate and tannic acid are shown in 3.1d. In order to coat titanium glycolate onto gold and silver nanoparticles, a 0.25 vol. % solution of titanium n-butoxide in ethylene glycol was prepared and used. As shown in Figure 3.1, the coating on nanoparticles of both gold (3.1b) and silver (3.1e) has a thickness of approximately 5-8nm. The as-coated particles are well-dispersed in solution, however upon preparation for TEM, some of the coated particles agglomerate together. In order to convert the amorphous coating surrounding the nanoparticles into a crystalline shell, the particles were refluxed in an aqueous solution. Wang et al. demonstrated that amorphous titania materials can be converted to crystalline TiO_2 by aging in water.[45] This method has additionally been demonstrated to induce the hydrolysis of titanium glycolate microspheres in order to form crystalline TiO_2 as well.[37,46] This method of crystallization is very mild and forms small TiO_2 primary particles of predominantly anatase phase with some brookite phase. The brookite phase can be prevented by the addition of a small amount of an inorganic fluoride source such as NaF or NH_4F.[45] The TEM images of titanium glycolate coated gold and silver particles after refluxing in water are shown in Figure 3.1c and f, respectively. The images show a marked change in appearance from the smooth amorphous coating to a more granular state, indicating a transition to a more crystalline nature where the shell is made up of small primary TiO_2 particles. It must be noted that after refluxing, these particles do show a more pronounced tendency towards aggregation. Figure 3.2 shows the UV-VIS absorption spectra of the gold and silver nanoparticles. Figure 3.2a shows spectra of bare gold nanoparticles, coated gold nanoparticles, and coated particles after refluxing. The bare, uncoated gold nanoparticles show a peak near 520 nm, typical of citrate stabilized gold surface plasmon absorption. This peak is then redshifted by approximately 10 nm upon coating by titanium glycolate. It should be noted here that the overall profile of the peak changes little, indicating that the aggregation shown by the TEM results in Figure 3.1 does not appear in solution. After refluxing, the titanium glycolate coated gold nanoparticles show minimal change in the absorption peak position, however a significant widening of the peak can be attributed to aggregation of the particles. Figure 3.2b shows the UV-VIS absorption spectra of bare silver nanoparticles, coated silver nanoparticles, and coated particles after refluxing. The bare particles show a peak near 404 nm, typical of silver nanoparticles of the size. Much like with the coating on gold nanoparticles, there is a redshift in the surface plasmon absorption peak, however it is much more pronounced in the case of silver as the peak redshifts ~35 nm to 440 nm. Further the coated particles which appear aggregated by the TEM results do not appear as such in solution as determined by the lack of peak broadening in the spectra. The coated particles after refluxing show both aggregation by the broadening of the peak as well as another significant redshift of ~45nm to 485 nm.

In order to better demonstrate the utility of this coating methodology, it is necessary to coat titanium glycolate onto particles of different sizes. Other methods frequently reported are optimized for and limited to a narrow range of particle sizes whereas this method can be used to coat a wide range of sizes. TEM images demonstrating the extension of this coating method to larger nanoparticles is shown in Figure 3.3. Figure 3.3a and 3.3b shows TEM images of silver nanoplates of ~40-60 nm in diameter before and after coating, respectively. The coating on the silver

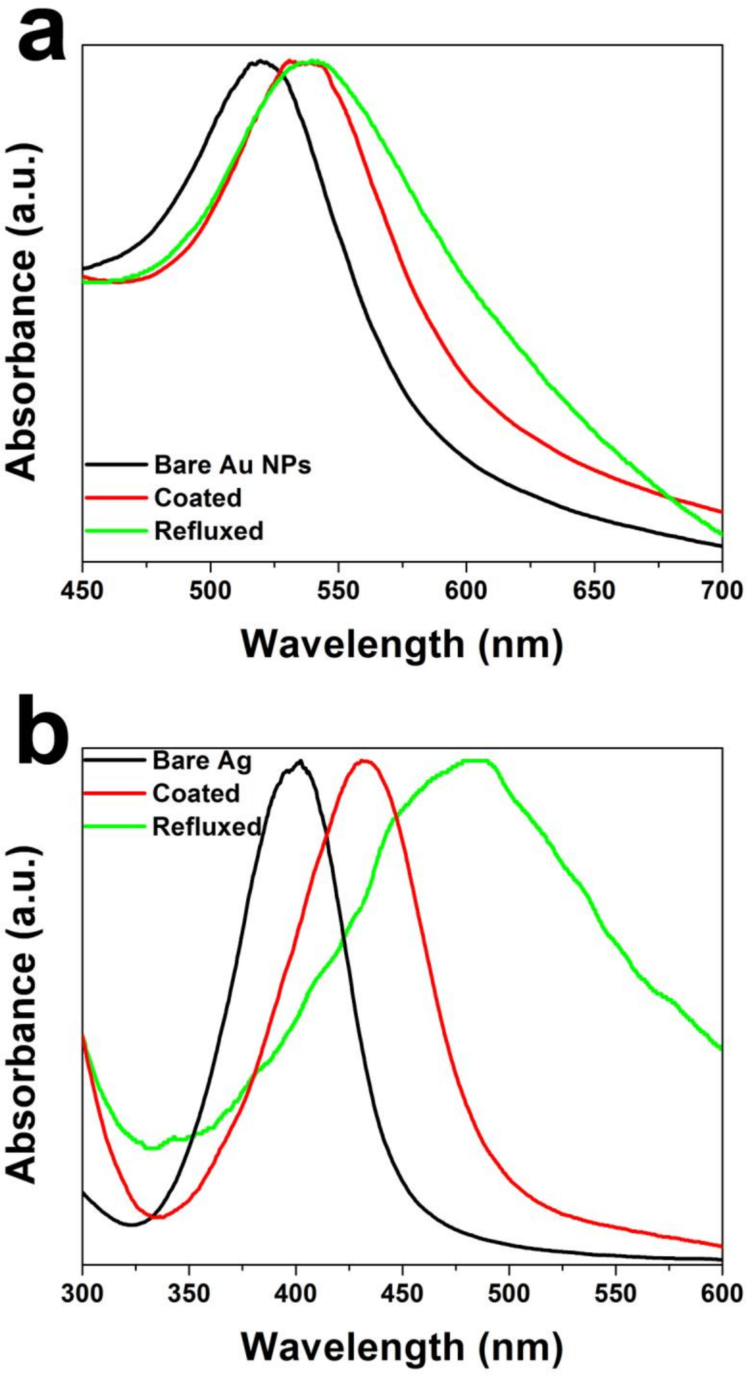

Figure 3.2 UV-Vis absorption spectra of (a) gold nanoparticles and (b) silver nanoparticles before coating with titanium glycolate, after coating, and after refluxing.

nanoplates is less uniform than the coating on the spherical nanoparticles, showing thicknesses between 4-10 nm which may be partially due to the anisotropy of the nanoplates. Figure 3.3c and 3.3d show TEM images of gold nanorods before (3.3c) and after (3.3d) coating with titanium glycolate. The dimensions of the gold nanorods are approximately 60 nm in length and 20 nm in width, with some polydispersity. The coating is approximately 7-10 nm in thickness, and it creates a more uniform coating on individual particles. As with the case of the spherical nanoparticles, both the silver nanoplates and the gold nanorods showed a redshift in the surface plasmon absorption as shown in Figure 3.4. The bare silver nanoplates show a strong peak at 830 nm which is assigned to the in-plane dipole plasmon resonance. After coating, this peak is redshifted considerably to 907 nm. The gold nanorods show peaks at 514 and 710 nm which are assigned to the transverse and longitudinal plasmon resonance of the rod, respectively. The transverse peak is only redshifted slightly, by ~10 nm whereas the longitudinal peak displays a more pronounced redshift to 752 nm. These two examples depict the ease of coating metal nanoparticles of larger size and of different morphologies without significantly changing the procedure.

The thickness of the titanium glycolate coating can also be tuned by either changing the concentration of templates or by using subsequent coatings. Figure 3.5a-d shows TEM images indicating the difference in the thickness of the titanium glycolate layer on gold nanorods. By changing the amount of gold nanorod templates added into the solution, the thickness of the resulting coating can be changed. Figure 3.5b shows a thin, non-uniform coating of approximately 1-2 nm which is obtained when the amount of gold nanorods added is at its largest. This thickness can be increased by decreasing the amount of gold nanorods added as shown in Figure 3.5c

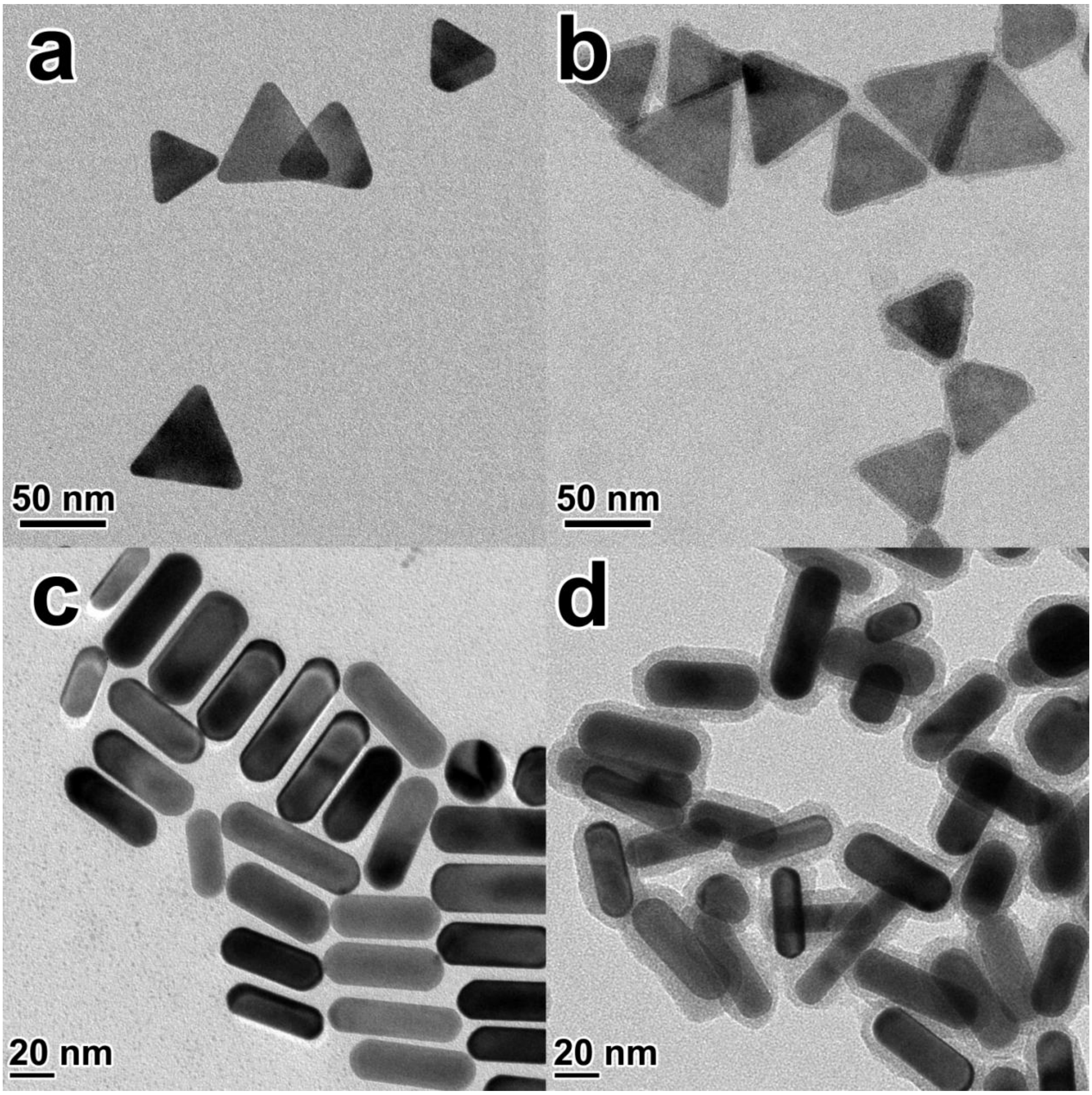

Figure 3.3 TEM images of silver nanoplates (a) before and (b) after coating with titanium glycolate, and gold nanorods (c) before and (d) after coating with titanium glycolate.

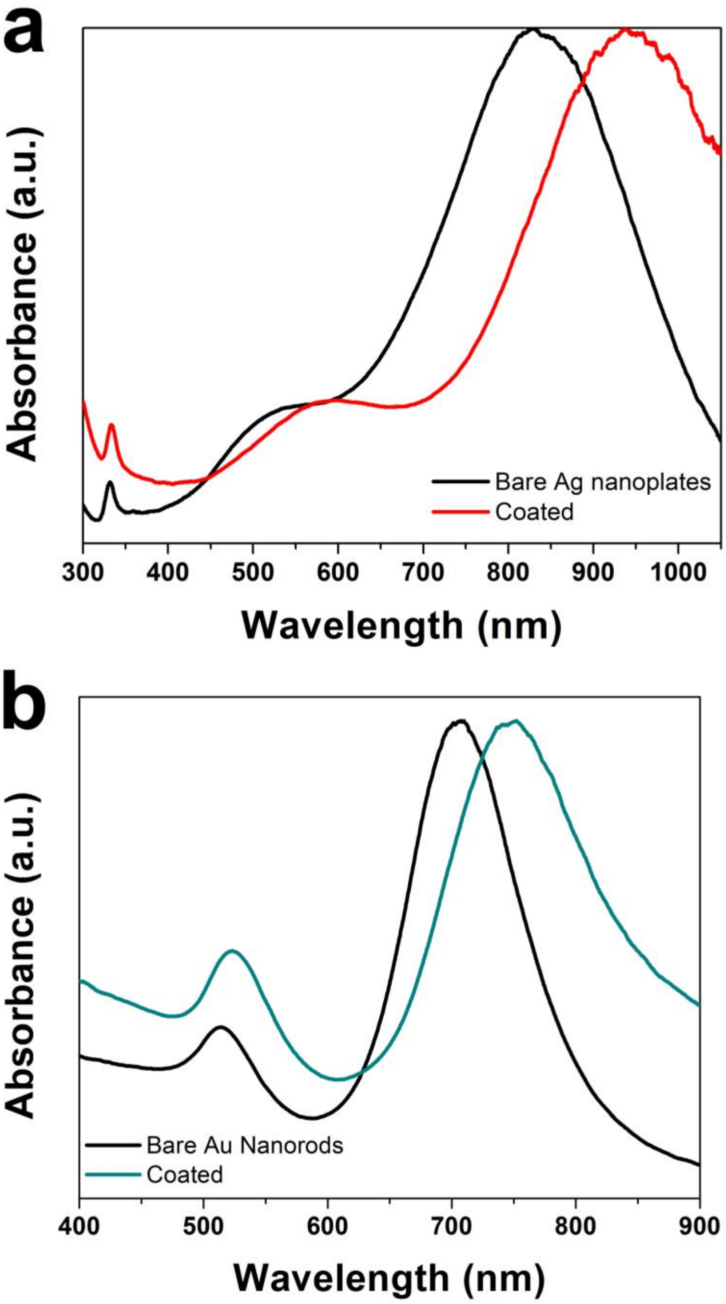

Figure 3.4 UV-Vis absorption spectra of (a) silver nanoplates and (b) gold nanorods before and after coating with titanium glycolate.

and 3.5d. The increase in the thickness of the titanium glycolate layer shows a minimal change on the peak absorption of the surface plasmon resonance (Figure 3.5e). Upon coating with a thin layer, the peak of the longitudinal mode of the gold nanorods redshifts by ~30 nm from 710 to 741 nm; however, the thickest measured coating only further increases the redshift by ~10 nm. This is presumed to indicate that the initial layers deposited form a full coating around the entire particle and subsequent layers of titanium glycolate do not significantly change the dielectric environment surrounding the particle, thus there is little effect on the peak absorption.

Beyond these metal nanoparticle templates, coating titanium glycolate onto larger templates can be accomplished as well. Figure 3.6a shows the TEM image of an uncoated silica sphere of approximately 280 nm. Silica microspheres can be easily coated with titanium glycolate simply by changing the concentration of the TBOT:ethylene glycol precursor to 2.5 vol. % TBOT, as shown in Figure 3.6b. The coating is highly uniform with a thickness of approximately 7 nm. Thicker coatings of titanium glycolate can also be made by recoating the templates as shown in Figure 3.6c and 3.6d. By removing the templates after coating, washing to remove the reaction solution, and dispersing in a new coating solution, additional layers of titanium glycolate can be deposited. The limit of this recoating procedure, however, is approximately six coatings or ~40 nm, after which significant self-nucleation occurs. It is our belief that this may be further extended with further modification of the procedure such as decreased concentration of TBOT in the injection solution, though this has not been tested. In addition to silica, resorcinol-formaldehyde (RF) polymer spheres can be coated with titanium glycolate. The coating on RF, as with the case of SiO_2, is highly uniform with a thickness of approximately 7 nm. Figure 3.7 shows low

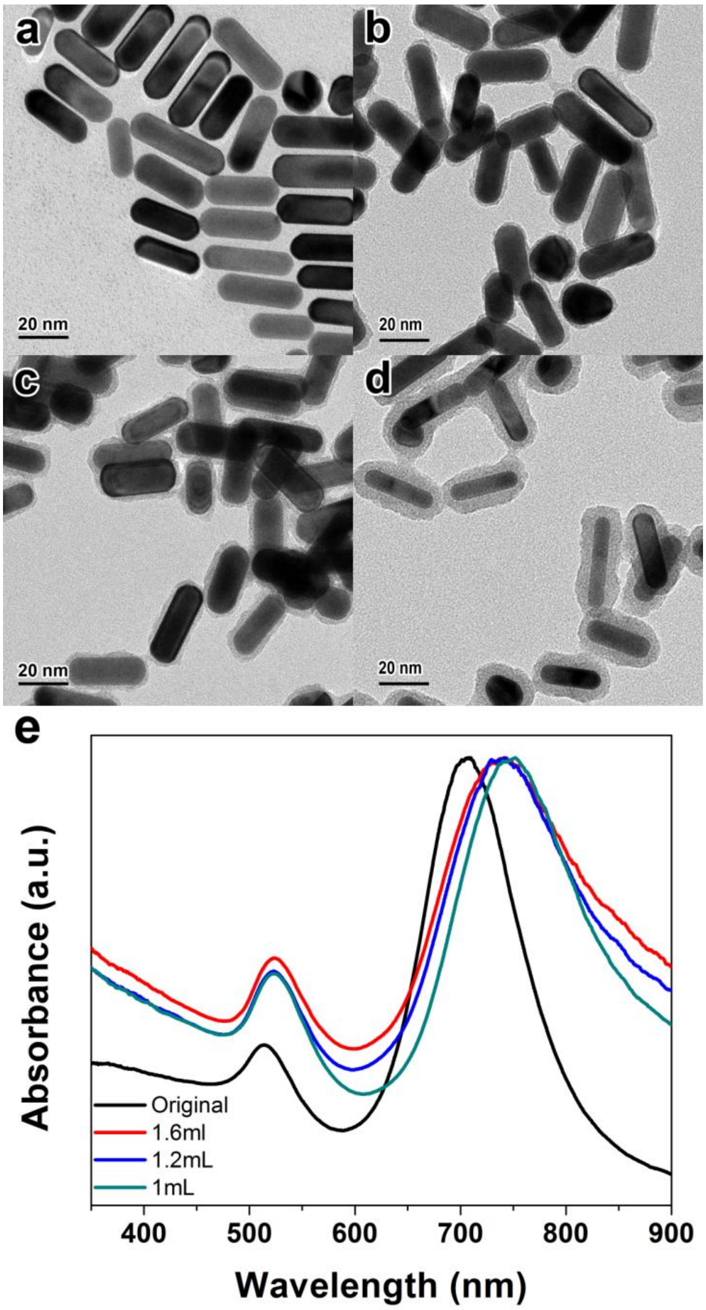

Figure 3.5 (a-d) TEM images of different thicknesses of titanium glycolate coating on gold nanorod templates by changing the amount of gold nanorods added to the coating solution. (e) UV-Vis absorption spectra of gold nanorods indicating peak position changes after coating with different thicknesses of titanium glycolate.

magnification TEM images of both SiO_2 and RF template coatings which show that the coating is uniform across multiple particles and there is little to no self nucleated material.

Each of the four coated materials shown can also be refluxed in an aqueous solution to crystallize the titanium glycolate to TiO_2. Figure 3.8a-d shows TEM images of each of these particles after refluxing. Similar to the coating on gold and silver nanoparticles discussed above, the titanium glycolate becomes noticeably granulated, indicating a change from an amorphous coating to crystalline. As mentioned above, the crystallization of TiO_2 in an aqueous solution forms a mixture of anatase and brookite phases; however the brookite phase can be inhibited by the addition of fluoride. It should be noted that in the case of refluxing titanium glycolate coated SiO_2 microspheres, the fluoride source (NaF) yields a basic environment which at elevated temperature induces the dissolution of the SiO_2 template, as seen in Figure 3.8c. The crystallization of these materials can be monitored by Raman spectroscopy, as shown in Figure 3.8e. This method is preferable compared to X-ray diffraction (XRD) because when the templates are still present, the contribution to the signal for XRD by the template is significantly greater than that of the crystalline TiO_2 due to both its relatively low percent composition as well as its low crystallinity. Raman spectroscopy on the other hand can better measure the surface of the core@shell composite where TiO_2 is primarily located. Figure 3.8e shows the Raman spectra of refluxed SiO_2@titanium glycolate, refluxed Au nanorods@titanium glycolate, and titanium glycolate particles without a template or refluxing. Both spectra of the refluxed core@shell particles show peaks indicative of anatase phase TiO_2 at 142, 397, 510, and 639 cm^{-1} which can be attributed to the E_g, B_{1g}, A_{1g}, and E_g symmetries

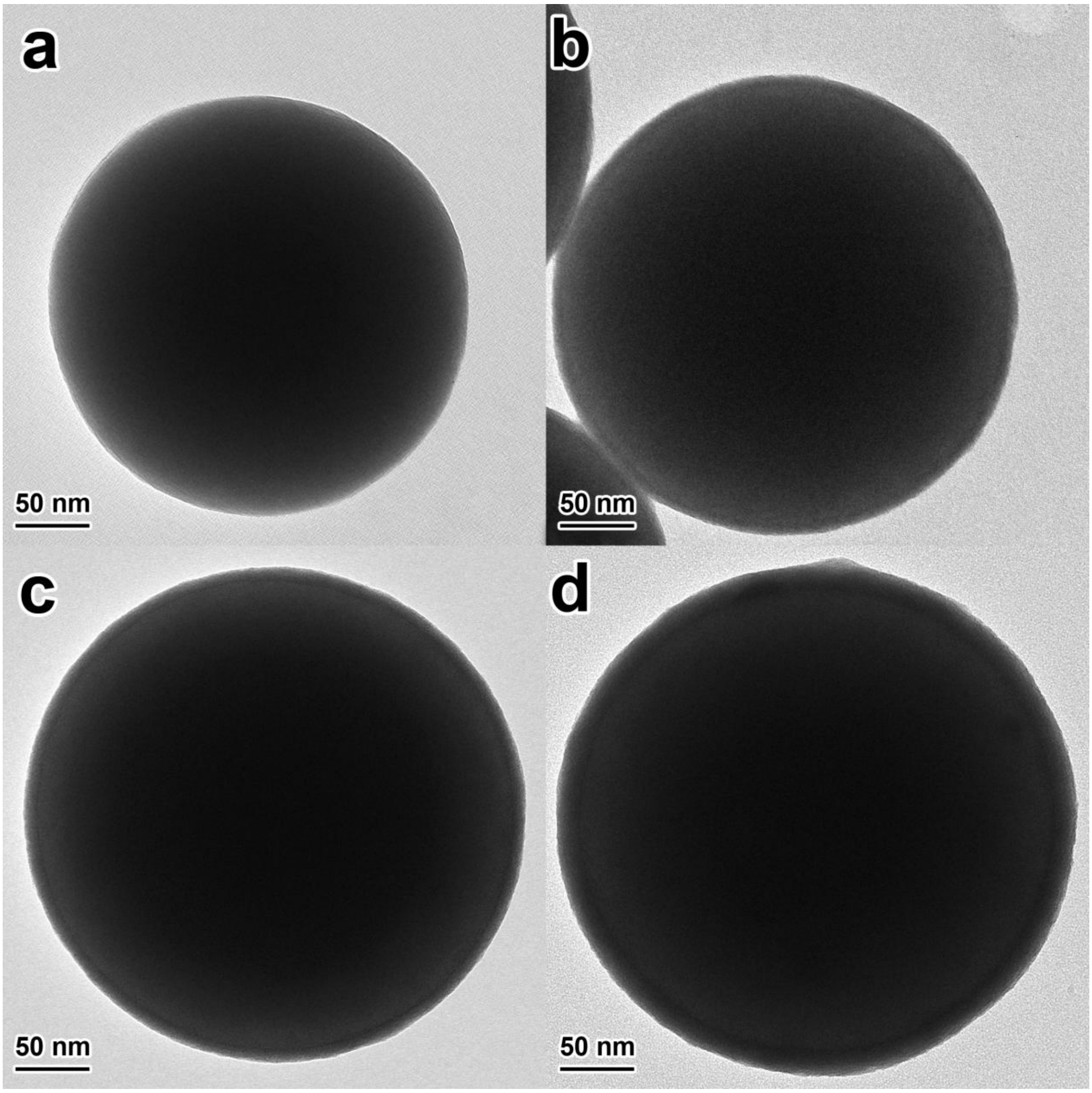

Figure 3.6 TEM images of (a) bare SiO_2, and (b) single, (c) double, and (d) quadruple coatings of titanium glycolate on SiO_2.

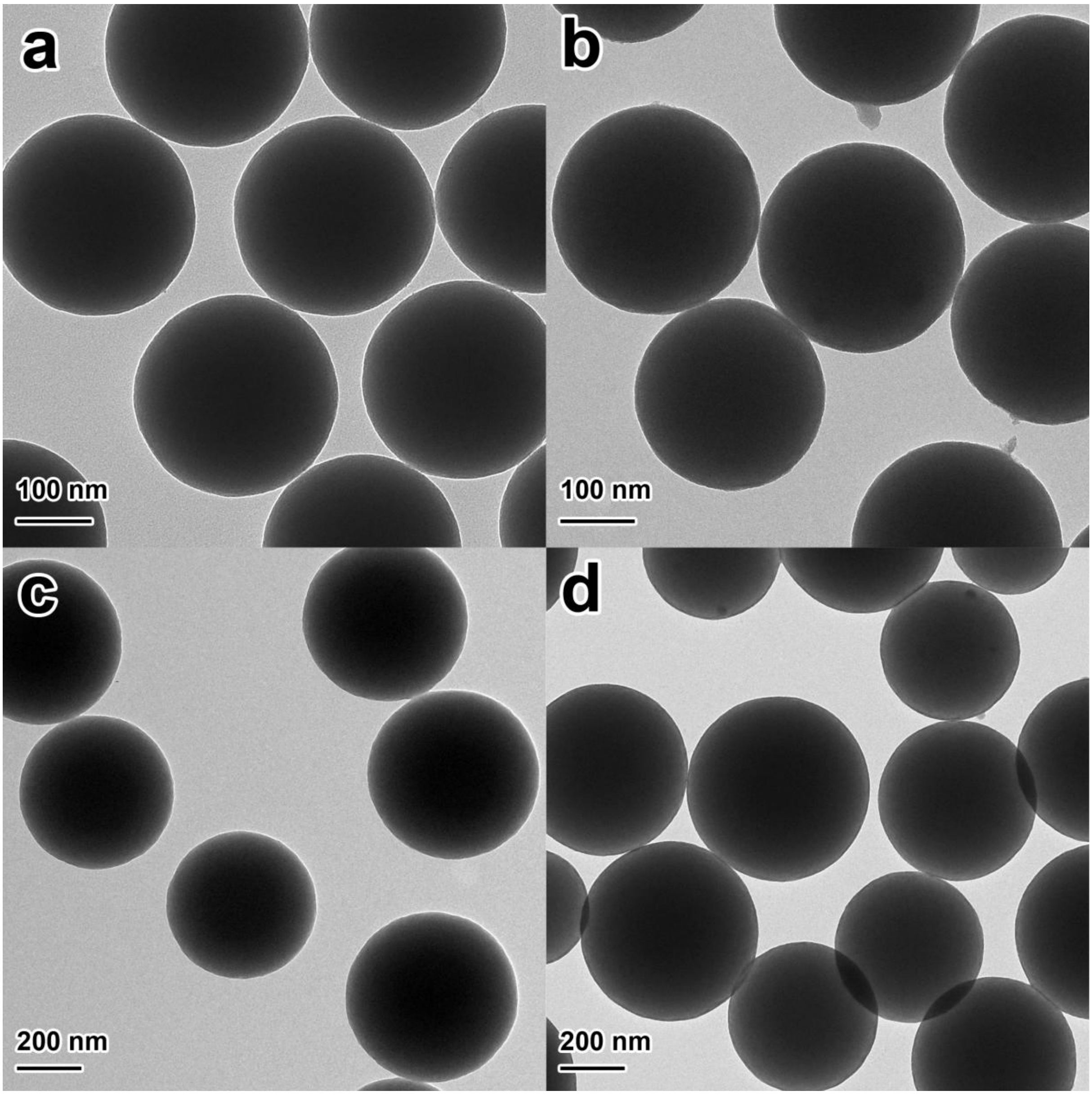

Figure 3.7 TEM images of SiO_2 and RF polymer microspheres before (a,c) and after (b,d) coating with titanium glycolate.

respectively.[47] Due to the use of fluoride during the refluxing process, there is no indication of brookite phase in the Raman spectra. The bare, non-refluxed titanium glycolate particles show no discernable peaks, typical of its amorphous nature.[48]

In addition to crystallization through refluxing in an aqueous solution, the titanium glycolate coating can also be crystallized to TiO_2 through calcination. This is best exemplified using SiO_2@titanium glycolate since the silica core can easily be removed via etching with sodium hydroxide after calcination to yield a hollow TiO_2 shell. Figure 3.9a-d shows TEM images of hollow TiO_2 shells which were prepared by calcination of the SiO_2@titanium glycolate composite followed by etching to remove the SiO_2 core. It is apparent from the images that the morphology of the resulting TiO_2 shell is quite different than the crystalline shells produced by refluxing in an aqueous solution. When the samples are calcined at 400 °C, the hollow TiO_2 shells appear to consist of smaller primary particles connected to form a shell. It is of note here that the shells appear to contract in size after calcination which is consistent with contraction seen in titanium glycolate microspheres.[35] As the calcination temperature is increased, the shells become much denser and appear to consist of larger crystal domains. As these crystal domains grow larger, the shells have a greater tendency to break apart into smaller crystals as shown in the TEM images in Figure 3.10. X-ray diffractograms of the hollow TiO_2 shells, as shown in Figure 3.9e, show peaks at $2\theta = 25.3, 36.9, 37.8, 38.5, 48.0, 53.8$ and $54.9°$ which are attributed to the (101), (103), (004), (112), (200), (105) and (211) planes of the anatase TiO_2 crystal lattice. Further the sharpness of the peaks indicates that the samples are of a high degree of crystallinity. The retention of anatase phase and inhibition of rutile formation may be explained by the presence of SiO_2. In our previous studies we have

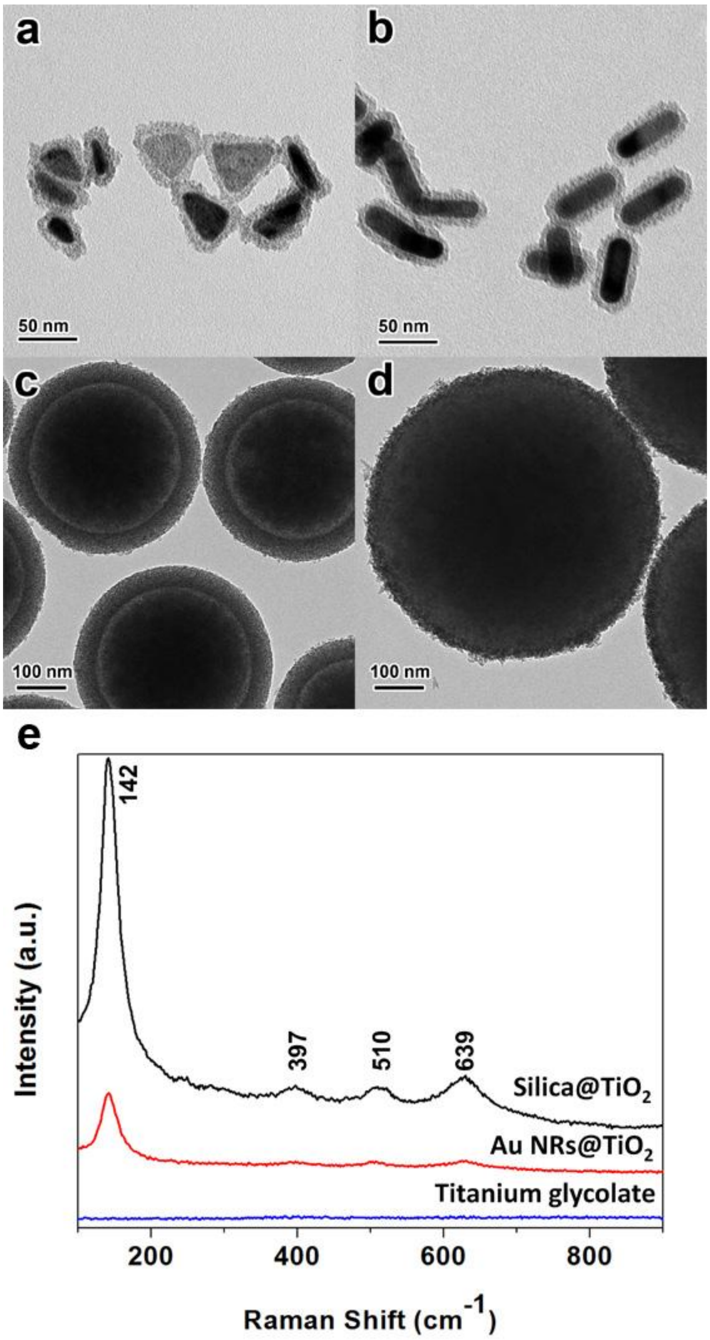

Figure 3.8 TEM images of titanium glycolate coatings crystallized through refluxing in water on (a) silver nanoplates, (b) gold nanorods, (c) SiO_2 microspheres, and (d) resorcinol-formaldehyde polymer spheres. (e) Raman spectra of titanium glycolate coatings on gold nanorods and SiO_2 microspheres after refluxing, indicating conversion to anatase crystal phase. λ_{ex} = 532 nm.

seen both an inhibition of TiO_2 crystal grain growth by SiO_2 as well as the inhibition of transition to the rutile crystalline phase,[49,50] even as the individual grains grow larger than the typical size where transition begins of ~14 nm.[51] It is presumed that here, although SiO_2 is present in the core and not as a shell, the penetration of SiO_2 oligomers from the surface of the core into the titanium glycolate shell layer successfully inhibits transition to the rutile phase, even as the grain size grows larger than 14 nm. From the XRD data, the increase in the sharpness of the peaks indicates an increase in the size of the crystal grains of the TiO_2 hollow shells which can be approximated using the Scherrer equation. Figure 3.11a summarizes the increase in the calculated grain size versus the calcination temperature. The SiO_2@titanium glycolate samples calcined as low as 400 °C still show a remarkably high degree of crystallinity, with grain sizes of approximately 11 nm. Once calcined above 500 °C, the 14 nm threshold is passed while the TiO_2 shells produced are still pure anatase phase. Calcination at 600 °C results in calculated grain sizes of ~18nm, and once the SiO_2@titanium glycolate samples have been calcined to 800 °C, the grain size plateaus at ~23 nm. It is interesting to note that as the calcination temperature is increased to 900 °C, the grain size does not change appreciably. This is attributed to the fact that above 800 °C, the shell morphology significantly degrades and the shells break apart. As this occurs it can then be hypothesized that the broken shells do not fuse together and as such do not grow further. The surface areas of the hollow TiO_2 shells after calcination were measured using the multi-point Brunauer-Emmett-Teller (BET) method from the adsorption branch in the relative pressure range of 0.05–0.25, which is summarized in Figure 3.11b. The typical isotherm shows a type IV isotherm with hysteresis indicating presence of mesopores.

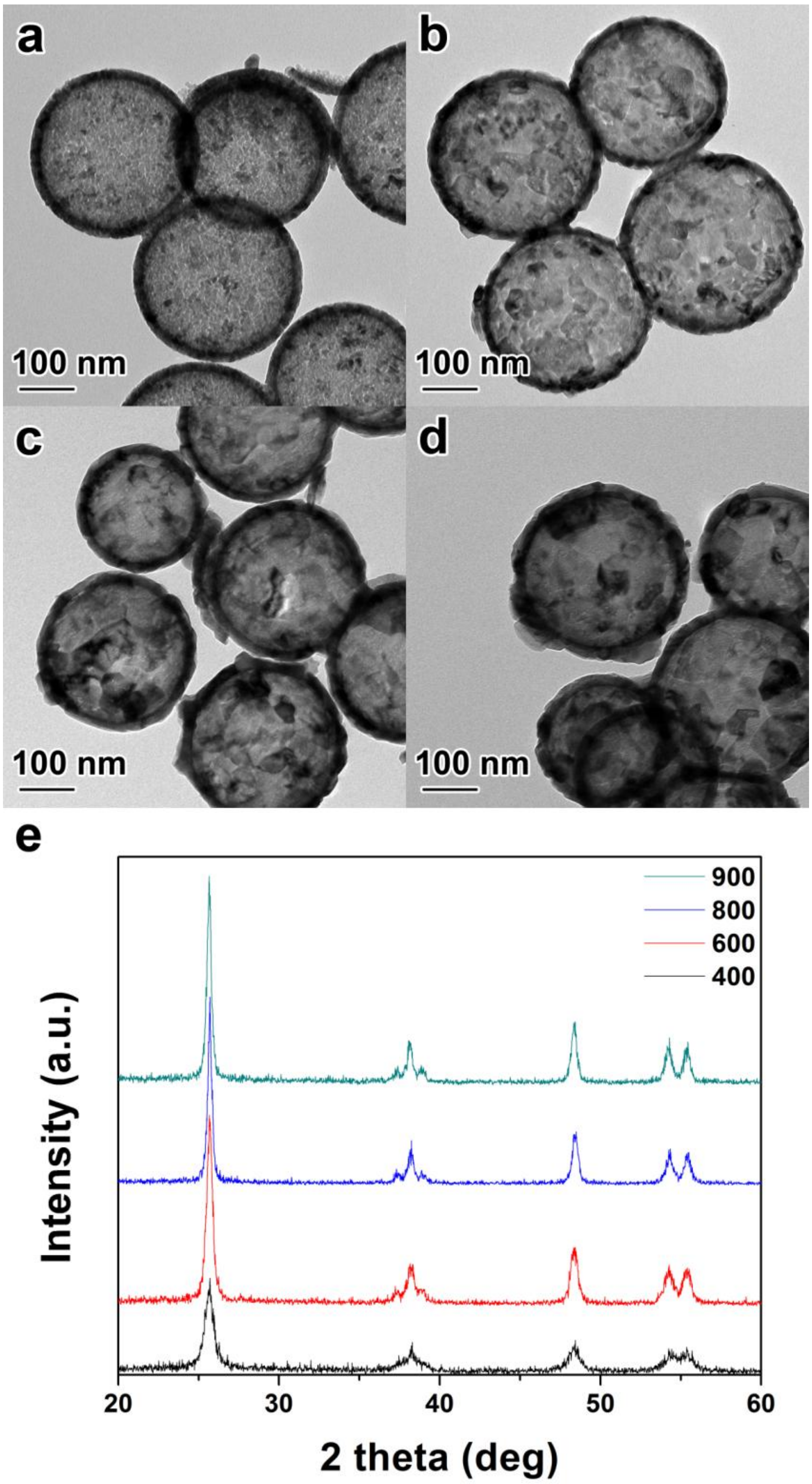

Figure 3.9 TEM images of hollow TiO_2 shells obtained by calcination of SiO_2@titanium glycolate, followed by etching. Samples shown were calcined at (a) 400, (b) 600, (c) 800 and (d) 900 °C. (e) XRD diffractograms of hollow TiO_2 shells obtained by calcination and etching of SiO_2@titanium glycolate indicating conversion to anatase crystal phase.

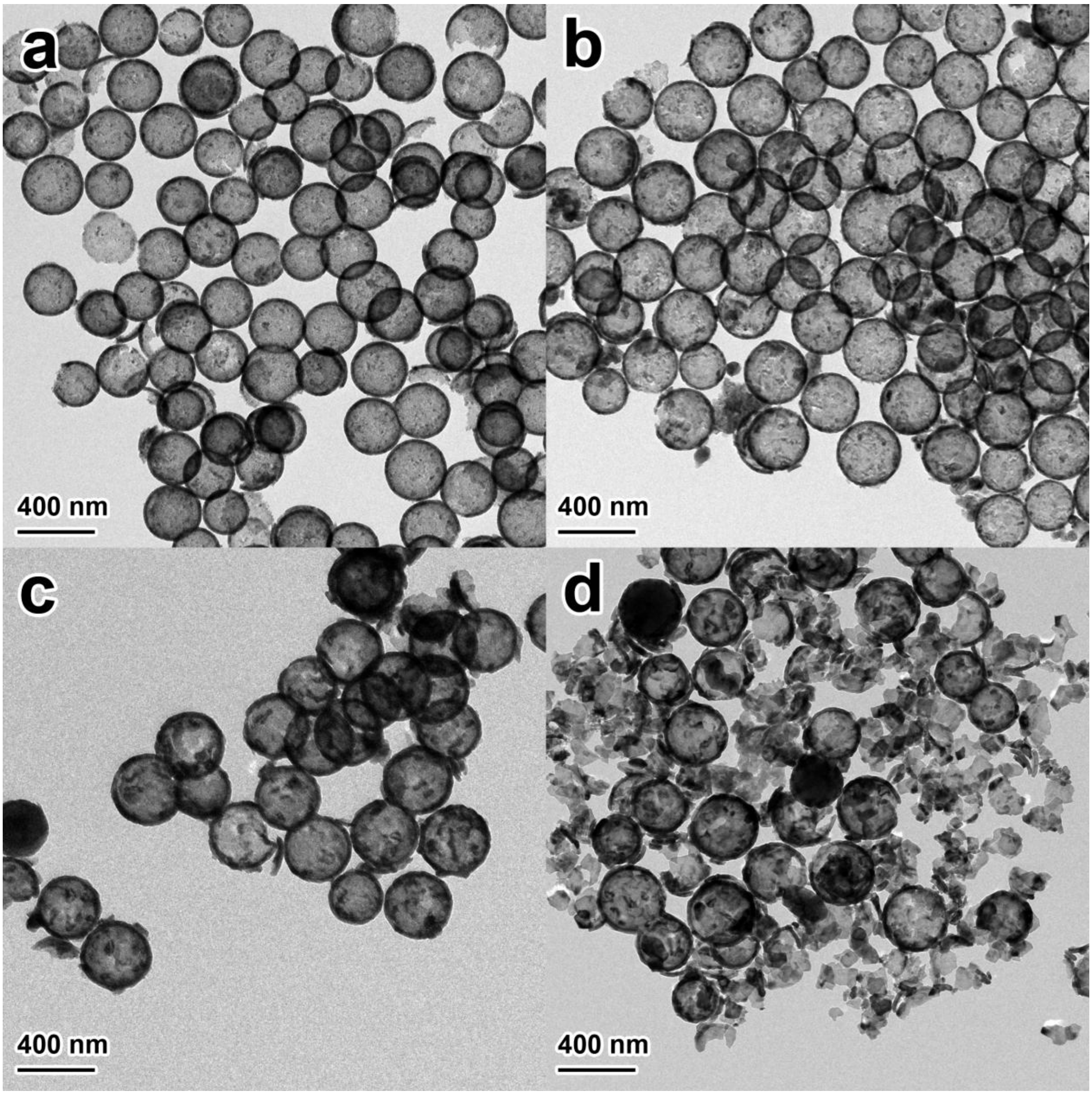

Figure 3.10 Low magnification TEM images of hollow TiO_2 shells obtained by calcination of SiO_2@titanium glycolate, followed by etching. Samples shown were calcined at (a) 400, (b) 600, (c) 800 and (d) 900 °C.

Since the hollow TiO_2 shells display such a high degree of crystallinity, the application of the hollow shells towards photocatalysis becomes of interest. The photocatalytic activity of the hollow TiO_2 shells produced after calcination and etching of the SiO_2@titanium glycolate composites was demonstrated by measuring the degradation of Rhodamine B (RhB) dye under UV irradiation over time. Figure 3.12a displays the change in concentration of the dye versus time as measured by the decrease in absorbance of the characteristic RhB absorption peak at 533 nm. The blank sample without catalyst shows minimal degradation over the one hour time period measured whereas all hollow TiO_2 samples showed at least 90% degradation in the same timeframe. The best sample was the hollow TiO_2 shells produced after calcination at 700 °C. This sample showed a photocatalytic activity comparable to P25 TiO_2. This activity is attributed to the high degree of crystallinity of the sample, which showed a grain size of ~20 nm. The samples calcined at higher temperatures were lower in activity even though, by calculation from the XRD data, the grain sizes of both were ~23 nm. The difference in the photocatalytic activity of these samples may be attributed to the fact that the sample calcined at 700 °C has a surface area of approximately 56 m^2 / g where the samples calcined at 800 and 900 °C have surface areas of 33 and 25 m^2 / g, respectively (Figure 3.11b). In addition to the surface area difference, the sample calcined at 700 °C retains the hollow shell morphology which allows it to be more easily dispersed in the photocatalysis reaction solution. The sample calcined at 600 °C also shows a higher photocatalytic activity despite a lower grain size than the samples calcined at 800 and 900 °C which provides more evidence that there is a benefit to retaining the shell morphology and there is a midpoint between the benefits of an increased grain size and surface area, which has been

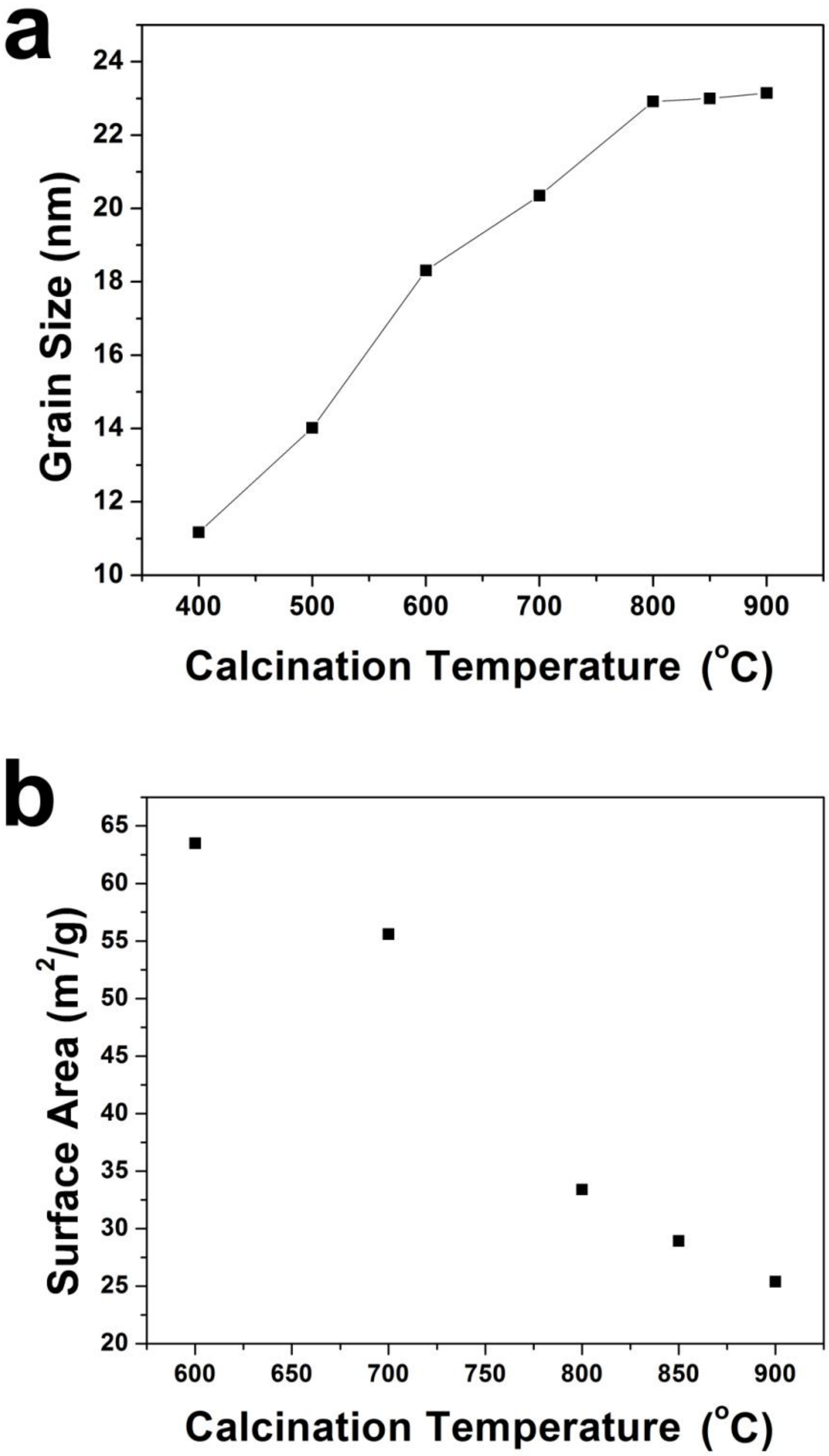

Figure 3.11 (a) Summary of grain sizes of crystalline TiO_2 hollow shells as calculated by the Scherrer equation versus the calcination temperature. (b) Summary of the surface areas measured by the multi point BET method of hollow TiO_2 versus the calcination temperature.

shown previously.[49] Figure 3.12b shows the linear relationship of plotting ln (C/C_0) versus reaction time while irradiated, indicating first order reaction kinetics. Each sample tested matches first order kinetics with R^2 values of at least 0.99. Using the formula $\ln(C/C_0) = -kt$, we can determine the apparent rate constant, *k*. From this date it is noticed that the sample calcined at 700 °C and P25 are quite similar in activity with *k* values of ~0.086 min^{-1} for each. As expected the *k* values then decrease to 0.046, 0.038, and 0.035 min^{-1} for the samples calcined at 600, 800, and 900 °C, respectively. The reaction kinetics further show that the sample calcine at 700 °C has an optimal grain size, surface area, and morphology which allows it to have a photocatalytic activity which is approximately equal to that of P25 TiO_2.

3.3.2 Metal Ion Doped Titanium Glycolate Coating on SiO_2

In order to broaden the function of the coating of titanium glycolate onto SiO_2, the incorporation of an additional metal to act as a dopant in the TiO_2 hollow shell was tested. This is done to extend the absorption of light of the hollow shells into the visible region and thus, imrprove its ability as a photocatalyst. The incorporation of dopants into the TiO_2 crystal structure has been covered in literature, however doping of TiO_2 hollow shells has rarely been reported. This may be in part due to the tendency of these ions to disturb the crystal lattice enough to cause degradation of the shell morphology. To incorporate dopants into crystalline TiO_2, one aspect which must be considered is the oxidation state of the dopant. Literature has shown dopants such as V^{3+} to be good candidates; however this oxidation state is not stable and will frequently oxidize to the V^{5+} state, which is decidedly less active as well as toxic.[52] When considering common transition metals, Ni^{2+} appears to be a good candidate because in addition to the evidence of its improvement of TiO_2 photocatalysts, it is

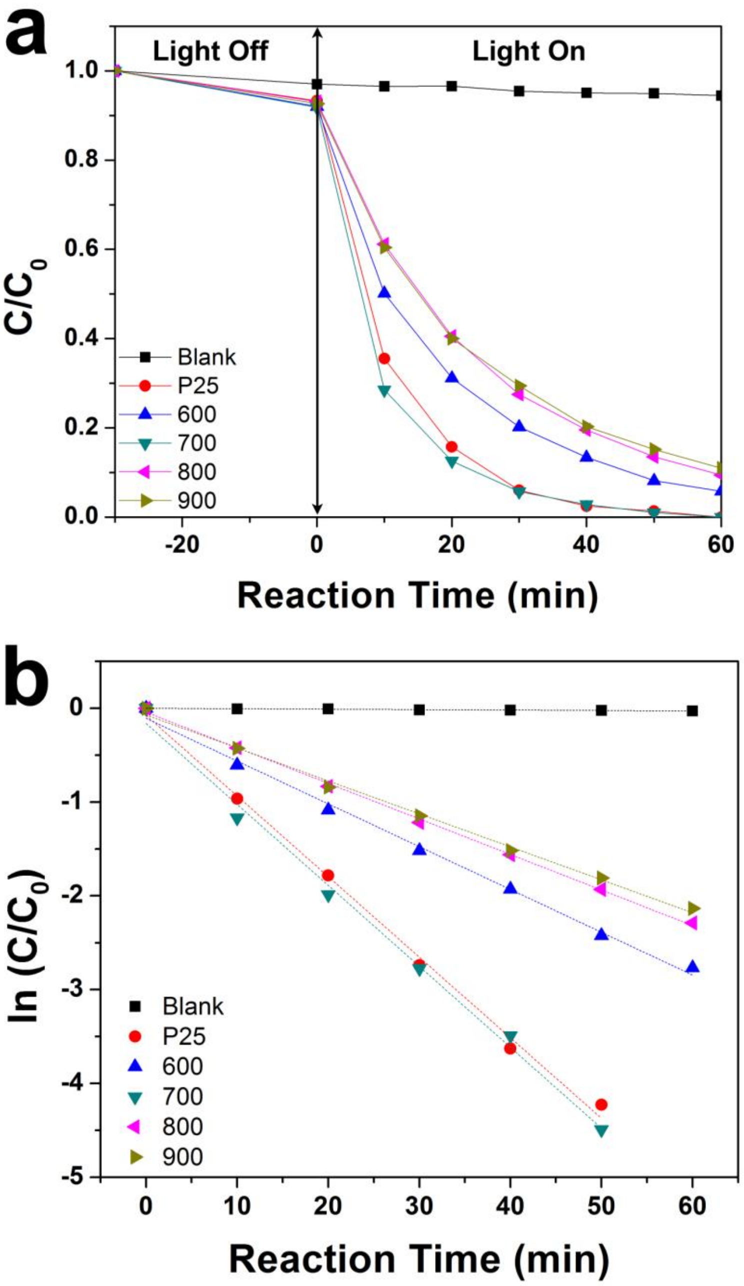

Figure 3.12 (a) Photocatalytic degradation of Rhodamine B dye by the prepared hollow TiO_2 shells under UV irradiation with a 366 nm filter. (b) Apparent reaction rate versus UV irradiation time for the same catalysts.

stable, has a low toxicity, and a high abundance. The addition of Ni^{2+} of varying mol % into the titanium glycolate precursor solution was done by simply dissolution of a Ni^{2+} salt in ethylene glycol followed by addition of TBOT. The samples could then coated onto SiO_2 and processed similar to pure titanium glycolate including calcination and etching. Figure 3.13 shows the TEM images of hollow TiO_2 with different concentrations of Ni^{2+} dopant after calcination at 600 °C and sodium hydroxide etching. 3.13a is the undoped sample whereas 3.13b is doped with 0.5 mol % Ni^{2+} and 3.13c is doped with 1.0 mol % Ni^{2+}. What is of particular interest here is that when Ni^{2+} is incorporated at a concentration of 2.5 mol %, there is a significant degradation of the hollow shell after calcination as well as a considerable amount of self-nucleated material. This suggests that lower concentrations are optimal for this procedure in order to maintain the hollow shell morphology, retain optimal dispersity in water, and to still endow it with the benefits of metal doping.

One particular reason behind the degradation of the hollow shell morphology is the rapid increase in the crystal grain size of the TiO_2 hollow shells. The role of Ni^{2+} as a promoter of the anatase to rutile phase transition has been established in literature;[5] therefore, it is likely that one prominent reason why this occurs is because of the hastening of the grain growth as compared to pure TiO_2, which is known to be a key contributor to the anatase to rutile phase transition. Though in these samples no evidence of rutile is present, this is ascribed to the effect of SiO_2 inhibiting the phase transition. Figure 3.14a shows the XRD diffractograms of Ni^{2+} doped TiO_2 with different concentrations of Ni^{2+} dopant. The patterns and peak positions clearly indicate anatase phase TiO_2 with no rutile nor any peaks from nickel metal or nickel oxides. The increase in the sharpness of the peak at approximately $2\theta = 25.3°$

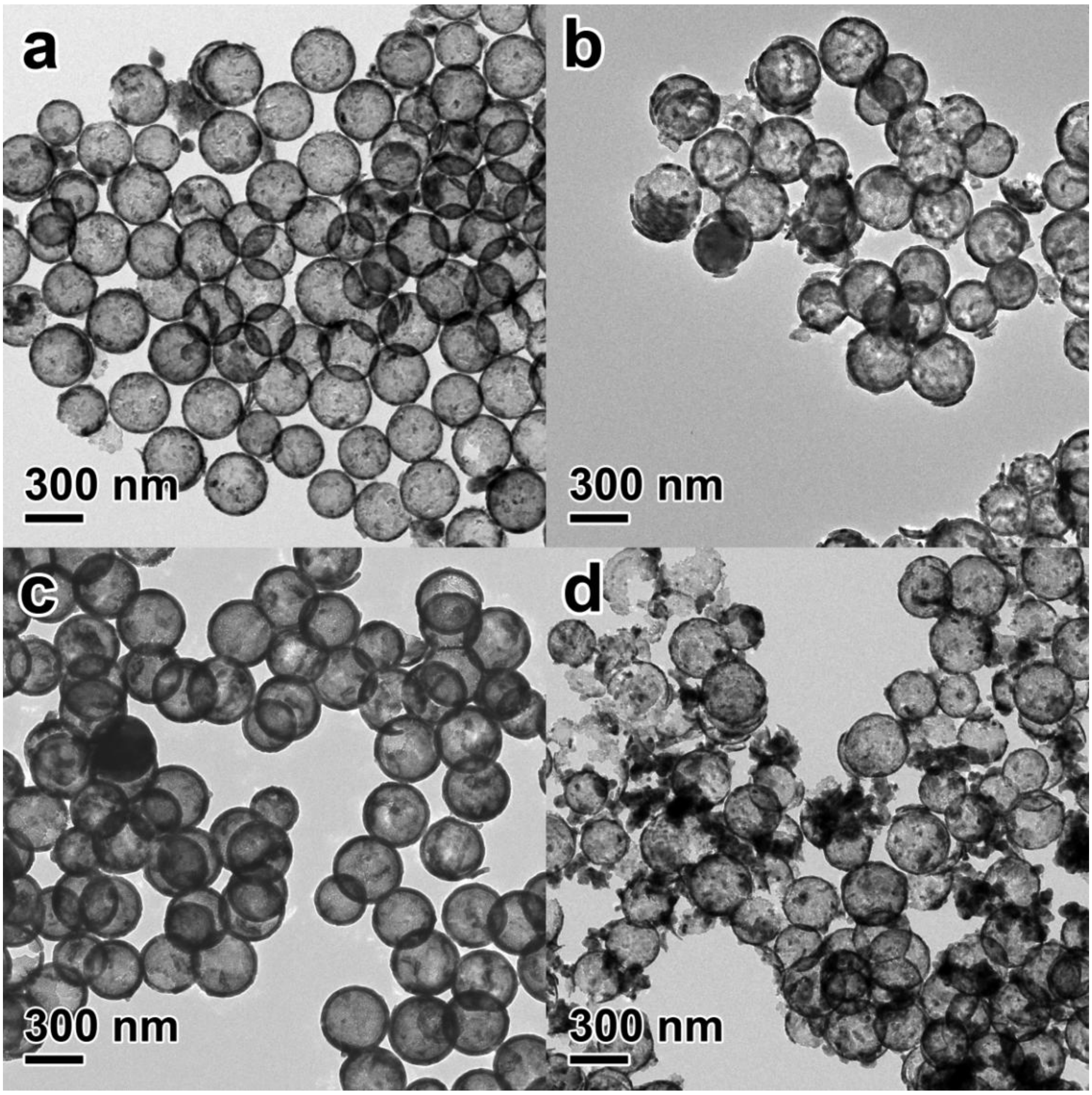

Figure 3.13 Hollow crystalline TiO_2 shells with varying Ni^{2+} dopant concentrations. (a) undoped TiO_2 (b) 0.5 mol %, (c) 1.0 mol %, and (d) 2.5 mol %. In the 2.5 mol % sample it is noticeable that the hollow morphology is degraded, with some self nucleated material present.

indicates that the crystalline grain sizes are increasing with increasing dopant concentration from undoped up to 1.0 mol % Ni^{2+} dopant. The grain size, as calculated by the Scherrer Equation, for the samples is summarized in Figure 3.14b. The grain size of the pure phase hollow TiO_2 is approximately 18.3 nm. This increases to 19.4 nm when 0.1 mol % Ni^{2+} is added and increases to 21.6 nm and 26.6 nm with the addition of 0.5 and 1.0 mol % of Ni^{2+}, respectively. Not included in this data is the XRD diffractograms for samples doped with 2.5 mol % Ni^{2+}. This data is less conclusive because of the degradation of the shell morphology and the significant percentage of self-nucleated material. It should be noted however that at this Ni^{2+} concentration, the XRD data does indicate some (~14 %) transformation of the TiO_2 from anatase to rutile.

To better investigate the hypothesis regarding the role of Ni^{2+} in increasing the grain size of the TiO_2, other metal ions were used as dopants into the TiO_2 crystal structure. A recent survey of the literature regarding the role of metal dopants on the anatase to rutile transition by Hanaor and Sorrell resulted in a plot of Shannon-Prewitt ionic radius versus metal valence which yields some predictability to which metal dopant will or will not promote or inhibit the phase transition.[5] According to our data, Ni^{2+} promoted the increase in grain size as compared to pure phase TiO_2 and it is considered to be a promoter of the transition from anatase to rutile. This implies then that a metal which should act as an inhibitor of the phase transition should also retard the growth of the TiO_2 crystalline grains. This was tested through the addition of Sr^{2+} as a dopant. According to the plot by Hanaor and Sorrell, although the valence is the same between nickel and strontium, Sr^{2+} acts as an inhibitor because of the larger ionic radius. Figure 3.15a shows the XRD diffractograms of TiO_2 shells with the

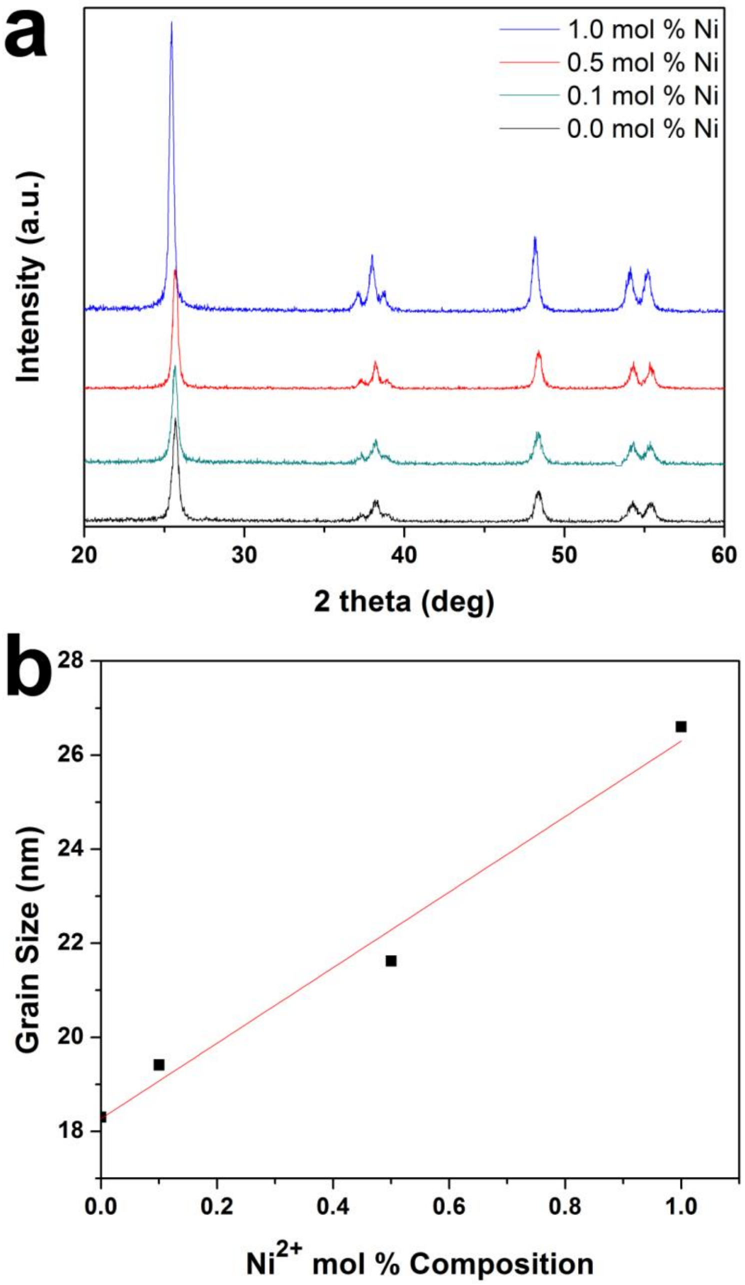

Figure 3.14 (a) XRD diffractograms show no peaks to indicate either metallic Nickel or NiO present and show only anatase TiO_2. (b) Summary of the increase in TiO_2 grain size with the increase in dopant concentration.

incorporation of 1.0 mol % of different metal ion dopants. The XRD pattern of the Sr^{2+} doped sample is less sharp than both the pure TiO_2 hollow shells and the Ni^{2+} doped samples, indicating a lesser degree of crystallinity. Indeed, the calculated grain size is 16.4 nm compared to 18.3 nm for the pure TiO_2 and 26.6 nm for the Ni^{2+} doped sample. To further investigate this phenomenon, and to utilize the predictive ability of the correlation between Shannon-Prewitt ionic radius and the valence of the metal, Bi^{3+} was also utilized as a dopant. According to the prediction Bi^{3+}, with an ionic radius of ~103 pm and a valence of +3, it should be considered as an inhibitor as well.[53] As seen in the XRD data, the Bi^{3+} doped sample shows the smallest peak at $2\theta = 25.4°$, which corresponds to a calculated grain size of 14.6 nm. The calculated grain sizes are summarized in Figure 3.15b, where the smaller grain sizes of Bi^{3+} and Sr^{2+} are easily compared to pure TiO_2 as well as the larger grain sizes of Ni^{2+}.

Since the samples doped with Ni^{2+} had the highest crystallinity and showed a light yellow color, the visible light degradation of Rhodamine B dye (RhB) was tested with P25 as a comparison. Figure 3.16a shows the results of the test where it is apparent that although the 1.0 mol % Ni^{2+} doping improves the photocatalysis as compared to pure phase TiO_2, the photocatalytic activity is still lower than that of P25 TiO_2. Plotting $\ln (C/C_0)$ versus reaction time, as shown in Figure 3.16b shows the first order reaction kinetics of the dye degradation. The rate constants, calculated using the same method as earlier, were found to be 1.52×10^{-3}, 1.87×10^{-4}, 5.28×10^{-4}, 8.32×10^{-4} for P25, 0.0 mol % Ni^{2+}, 0.5 mol % Ni^{2+}, and 1.0 mol % Ni^{2+}, respectively. This shows that although the dopant improves the photocatalysis, other dopants need to be investigated in order to yield a photocatalyst which is superior to P25.

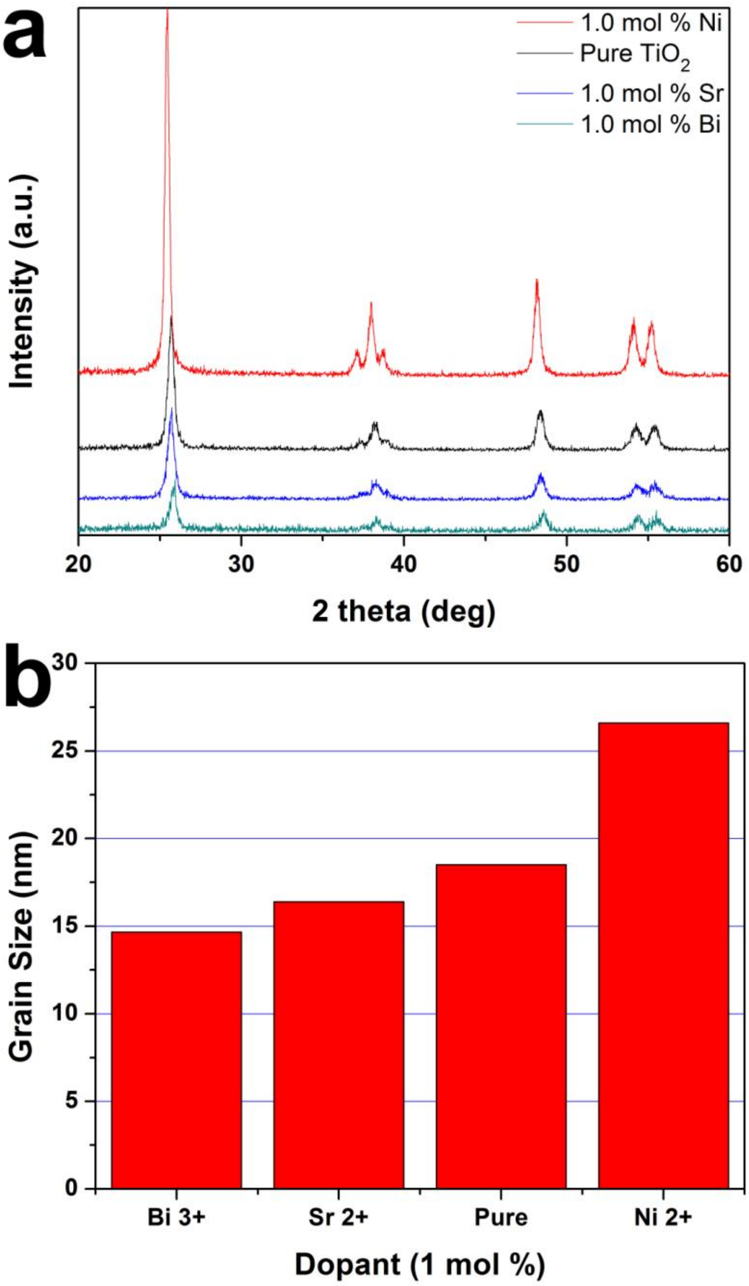

Figure 3.15 (a) XRD diffractograms of hollow TiO_2 shells doped with 1.0 mol % of different metals. (b) Summary of the grain sizes showing inhibition of grain growth versus promotion of grain growth as predicted by inhibition/promotion of anatase to rutile transition.

3.4 Conclusion

We have developed a method which allows for easy coating of a titanium glycolate layer onto nanomaterials covering a wide range of sizes, from nanoparticles to microspheres, by simply changing concentrations of the titanium alkoxide in the precursor solution. The coatings can be controlled in thickness from only a few nanometers to approximately 20 nm on nanoparticles and up to 40 nm on microspheres. The titanium glycolate coating can then be crystallized to anatase TiO_2 by either refluxing in an aqueous solution or by calcination. Calcination yields larger grain size anatase TiO_2 which, after removal of the SiO_2 template, can be converted to hollow TiO_2 shells. The photocatalytic degradation of Rhodamine B dye by the hollow TiO_2 shells yields an optimal sample which is comparable to commercial P25 TiO_2. This method may lead to easier to synthesize metal@TiO_2 composite materials which can be used for applications in sensors, photovoltaic cells, and catalysis. Further, the doping of the TiO_2 shell by inclusion of metal ions in the precursor solution allowed for an investigation of the effect of metal ions on the grain size growth of TiO_2 as well as an improved photocatalytic activity under visible light irradiation as compared to pure TiO_2.

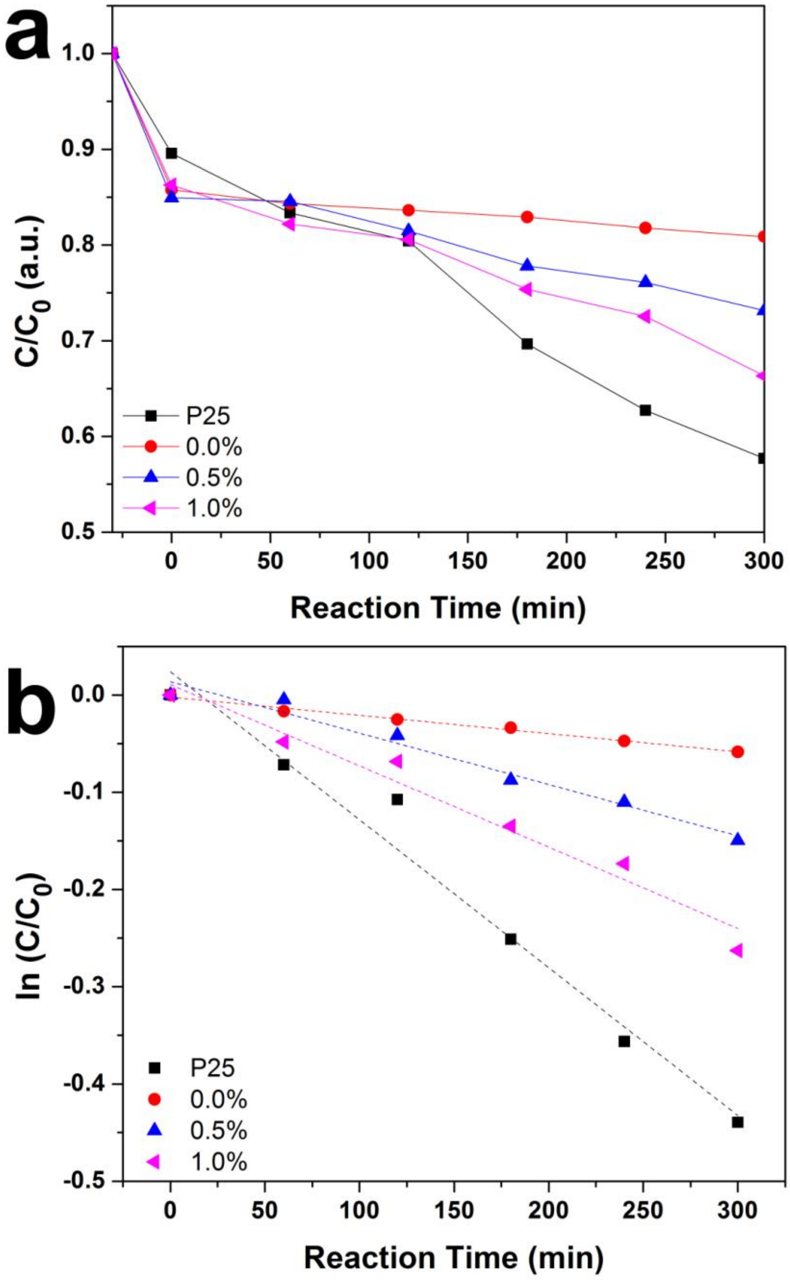

Figure 3.16 a) Visible light degradation of Rhodamine B dye by catalysts of different Ni^{2+} dopant concentrations. b) Kinetic plot of dye degradation showing first order degradation of the dye by the Ni^{2+} doped and P25 photocatalysts.

3.5 References

(1) O'Regan, B.; Gratzel, M. *Nature* **1991**, *353*, 737.

(2) Chen, X.; Mao, S. S. *Chem. Rev.* **2007**, *107*, 2891.

(3) Chen, D.; Caruso, R. A. *Adv. Funct. Mater.* **2013**, *23*, 1356.

(4) Dahl, M.; Liu, Y.; Yin, Y. *Chem. Rev.* **2014**, *114*, 9853.

(5) Hanaor, D.; Sorrell, C. *J. Mater. Sci.* **2011**, *46*, 855.

(6) Furube, A.; Du, L.; Hara, K.; Katoh, R.; Tachiya, M. *J. Am. Chem. Soc.* **2007**, *129*, 14852.

(7) Awazu, K.; Fujimaki, M.; Rockstuhl, C.; Tominaga, J.; Murakami, H.; Ohki, Y.; Yoshida, N.; Watanabe, T. *J. Am. Chem. Soc.* **2008**, *130*, 1676.

(8) He, J.; Ichinose, I.; Kunitake, T.; Nakao, A.; Shiraishi, Y.; Toshima, N. *J. Am. Chem. Soc.* **2003**, *125*, 11034.

(9) Zaera, F. *Chem. Soc. Rev.* **2013**, *42*, 2746.

(10) Zhong, Z.; Yin, Y.; Gates, B.; Xia, Y. *Adv. Mater.* **2000**, *12*, 206.

(11) Li, G. K.; Zhang, Z. C. *Mater. Lett.* **2004**, *58*, 2768.

(12) Ye, M.; Zhang, Q.; Hu, Y.; Ge, J.; Lu, Z.; He, L.; Chen, Z.; Yin, Y. *Chem. Eur. J.* **2010**, *16*, 6243.

(13) Lee, I.; Joo, J. B.; Yin, Y.; Zaera, F. *Angew. Chem. Int. Ed.* **2011**, *50*, 10208.

(14) Joo, J. B.; Zhang, Q.; Lee, I.; Dahl, M.; Zaera, F.; Yin, Y. *Adv. Funct. Mater.* **2012**, *22*, 166.

(15) Li, W.; Zhao, D. *Adv. Mater.* **2013**, *25*, 142.

(16) Lou, X. W.; Archer, L. A. *Adv. Mater.* **2008**, *20*, 1853.

(17) Li, W.; Yang, J.; Wu, Z.; Wang, J.; Li, B.; Feng, S.; Deng, Y.; Zhang, F.; Zhao, D. *J. Am. Chem. Soc.* **2012**, *134*, 11864.

(18) Pastoriza-Santos, I.; Koktysh, D. S.; Mamedov, A. A.; Giersig, M.; Kotov, N. A.; Liz-Marzán, L. M. *Langmuir* **2000**, *16*, 2731.

(19) Mayya, K. S.; Gittins, D. I.; Caruso, F. *Chem. Mater.* **2001**, *13*, 3833.

(20) Koktysh, D. S.; Liang, X.; Yun, B. G.; Pastoriza-Santos, I.; Matts, R. L.; Giersig, M.; Serra-Rodríguez, C.; Liz-Marzán, L. M.; Kotov, N. A. *Adv. Funct. Mater.* **2002**, *12*, 255.

(21) Liz-Marzán, L. M.; Mulvaney, P. *J. Phys. Chem. B* **2003**, *107*, 7312.

(22) Tom, R. T.; Nair, A. S.; Singh, N.; Aslam, M.; Nagendra, C. L.; Philip, R.; Vijayamohanan, K.; Pradeep, T. *Langmuir* **2003**, *19*, 3439.

(23) Chen, Y.; Zhu, B.; Yao, M.; Wang, S.; Zhang, S. *Catal. Commun.* **2010**, *11*, 1003.

(24) Goebl, J.; Joo, J. B.; Dahl, M.; Yin, Y. *Catal. Today* **2014**, *225*, 90.

(25) Zhang, Q.; Lima, D. Q.; Lee, I.; Zaera, F.; Chi, M.; Yin, Y. *Angew. Chem.* **2011**, *123*, 7226.

(26) Demirörs, A. F.; van Blaaderen, A.; Imhof, A. *Langmuir* **2010**, *26*, 9297.

(27) Hirakawa, T.; Kamat, P. V. *J. Am. Chem. Soc.* **2005**, *127*, 3928.

(28) Qi, J.; Dang, X.; Hammond, P. T.; Belcher, A. M. *ACS Nano* **2011**, *5*, 7108.

(29) Zhang, N.; Liu, S.; Fu, X.; Xu, Y.-J. *J. Phys. Chem. C* **2011**, *115*, 9136.

(30) Du, P.; Cao, Y.; Li, D.; Liu, Z.; Kong, X.; Sun, Z. *RSC Adv.* **2013**, *3*, 6016.

(31) Mubeen, S.; Lee, J.; Singh, N.; Kramer, S.; Stucky, G. D.; Moskovits, M. *Nat. Nanotechnol.* **2013**, *8*, 247.

(32) Wang, F.; Li, C.; Chen, H.; Jiang, R.; Sun, L.-D.; Li, Q.; Wang, J.; Yu, J. C.; Yan, C.-H. *J. Am. Chem. Soc.* **2013**, *135*, 5588.

(33) Reeves, R. E.; Mazzeno, L. W. *J. Am. Chem. Soc.* **1954**, *76*, 2533.

(34) Wang, D.; Yu, R.; Kumada, N.; Kinomura, N. *Chem. Mater.* **1999**, *11*, 2008.

(35) Jiang, X.; Wang, Y.; Herricks, T.; Xia, Y. *J. Mater. Chem.* **2004**, *14*, 695.

(36) Pal, M.; García Serrano, J.; Santiago, P.; Pal, U. *J. Phys. Chem. C* **2006**, *111*, 96.

(37) Yang, X.; Fu, H.; Yu, A.; Jiang, X. *J. Colloid Interf. Sci.* **2012**, *387*, 74.

(38) de Boer, M. A.; Lammertsma, K. *ChemSusChem* **2013**, n/a.

(39) Turkevich, J.; Stevenson, P. C.; Hillier, J. *Discussions of the Faraday Society* **1951**, *11*, 55.

(40) Dadosh, T. *Mater. Lett.* **2009**, *63*, 2236.

(41) Ye, X.; Zheng, C.; Chen, J.; Gao, Y.; Murray, C. B. *Nano Lett.* **2013**, *13*, 765.

(42) Zhang, Q.; Li, N.; Goebl, J.; Lu, Z.; Yin, Y. *J. Am. Chem. Soc.* **2011**, *133*, 18931.

(43) Liu, J.; Qiao, S. Z.; Liu, H.; Chen, J.; Orpe, A.; Zhao, D.; Lu, G. Q. *Angew. Chem. Int. Ed.* **2011**, *50*, 5947.

(44) Li, N.; Zhang, Q.; Liu, J.; Joo, J.; Lee, A.; Gan, Y.; Yin, Y. *Chem. Commun.* **2013**, *49*, 5135.

(45) Wang, D.; Liu, L.; Zhang, F.; Tao, K.; Pippel, E.; Domen, K. *Nano Lett.* **2011**, *11*, 3649.

(46) Zhong, L.-S.; Hu, J.-S.; Wan, L.-J.; Song, W.-G. *Chem. Commun.* **2008**, 1184.

(47) Ohsaka, T.; Izumi, F.; Fujiki, Y. *Journal of Raman Spectroscopy* **1978**, *7*, 321.

(48) Pal, M.; García Serrano, J.; Santiago, P.; Pal, U. *J. Phys. Chem. C* **2007**, *111*, 96.

(49) Dahl, M.; Dang, S.; Bong Joo, J.; Zhang, Q.; Yin, Y. *CrystEngComm* **2012**, *14*, 7680.

(50) Joo, J. B.; Zhang, Q.; Dahl, M.; Lee, I.; Goebl, J.; Zaera, F.; Yin, Y. *Energy Environ. Sci.* **2012**, *5*, 6321.

(51) Zhang, H.; F. Banfield, J. *J. Mater. Chem.* **1998**, *8*, 2073.

(52) Choi, W.; Termin, A.; Hoffmann, M. R. *J. Phys. Chem.* **1994**, *98*, 13669.

(53) Shannon, R. D. *Acta Crystallographica Section A* **1976**, *32*, 751.

Chapter 4

Synthesis of Metal-TiO_2 via Titanate Cation Exchange

4.1 Introduction

The considerable development of protocols for the synthesis of colloidal TiO_2 nanomaterials has given rise to a significant amount of control of parameters such as size and morphology.[1] Further, one avenue of morphology control which has been investigated frequently over the last decade is that of core@shell particles.[2,3] The use of SiO_2 as a hard template for TiO_2 has allowed for an additional area of research: the synthesis of titanate nanostructures. When SiO_2 is removed from amorphous TiO_2 through base etching with sodium hydroxide, the effect on the resulting TiO_2 is the formation of titanate nanostructure.[4] In the case of SiO_2@TiO_2 core@shell particles, this leaves hollow sodium titanate as a product. To produce crystalline TiO_2 from sodium titanate, it has been shown that cation exchange with a sufficient amount of an acid such as HCl or HNO_3 will yield a protonated TiO_2 which, upon calcination, forms pure phase TiO_2.[5-7] Additionally, as we have recently reported, utilizing this methodology with hollow sodium titanate shells will produce crystalline TiO_2 hollow shells after calcination, with no degradation of the morphology.[8]

Recently, these titanate nanostructures have seen more usage as inorganic sorbents and cation exchange media due to their typically high surface areas and pore volumes as well as their high ion exchange efficiency.[9,10] Various reports have shown a good capacity of titanate for adsorption of various heavy metal ions such as Zn^{2+}, Cd^{2+}, Cr^{3+}, and Hg^{2+}. Beyond the simple utilization of titanate nanostructures as cation exchange media, there are also reports of the subsequent use of the adsorbed ions such as the addition of sulfur to Cd-titanate in order to produce CdS-TiO_2 composites for the photocatalytic production of hydrogen.[11] This area of the production of TiO_2 nanomaterials via cation exchange of sodium titanate appears to have been studied little to date. In our study we first look at the production of gram scale quantities of colloidal SiO_2@TiO_2 core@shell structures. Then, upon dissolution with sodium hydroxide, the resulting hollow sodium titanate nanostructures can be formed. These hollow sodium titanate nanostructures can then be easily mixed with metal sources in order to form metal-exchanged TiO_2 nanostructures which are effectively doped-TiO_2. The cation exchange procedures done at elevated temperature result in the crystallization of TiO_2 into anatase phase crystal structure. The as prepared materials are doped-TiO_2 and can be utilized for photocatalysis, or in the case of Fe-TiO_2, the Fe^{3+} exchanged into the structure can be reduced by calcination under H_2 to form a magnetic iron oxide-TiO_2 composite. One use of TiO_2 which has been investigated in recent years takes advantage of the affinity for phosphate binding on metal oxide surfaces.[12-14] Magnetic separation of these composites allows them to become higher throughput and easier to utilize. Synthesis of a scalable and easy to use composites for the separation of phosphorylated proteins is then also demonstrated using these procedures.

4.2 Experimental

4.2.1 Synthesis of SiO_2 Spheres

SiO_2 microspheres were synthesized using a modified Stöber process. Tetraethyl orthosilicate (TEOS, 99%, 5.16 mL) was mixed with de-ionized water (25.8 mL), ethanol

(138 mL) and an aqueous solution of ammonia (26%, 3.72 mL). After stirring for 4 h at room temperature, the colloidal silica particles were separated by centrifugation and washed three times with ethanol, then re-dispersed in 30 mL of ethanol under sonication.

4.2.2 Coating of TiO_2 on SiO_2

To a freshly cleaned 125 mL Erlenmeyer flask, hydroxypropyl cellulose (HPC, 150 mg) was dissolved in a mixture of 52.5 mL absolute ethanol and 21 mL of acetonitrile (99+%). To this mixture was added 7.5 mL of the prepared SiO_2 colloid followed by stirring for 10 minutes to facilitate HPC adsorption to the SiO_2 surface. To this was added 0.6 mL of aqueous ammonia (26 %) followed by an additional 10 minutes of stirring. Separately, 3 mL of titanium n-butoxide (TBOT, 97%) was dissolved in a mixture of 9 mL ethanol and 3 mL acetonitrile. The TBOT mixture was then injected quickly to the first mixture followed by stirring for 2 h. The resulting core@shell composites were collected by centrifugation and washed three times with absolute ethanol and concentrated to 30 mL in ethanol.

4.2.3 Removal of SiO_2 Through Base Etching

Firstly, the above SiO_2@TiO_2 composite was centrifuged and dispersed into 50 mL DI water. Next, to a clean 250 mL three neck flask, 1.8 g of NaOH was added followed by the dispersed SiO_2@TiO_2 composite and an additional 130 mL of deionized water. This mixture was then heated to 100 °C and run for 75 min. After cooling to room temperature, the hollow sodium titanate was collected through centrifugation, washed twice with water and once with ethanol, then dried under vacuum.

4.2.4 Cation Exchange of M^+ into Sodium Titanate

To exchange the sodium ions with a target metal such as Fe^{3+}, a 0.100 M $Fe(NO_3)_3$ was prepared by dissolving $Fe(NO_3)_3•9H_20$ (1.010 g) in 25 mL of DI water. To this solution, 0.0500 g of the dry sodium titanate powder was added and dispersed by ultrasonication. The dispersion was then refluxed at 100 °C for the desired amount of time. Once the sample was cooled to room temperature, it was centrifuged and washed with water twice and ethanol once, then dried by vacuum. Similar procedures were done to prepare Cu^{2+} and Ni^{2+}-titanate nanostructures except in these cases 0.010 M solutions of $Cu(NO_3)_2$ and $Ni(NO_3)_2$ were utilized instead.

4.2.5 Photocatalytic Measurements

The catalyst to be tested (5 mg) was dispersed in an aqueous Rhodamine B solution (25 mL, 1.0×10^{-5} M) in a 50 mL quartz cell which was then stirred in the dark for 30 min to ensure adsorption of the dye. The lamp (500 W, tungsten) was used with a 420 nm filter in a commercial reactor system (Xujiang XPA-7). The concentration of RhB was determined by measuring the absorbance on a UV-Vis spectrophotometer (HR2000CG-UV-NIR, Ocean Optics).

4.2.6 Selective Enrichment of Phosphorylated Proteins from Protein Mixture

A mixture of the proteins β-casein, β-lactoglobulin, and horseradish peroxidase was prepared by dissolving 0.25 mg of each in 200 μL of a buffer solution containing 50% acetonitrile and 0.1% trifluoroacetic acid (TFA). The three solutions were combined then diluted to 1.00 mL to give a 0.75 mg/mL protein concentration. A 200 μL aliquot of the protein mixture was taken, to which 1 mg of the iron oxide-TiO_2 was added and the sample was mixed for 1 h to ensure adsorption. After adsorption, the sample was collected on the side of the tube using a magnet and the waste solution was removed. To the remaining material, 200 μL of fresh 50% acetonitrile 0.1% TFA water solution was added to wash. This was repeated three times, then the remaining phospoprotein-loaded composite was eluted by 50 μL of 10 % aqueous ammonia for 1 h followed by collection by magnet. The remaining supernatant containing the phosphopeptides was collected and saved in a clean tube then dried by vacuum. To prepare the sample for MALDI-TOF, the sample was dispersed in 2 μL of matrix solution (10 mg/mL sinapinic acid dissolved in 50% acetonitrile and 0.1% TFA water solution) and then 0.5 μL of the mixture was dropped directly onto a stainless steel MALDI plate for MS analysis. An aliquot (~20 μL) of the initial supernatant with the non-phosphorylated proteins was also dried, dissolved in sinapinic acid solution, and dropped on the MALDI plate for MS analysis.

4.2.7 Characterization

The morphology of each sample was observed by transmission electron microscopy (TEM, Tecnai T12, 120 kV). The crystalline structures were determined by X-ray diffraction (XRD) analysis using PANalytical Empyrean with Cu Kα radiation (λ = 1.5406 Å). The nitrogen adsorption isotherms were obtained at 77 K using a Quantachrome NOVA 4200e Surface Area and Pore Size Analyzer. The surface area was calculated from the adsorption isotherm using the multi-point BET method in the pressure range of $P/P_0 = 0.05–0.25$. Matrix assisted laser desorption/ionization mass spectra were obtained by using a Voyager-DE STR MALDI-TOF mass spectrometer (Applied Biosystems) operating in positive linear mode. The spectrometer is equipped

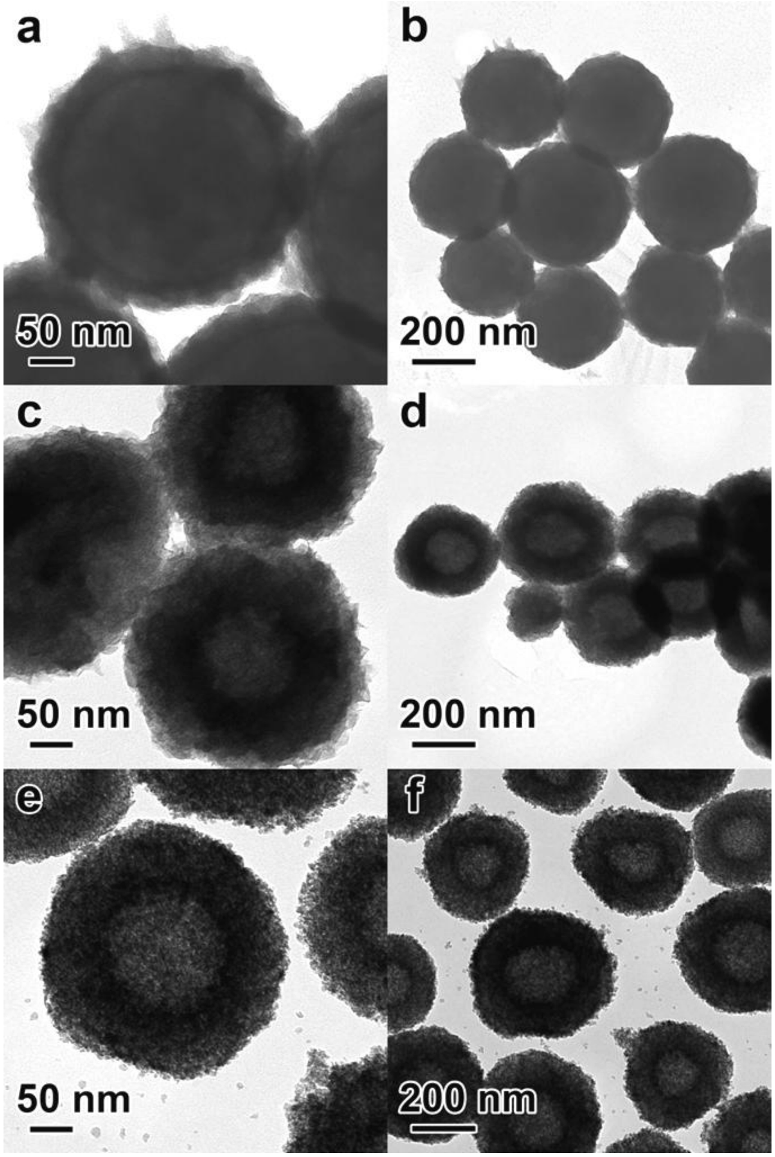

Figure 4.1 TEM images of (a) TiO_2 coated on SiO_2, (b) hollow sodium titanate after SiO_2 etching in an aqueous NaOH solution and (c) hollow, crystalline Cu-TiO_2 made by refluxing hollow sodium titanate in an aqueous $Cu(NO_3)_2$ solution for 1h.

with a pulsed nitrogen laser operated at 337 nm with 3 ns duration pulses. MS spectra were acquired as an average of 100 laser shots.

4.3 Results and Discussion

The synthesis of the materials can be divided into three main steps: (i) coating TiO_2 onto silica templates; (ii) removal of the silica and production of hollow sodium titanate through base etching of the SiO_2@TiO_2 composite; (iii) cation exchange with a target metal to form metal-TiO_2 composite structures. Representative TEM images of each of these steps are shown in Figure 4.1. The first step, coating of TiO_2 onto the silica templates, is done using a mixed solvent approach whereby acetonitrile is added to the solution in order to decrease the solubility of the titanium n-butoxide and its hydrolysis products. This in turn increases the amount of hydrolysis product collected and increases the overall yield of the reaction.[15] Further, ammonia plays a similar role in decreasing the solubility of the hydrolysis products as well as reducing the affinity of the hydrolysis product to the ethanol solvent which leads to increasing the anticoagulation and a more spherical product.[16] Figure 4.1a-b shows TEM images of the SiO_2@TiO_2 core@shell composites after coating using the mixed solvent method. The composites are then etched at 100 °C in 0.25 M NaOH. TEM images of the products after etching are shown in Figure 4.1c-d. Of particular interest is the shrinking of the cavity left after the SiO_2 core has been removed. It is well known that titanate structures, particularly sodium titanate, form flaky structures when formed from amorphous TiO_2 which can expand beyond the original dimensions.[17] In this case, the TiO_2 prepared from the mixed solvent method has a lesser degree of condensation and the shell structure expands into the empty cavity left

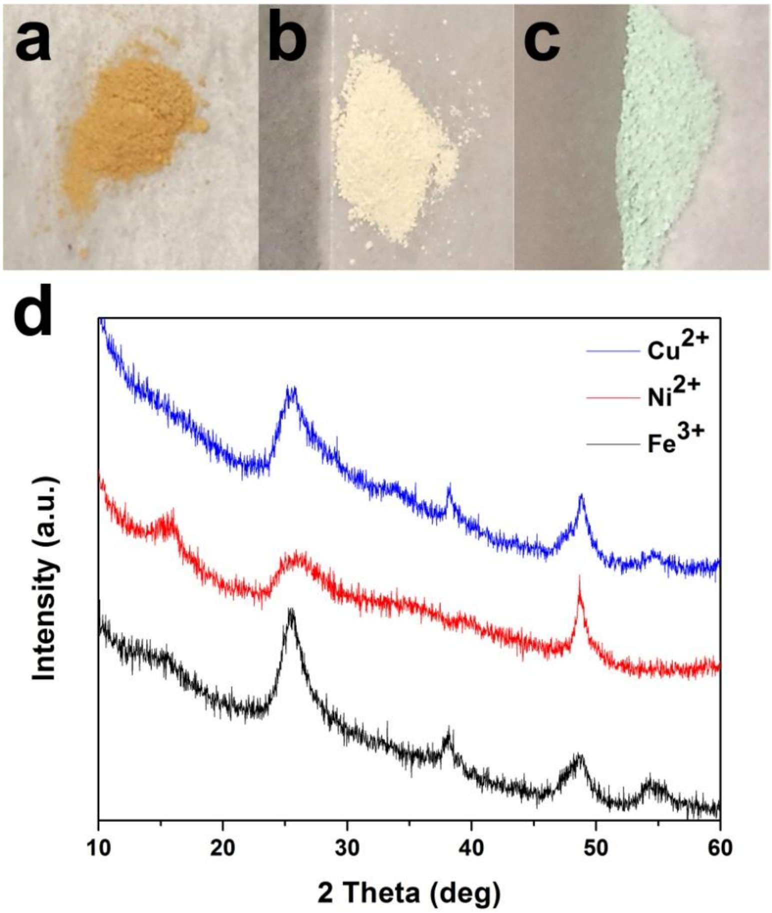

Figure 4.2 (a-c) digital images of metal-TiO_2 powders after cation exchange with hollow sodium titanate. Metals exchanged are (a) Fe^{3+}, (b) Ni^{2+}, and (c) Cu^{2+}. (d) XRD diffractograms of powders after cation exchange for 1 h, indicating primarily anatase crystalline phase.

by the SiO_2. Cation exchange into the sodium titanate structure produces hollow crystalline metal incorporated-TiO_2 structures, as shown in the TEM images in Figure 4.1e-f. The hollow shells consist of many small crystalline domains, consistent with reported results of ageing amorphous TiO_2.[18] Also of note here is how the entirety of the structure is comprised of these small TiO_2 grains, which indicates that the portion of the shell which had expanded into the cavity still consists of TiO_2.

The incorporation of metal ions into the hollow sodium titanate structure can be easily evidenced by the digital images in Figure 4.2 where powders obtained after incorporation of Fe^{3+}, Ni^{2+}, and Cu^{2+} are shown in a, b, and c, respectively. Incorporation of the metal happens concurrently with the transition of the sodium titanate to crystalline TiO_2. Figure 4.2d shows XRD diffractograms of sodium titanate samples after refluxing in solutions containing Fe^{3+}, Ni^{2+}, and Cu^{2+}. It is evident that the samples have been converted to anatase TiO_2 through the appearance of peaks at $2\theta \approx 25.3$, 37.8, 48.0, a broad peak combining typical peaks at 53.8 and 54.9° which are attributed to the (101), (004), (200), (105) and (211) planes of the anatase TiO_2 crystal lattice. The sample refluxed with Ni^{2+} does indicate some remaining sodium titanate with a peak in the diffractogram at $2\theta \approx 15°$, typical of $Na_2Ti_6O_{13}$,[19] which is likely due to it being the weakest acid of the three metals tested.

Figure 4.3a shows the XRD diffractograms of hollow sodium titanate after refluxing in a Cu^{2+} solution for different periods of time, from 1 hour to 24 hours. The XRD diffractograms show that by refluxing for longer periods of time, the sodium titanate conversion to anatase TiO_2 becomes more complete and a higher degree of

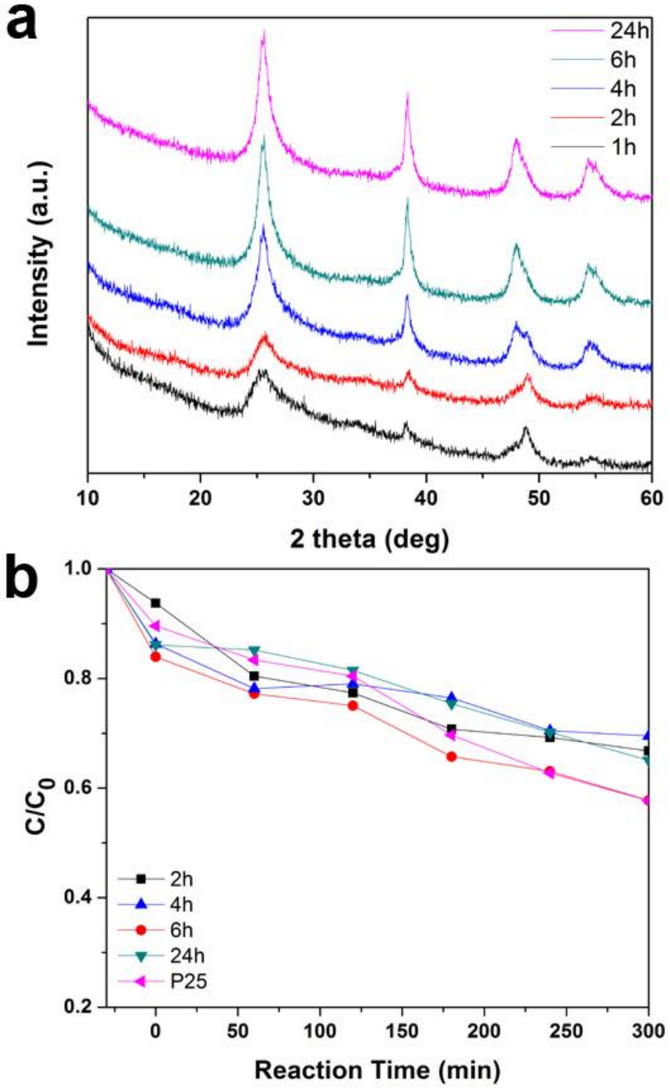

Figure 4.3 (a) XRD diffractograms of powders after cation exchange with Cu^{2+} for different periods of time. Crystalline phase remains anatase with an increase in peak sharpness, indicating a higher degree of crystallinity. (b) Visible light degradation of Rhodamine B dye utilizing Cu^{2+} exchanged titanate after refluxing for different periods of time.

crystallinity is obtained. These Cu^{2+} doped samples were then utilized for the visible light photocatalytic degradation of Rhodamine B dye. Figure 4.3b shows the degradation of the dye on the Cu^{2+} doped catalysts. Interestingly, the sample refluxed after 6 hour shows the best photocatalytic activity by degrading, comparable to that of P25 TiO_2. The samples prepared by refluxing for 2, 4, and 24 hours were approximately equal in activity. The sample refluxed for 24 hours shows no significant difference in crystallinity from the sample refluxed after 6 hours so the decrease in activity is noticeable. It is presumed that some of the Cu^{2+} may have reacted elsewhere over the course of 24 hours and, as such, is not present at the same dopant concentration as in the sample refluxed for 6 hours.

To better utilize the sodium titanate hollow samples, Fe^{3+} exchange was investigated in order to later reduce it to form a magnetic TiO_2 composite. This magnetic composite could then be utilized as an easily isolatable material for phosphoprotein purifications. One necessary component to this is a high surface area. Figure 4.4 shows the N_2 physisorption isotherms of sodium titanate samples after cation exchange with Fe^{3+} for 1 hour, 24 hours, and after reduction of both samples at 400 °C for 2 h. Each of the samples shows a type IV isotherm, consistent with a mesoporous structure. The multi point BET method was used in the relative pressure range of 0.05-0.3 to calculate the surface area of the samples. The surface area was the highest for the sample refluxed after only 1 hour, at 358 m^2 / g. By refluxing for 24 h, the surface area decreases to 195 m^2 / g, which corresponds to an increase in both crystallinity and pore size. Upon reduction under H_2, which further increases the degree of crystallinity the surface areas decrease to

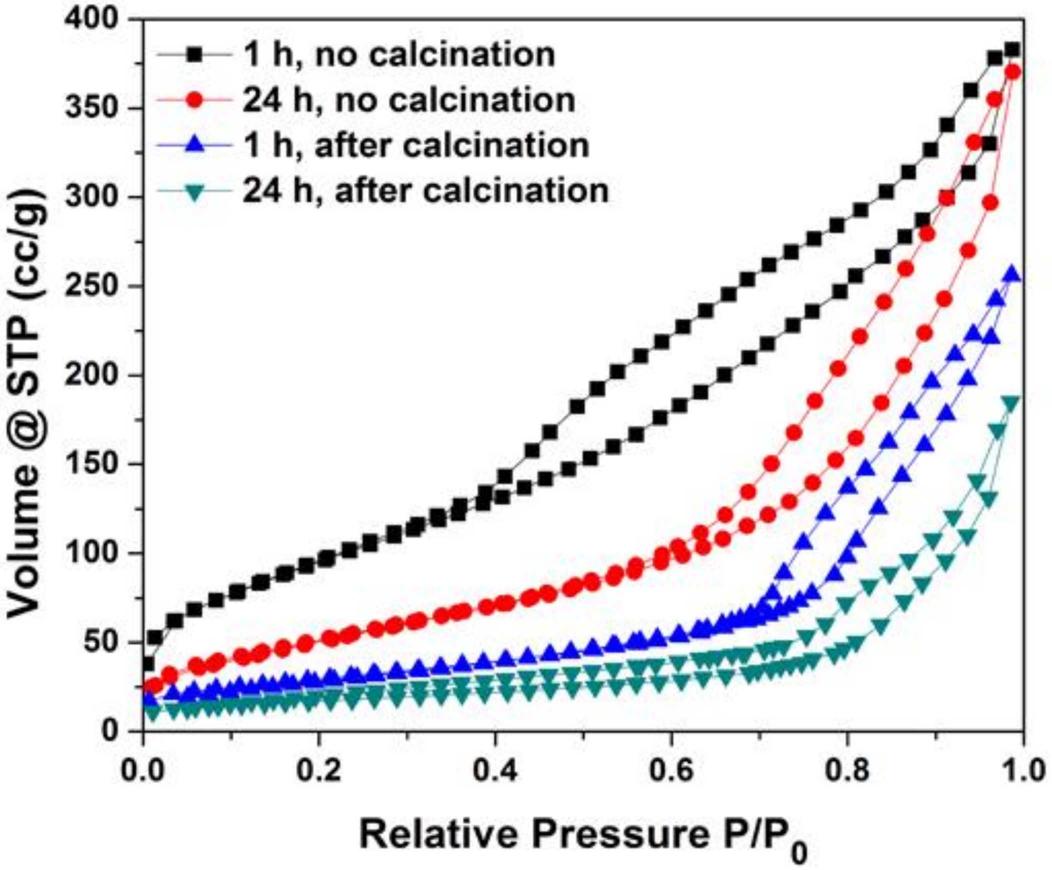

Figure 4.4 N_2 physisorption isotherms for Fe^{3+} exchanged sodium titanate after refluxing for 1 h and 24 h and the same samples after calcination at 400 °C for 2 h under an H_2 atmosphere. The surface areas calculated by the multi point BET method are 358, 195, 106 and 61 m^2 / g, respectively.

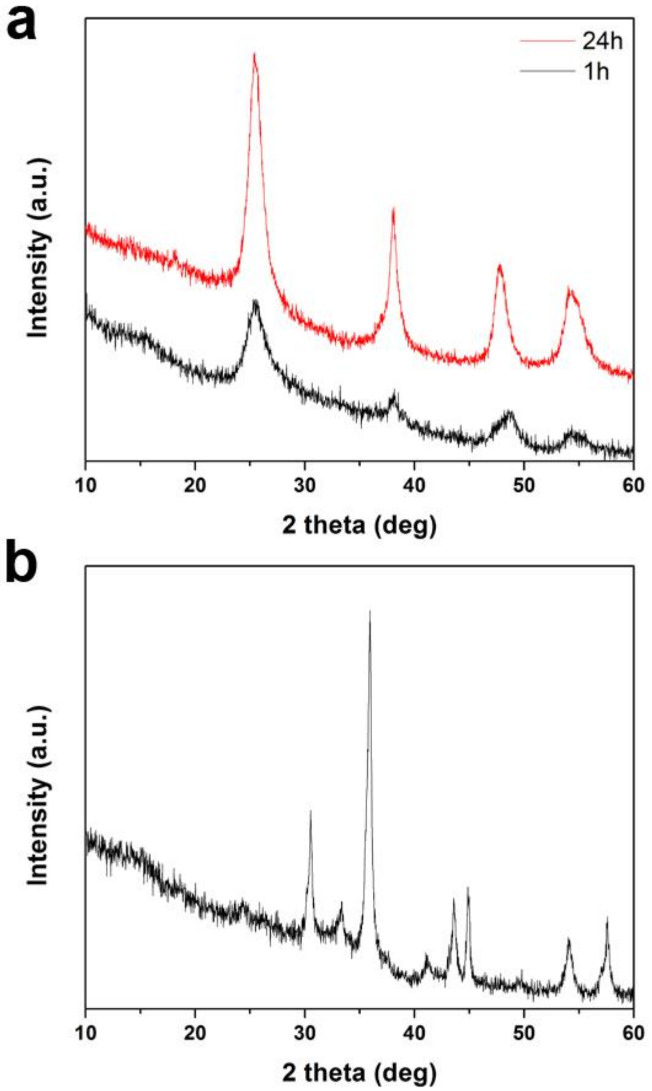

Figure 4.5 (a) XRD diffractograms of powders after cation exchange with Fe^{3+} for 1 hour (black line) and 24 h (red line). Crystalline phase remains anatase with an increase in peak sharpness, indicating a higher degree of crystallinity. (b) XRD diffractogram of Fe^{3+} exchanged TiO_2 after reduction under H2 at 400 °C for 2 h. Sample consists of a mixture of Fe_3O_4 and Fe_2TiO_5 with no indication of TiO_2 present.

106 and 61 m^2 / g, respectively. The XRD diffractograms of these samples are shown in Figure 4.5. The noticeable increase in crystallinity with refluxing time is apparent in Figure 4.5a where the peaks become much sharper as the refluxing time is increased from 1 h to 24 h. Figure 4.5b shows the XRD diffractogram of the sample refluxed for 1 h after reduction under H_2 at 400 °C for 2h. There is no longer any indication of TiO_2 however there is formation of Fe_2TiO_5. Additionally, magnetite iron oxide, Fe_3O_4, peaks become apparent as well. The resulting iron oxide-iron titanate sample is both magnetic and porous with a surface area noted earlier of 106 m^2 / g.

The formation of a magnetic TiO_2 derived material can find a significant use for the separation of phosphorylated proteins from non-phosphorylated proteins. The study of protein phosphorylation has seen considerable research over the past few decades, however research has been limited to a small number of proteins and identification methods. In order to increase the concentration of phosphorylated proteins and thus the signal to noise, methods of separating these proteins from non-phosphorylated proteins have been of considerable interest. The utilization of metal oxide affinity chromatography, MOAC, has been one such area of recent interest.[20] The selective binding of the phosphate group to metal oxide surfaces, especially TiO_2, allows for this technique to be advantageous.[13,14,21] Further, incorporation of a magnetic component simplifies the separation procedures and hastens the process.[22,23] Figure 4.6 shows a schematic illustration of the procedure of separating phosphorylated proteins from non-phosphorylated ones. A mixture of a phosphorylated protein, β-casein, and two non-phosphorylated proteins, β-lactoglobulin and horseradish peroxidase, is dissolved in 50%

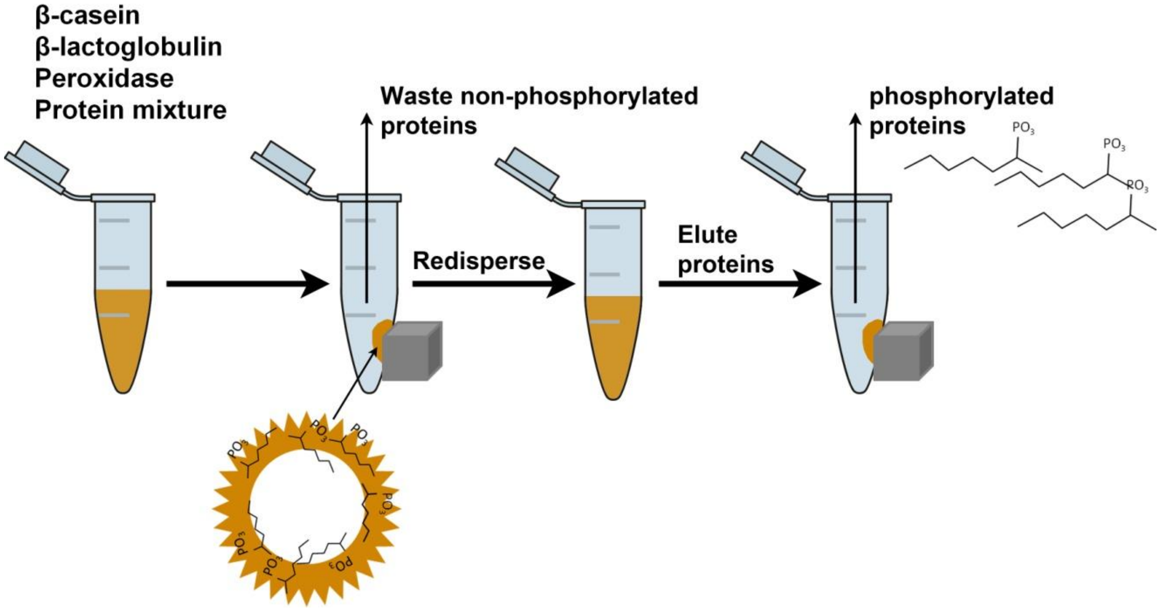

Figure 4.6 Schematic illustration of the process of selective enrichment of phosphorylated proteins by using the Fe-TiO_2 composite to both adsorb the proteins and collect the particles by magnetic separation.

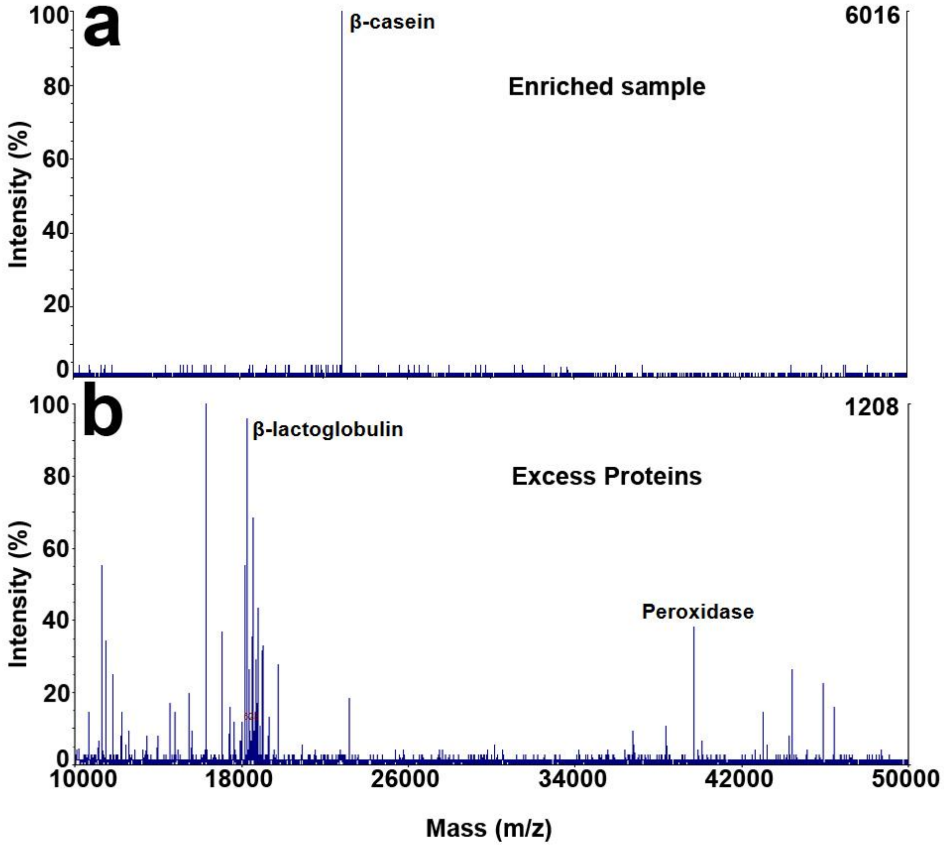

Figure 4.7 MALDI-TOF MS spectra of β-casein, β-lactoglobulin, and horseradish peroxidase protein mixture after enrichment. (a) The enriched beta casein which had adsorbed to the Fe-TiO_2 composite shows no excess proteins whereas (b) shows proteins which were not adsorbed to the composite because of a lack of phosphorylated sites.

acetonitrile 0.1% trifluoroacetic acid water buffer solution to a total protein concentration of 0.75 mg/mL. An aliquot of this sample was removed and to it was added the TiO_2 composite material. This sample was mixed then the composite was magnetically separated and fresh buffer solution was added. The waste non-phosphorylated proteins could be removed from the supernatant while the phosphorylated proteins were adsorbed to the TiO_2 composite. The proteins could then be eluted from the TiO_2 composite and analyzed by MALDI-TOF mass spectra. Figure 4.7a shows the mass spectra of the separated phosphorylated protein, β-casein with its primary peak at $m/z \approx 24000$. The mass spectrum shows no indication of either of the non-phosphorylated proteins, indicating good selectivity for the target β-casein. Figure 4.7b shows the mass spectra of the supernatant from the initial wash which clearly shows the presence of the non-phosphorylated proteins, β-lactoglobulin and horseradish peroxidase. It must be noted that there appears to be a percentage of excess β-casein remaining in the excess protein mass spectrum, indicating that the TiO_2 composite was saturated at the concentrations used.

4.4 Conclusion

Here we have developed a scalable system to synthesize hollow, metal doped TiO_2 colloidal materials which can be easily doped with various different metals. The procedure utilizes hollow sodium titanate shells which were synthesized through high temperature etching of $SiO_2@TiO_2$ core@shell composites. The hollow sodium titanate could then be cation exchanged with the target metal in order to get the final metal incorporated product. Additionally, since the metal ion exchange was done at elevated temperatures in an aqueous solution, the resulting TiO_2 is transformed from amorphous to crystalline anatase. One metal ion exchange tested was Cu^{2+} which yielded a metal doped TiO_2 composite which was readily dispersed in water and could be utilized for the photocatalytic degradation of Rhodamine B under visible light irradiation. A more substantial product was obtained when exchanging the sodium ions for Fe^{3+} which, after reduction by calcination under a H_2 environment, provided a porous, magnetic iron oxide-TiO_2 composite. The benefits of such a composite were demonstrated when utilized for the selective enrichment of phosphorylated proteins. The porosity allowed for a significant adsorption of the phosphoproteins to the composite which the magnetic recoverability allowed for quicker processing compared to separation by centrifugation. Further utilization of this method can yield metal incorporated TiO_2 products with a wide range of possible metals for a number of applications such as in sensors, energy storage, and catalysis.

4.5 References

(1) Chen, D.; Caruso, R. A. *Adv. Funct. Mater.* **2013**, *23*, 1356.

(2) Petkovich, N. D.; Stein, A. *Chem. Soc. Rev.* **2013**, *42*, 3721.

(3) Joo, J. B.; Zhang, Q.; Dahl, M.; Zaera, F.; Yin, Y. *J. Mater. Res.* **2013**, *28*, 362.

(4) Joo, J. B.; Zhang, Q.; Lee, I.; Dahl, M.; Zaera, F.; Yin, Y. *Adv. Funct. Mater.* **2012**, *22*, 166.

(5) Zhu; Gao; Lan, Y.; Song; Xi; Zhao *J. Am. Chem. Soc.* **2004**, *126*, 8380.

(6) Zhu, H. Y.; Lan, Y.; Gao, X. P.; Ringer, S. P.; Zheng, Z. F.; Song, D. Y.; Zhao, J. C. *J. Am. Chem. Soc.* **2005**, *127*, 6730.

(7) Mao, Y.; Kanungo, M.; Hemraj-Benny, T.; Wong, S. S. *J. Phys. Chem. B* **2006**, *110*, 702.

(8) Joo, J. B.; Lee, I.; Dahl, M.; Moon, G. D.; Zaera, F.; Yin, Y. *Adv. Funct. Mater.* **2013**, *23*, 4246.

(9) Ye, M.; Lu, Z.; Hu, Y.; Zhang, Q.; Yin, Y. *J. Mater. Chem. A* **2013**, *1*, 5097.

(10) Yang, D.; Zheng, Z.; Yuan, Y.; Liu, H.; Waclawik, E. R.; Ke, X.; Xie, M.; Zhu, H. *Phys. Chem. Chem. Phys.* **2010**, *12*, 1271.

(11) Zhang, Y.; Tang, Y.; Liu, X.; Dong, Z.; Hng, H. H.; Chen, Z.; Sum, T. C.; Chen, X. *Small* **2013**, *9*, 996.

(12) Lu, Z.; Duan, J.; He, L.; Hu, Y.; Yin, Y. *Anal. Chem.* **2010**, *82*, 7249.

(13) Lu, Z.; Ye, M.; Li, N.; Zhong, W.; Yin, Y. *Angew. Chem.* **2010**, *122*, 1906.

(14) Li, H.; Shi, X.; Qiao, L.; Lu, X.; Xu, G. *J. Chromatogr. A* **2013**, *1275*, 9.

(15) Kojima, T.; Sugimoto, T. *J. Phys. Chem. C* **2008**, *112*, 18445.

(16) Sugimoto, T.; Kojima, T. *J. Phys. Chem. C* **2008**, *112*, 18760.

(17) Li, W.; Deng, Y.; Wu, Z.; Qian, X.; Yang, J.; Wang, Y.; Gu, D.; Zhang, F.; Tu, B.; Zhao, D. *J. Am. Chem. Soc.* **2011**, *133*, 15830.

(18) Wang, D.; Liu, L.; Zhang, F.; Tao, K.; Pippel, E.; Domen, K. *Nano Lett.* **2011**, *11*, 3649.

(19) Štengl, V.; Bakardjieva, S.; Šubrt, J.; Večerníková, E.; Szatmary, L.; Klementová, M.; Balek, V. *Appl. Catal., B* **2006**, *63*, 20.

(20) Leitner, A. *TrAC, Trends Anal. Chem.* **2010**, *29*, 177.

(21) Ma, W.-F.; Zhang, Y.; Li, L.-L.; You, L.-J.; Zhang, P.; Zhang, Y.-T.; Li, J.-M.; Yu, M.; Guo, J.; Lu, H.-J.; Wang, C.-C. *ACS Nano* **2012**, *6*, 3179.

(22) Chen, C.-T.; Chen, Y.-C. *Anal. Chem.* **2005**, *77*, 5912.

(23) Lu, J.; Wang, M.; Deng, C.; Zhang, X. *Talanta* **2013**, *105*, 20.